Sede Amministrativa: Università degli Studi di Bologna
Dipartimento di Fisica "Augusto Righi"

Dottorato di Ricerca in Fisica

Ciclo XV

$t\bar{t}$ Production in Multijet Events at CDF (RunII)

Coordinatore: Ch.mo Prof. Giovanni Venturi

Supervisore: Ch.mo Prof. Andrea Castro

Dottorando: Dott. Ambra Alessia Gresele

14 Marzo 2003

Contents

Introduction

This thesis decribes the **all hadronic $t\bar{t}$ analysis** on the $\sim 100\ pb^{-1}$ of data collected so far by the CDF experiment (**Chapter 2** and **Chapter 3**) in the $p\bar{p}$ collisions at $\sqrt{s} = 2$ TeV of Tevatron (Fermilab).
At the Tevatron energy the production $q\bar{q} \rightarrow t\bar{t}$ is dominant. In the Standard Model the t-quark decays very often in a W boson and in a b-quark (**Chapter 1**). Because the *top* mass is greater than the sum m(W) + m(b), the W boson is not virtual and the possible final states for the $t\bar{t}$ events depend on the W decay. The best channel for the top discovery is when one or both W bosons decay leptonically (*single lepton + jet channel* or *di-leptonic channel*). In these cases we have very small background contaminations which can be eliminated with kinematical requests or requiring the presence of a b-jet. Instead, the largest branching ratio (44%) is when both W's decay in $q\bar{q}'$:

$$t\bar{t} \rightarrow W^+bW^-\bar{b} \rightarrow (q\bar{q}')b(q\bar{q}')\bar{b} \tag{1}$$

giving a final state with 6 jets. Unfortunately this channel is affected by a very large QCD background which makes very difficult the isolation of the signal.
Starting with a signal/background ratio of about 10^{-3} it is necessary to study a selection able to reduce the background events but keeping a good signal efficiency.
Chapter 4 is dedicated to the description of the algorithms which recontruct the tracks and the jets at CDF.
In our analysis the signal events are characterized by the presence of 6 quarks in the final state which can make 6 jets identified in the calorimeter. Because the jets can be merged, lost along the beam or fail the threshold in energy, the minimal jet multeplicity required is 5. After that we make a very tight selection based on the kinematical characteristics of the events (**Chapter 5**).
In this way we can increase the signal/background ratio to about 1/15 which is a good improvement but is not enough. Because the $t\bar{t}$ events have always two b-quarks in the final state, we can also require at least one b-jet (**Chapter 6**) requiring a secondary vertex coming from a b quark decay.
Putting together the optimized kinematicals selection and b-tagging we are able to evidentiate a small $t\bar{t}$ signal from which we derive a measurement of the $t\bar{t}$ production cross section (**Chapter 7**).

Chapter 1

Theory and phenomenology of the Standard Model

The top quark mass is a fundamental parameter of the Standard Model (SM) and is needed for extracting other parameters from precision electroweak measuments. In this chapter a brief review of the Standard Model, focused on the problem of introducing masses for both vector bosons and fermions, will be presented. This will introduce the issue of Higgs Physics. The evaluation of the range for the Higgs boson mass depends strongly by the experimental value of the top mass. The top quark and its existence, established by direct experimental observation at the Fermilab Tevatron by the CDF and D0 Collaborations, will be dealt with in this chapter.

1.1 Introduction to the Standard Model

1.1.1 Towards a unified electroweak theory

The first approach to weak interactions finds its origins in 1934, when Fermi [1] proposed a theory able to account for the nuclear β-decay process (see fig. 1.1), which can be expressed as:

$$\mathrm{n} \longrightarrow \mathrm{p} + \mathrm{e}^- + \overline{\nu}_\mathrm{e} \ .$$

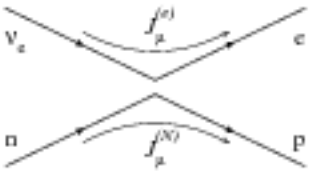

Figure 1.1: $\mathrm{n} \to \mathrm{p e}^- \overline{\nu}_\mathrm{e}$

Driven from experimental observations, suggesting for weak decays longer lifetimes than in electromagnetic processes, Fermi's idea consisted of treating weak interactions as 'point-like' electromagnetic interactions. In order to make such an analogy clear, the electromagnetic scattering of an electron off a proton (see fig. 1.2) can be considered:

$$\mathrm{e} + \mathrm{p} \longrightarrow \mathrm{e} + \mathrm{p} \ .$$

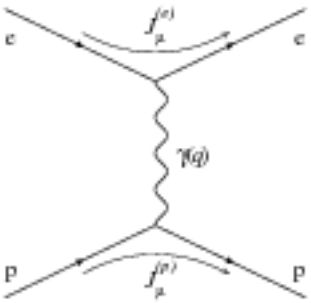

Figure 1.2: $\mathrm{ep} \to \mathrm{ep}$

Due to the fact that lepton and baryon numbers are conserved, this process can be thought as the interaction of two currents (indicated in figure 1.2 as J_μ) via a single (virtual) photon exchange, which leads to the scattering amplitude

$$\mathcal{M} \propto \overline{\mathrm{p}}\, \gamma^\mu\, \mathrm{p}\, \frac{e^2}{q^2}\, \overline{\mathrm{e}}\, \gamma_\mu\, \mathrm{e} \ ,$$

where q is the momentum transfer, γ_μ the Dirac matrix and p (e) the fermion spinor. For the cross section, QED predicts

$$\sigma \sim |\mathcal{M}|^2 \sim \frac{e^4}{s} \ , \tag{1.1}$$

where s is the square of the center of mass energy of the e−p system and e is the electron charge.

By analogy, Fermi supposed that weak processes, such as the β-decay, could be described in a similar way. Using the partons inside nucleons, the requirement of 'contact' interaction leads to the amplitude

$$\mathcal{M} \propto G_F \, (\bar{\mathrm{e}} \, \Gamma^\mu \, \nu_\mathrm{e})(\bar{\mathrm{u}} \, \Gamma_\mu \, \mathrm{d}) \ ,$$

where the form of Γ^μ has been determined to be $\gamma^\mu(1-\gamma_5)/2$, in order to account for parity and charge conjugation violations which characterize weak interactions[1] The numerical value of the Fermi's constant, G_F, has been estimated by comparison of the theoretical prediction for the β-decay rate with the empirical measurement to be $1.16639(1) \times 10^{-5} GeV^{-2}$. Now, if the weak process

$$\nu_\mathrm{e} + \mathrm{d} \longrightarrow \mathrm{e} + \mathrm{u},$$

which is described by a diagram similar to the one in fig. 1.1, or any other weak scattering process, is considered, the Fermi theory predicts a cross section:

$$\sigma \sim G_F^2 s \ . \tag{1.2}$$

For weak processes at high energies, this relation states that the cross section is divergent with s. This goes against the S-matrix unitarity. In other words, the expression (1.2) is a symptom of the sickness affecting the Fermi theory: non-renormalizability.

A possible solution to this problem consists in forcing the analogy between weak and electromagnetic processes by removing Fermi's assumption of 'contact' interaction in favour of a vector boson mediated weak interaction[2] (see fig. 1.3).

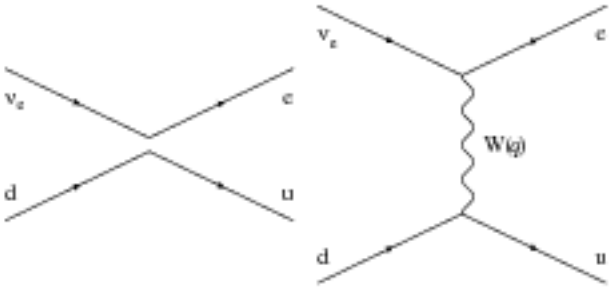

Figure 1.3: e−d *elastic scattering as seen by Fermi and* IVB *theories.*

[1] For a definition of the Dirac matrices γ^μ, γ_5, see for example [2].

[2] This approach is known as IVB (Intermediate Vector Boson) theory.

In order to preserve the short-range characteristic of the weak interactions, the intermediate boson (the so called $W^{\pm}$ particle) has to be massive. This has the immediate consequence of introducing a massive vector boson propagator

$$\frac{g^{\mu\nu} - \frac{q^{\mu}q^{\nu}}{M_W^2}}{q^2 - M_W^2} \tag{1.3}$$

into the amplitude of the considered process.

Although the IVB theory reproduces Fermi's results in the low energy limit, removing at the same time the unitarity violations that appear at tree-level, it presents some difficulties that affect heavily its predictability:

- the IVB theory cannot describe some processes at tree-level. This is the case, for instance, of $e + \nu_\mu \rightarrow e + \nu_\mu$;
- unitarity violations still emerge at tree-level in processes like $e^+e^- \rightarrow W^+W^-$, where the total amplitude is the result of the interference of a weak and an electromagnetic contribution (see fig. 1.4).

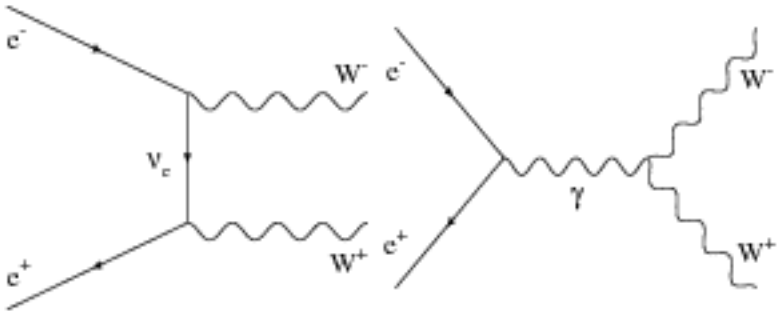

Figure 1.4: IVB *theory contributions to* $e^+e^- \rightarrow W^+W^-$

These signals seem to suggest that the IVB theory is not complete. The simplest and most logical way of addressing the problem consists in the introduction of an additional vector boson (Z^0) with the following properties:

- it must be neutral, in order to enable neutral currents[3] at tree-level (see fig. 1.5);
- as the $W^{\pm}$, it must interact 'electroweakly' in order to be able to interfere destructively both with the weak and the electromagnetic diagrams which concur to a given process when these are simultaneously divergent. In the case of the process $e^+e^- \rightarrow W^+W^-$, the additional contribution is shown in fig. 1.6.

[3] As opposed to the currents involving the emission or absorption of a charged vector boson, which are indicated as 'charged currents'. In agreement with observations, neutral currents do not change the fermion flavour.

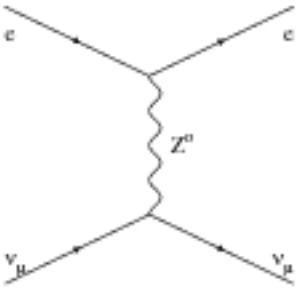

Figure 1.5: $e\nu_\mu \to e\nu_\mu$

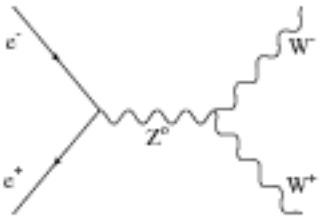

Figure 1.6: Z^0 *contribution to* $e^+e^- \to W^+W^-$ *(see fig. 1.4)*

This solution solves all the model diseases mentioned above[4], but the cure works at tree-level only: higher-order calculations are still not possible. The reason this happens can be studied by considering the cross section of the simple box diagram shown in fig. 1.7, where the (divergent) contribution of the loop integral is put in evidence (the divergence arises when the limit Λ(cutoff value)$\to\infty$ is taken).

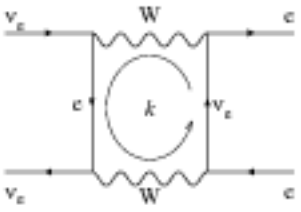

$$\Longrightarrow \qquad \sigma \sim \int^{\Lambda} \mathrm{d}^4 k \frac{1}{k}\frac{1}{k} \sim \Lambda^2$$

Figure 1.7: *Box diagram for the electroweak theory.*

Since the effect evidenced in fig. 1.7 becomes progressively more severe as the perturbative order increases, it is clear that predictions beyond the tree level are not possible.
It is then clear that all problems are originated by the behaviour of the vector boson propagator in case of massive bosons V – see expression (1.3): in this case, the term $q^\mu q^\nu / M_V^2$ at high energies causes the suppression of the $1/q^2$ factor from the denominator, and, consequently, of the two $1/k^2$ factors which enable converging results in the cross section of QED processes (where $M_\gamma = 0$).

1.1.2 The Standard Model of electroweak interactions

The previous paragraph has put in evidence the difficulty of formulating a renormalizable theory capable of describing the reality of electroweak interactions in terms of processes characterized by massive bosons exchanges.

At the same time, the origin of QED renormalizability comes from its intermediate boson being massless. This can be understood in terms of an underlying local symmetry

[4] At least in the limit of massless fermions. See for example [3], § 21.2.

obeyed by the theory: the Lagrangian density $\mathcal{L}$ of a system interacting electromagnetically has to be invariant under the field transformation

$$\psi(x) \longrightarrow e^{iQ\theta(x)}\psi(x) \ ,$$

where Q – the generator of the transformation – is the electric charge operator. The symmetry group which describes such a transformation is an U(1) group, which is indicated as $\mathrm{U}(1)_{em}$ in order to remind the electromagnetic nature of the generator. The locality of the transformation is ensured by the space-time dependence of the transformation parameter θ.
On one hand the invariance under $\mathrm{U}(1)_{em}$ guarantees that electric charge conservation holds, while, on the other, a new vector field A^μ – which can be associated to the γ intermediate boson – has to be introduced in $\mathcal{L}$ through an interaction term with fermion fields. Although a kinetic term for A^μ is allowed by the overall symmetry, this does not hold true for a mass term, which imply necessarily that $M_\gamma = 0$. In other words, $M_\gamma = 0$ is a signal that the $\mathrm{U}(1)_{em}$ symmetry is not violated, which in turn implies electric charge conservation.

The attempt of obtaining a renormalizable theory of electroweak interactions consists in providing the electroweak theory with a gauge[5] symmetry capable of reproducing the characteristic weak current left-right asymmetry responsible of parity and charge conjugation violations. In order to identify the local group, the weak charged current

$$J^\mu = \overline{\nu}_\ell \frac{1}{2}\gamma^\mu(1-\gamma_5)\ell$$

can be written as

$$J^\mu = \overline{\mathrm{L}}\gamma^\mu\tau^+\mathrm{L} \ , \tag{1.4}$$

with

$$\mathrm{L} = \tfrac{1}{2}(1-\gamma_5)\begin{pmatrix} \nu_\ell \\ \ell \end{pmatrix} \equiv \begin{pmatrix} \nu_\ell \\ \ell \end{pmatrix}_L$$
$$\tau^+ = \tfrac{1}{2}(\tau_1 + i\tau_2) \ ,$$

where τ_a stand for the usual Pauli matrices[6]. Note that writing (1.4) forces the fermion fields $\psi = \ell, \nu_\ell$ to be assigned to some multiplet representation of the underlying (unknown) gauge group, of which τ^+ will be one of the generators. In other words, this procedure is aimed at pointing out an explicit sign of the gauge group by simple phenomenological considerations.
In the same way, the hermitian conjugate current $J^{\mu\dagger}$

$$J^{\mu\dagger} = \overline{\mathrm{L}}\gamma^\mu\tau^-\mathrm{L} \ ,$$

with

$$\tau^- = \frac{1}{2}(\tau_1 - i\tau_2) \ ,$$

[5] *I.e.* local.

[6] Note that the subscript '*L*' to the lepton doublet reminds the action of the operator $(1-\gamma_5)/2$, which selects the left-hand helicity projection of a fermion field.

has to be considered, since it is involved into the interaction as much as J^μ is.
Since gauge bosons and currents are in one-to-one correspondence with the generators of the symmetry group, and since these, in turn, form a closed set with respect to the commutation operation, then the quantity

$$\overline{\mathrm{L}}\gamma^\mu \left[\tau^+, \tau^-\right] \mathrm{L} = \overline{\mathrm{L}}\gamma^\mu \tau_3 \mathrm{L} \equiv J_3^\mu$$

describes an other admissible weak current. In particular, it represents the weak neutral current whose existence has been anticipated on the basis of phenomenological considerations (see pag. 9). No more weak currents – independent from J^μ, $J^{\mu\dagger}$, J_3^μ – can be introduced in this way, since $[\tau_3, \tau^\pm] = 2\tau^\pm$.

Therefore, weak currents have been written in a form that points out a SU(2)-symmetric structure of weak interactions, since SU(2) is the group generated by the Pauli matrices. However, it should be noted that only left-handed fermions have been arranged in this scenario[7]. Since right-handed fermions, such as $\nu_{\ell R}$ and ℓ_R, do not participate in weak processes involving charged currents, one can suppose of arranging them into $\mathrm{SU}(2)_L$ singlets.

As previously mentioned, gauge bosons are in one-to-one correspondence to group generators of local symmetries. Therefore, a vector boson field W_i^μ has to be associated to each of $\mathrm{SU}(2)_L$ generator τ_i. While the structure of the charged currents J^μ, $J^{\mu\dagger}$ suggests that a suitable combination of the W_i^μ fields (precisely $(\mathrm{W}_1^\mu \mp \mathrm{i}\mathrm{W}_2^\mu)/\sqrt{2}$) should be considered for representing the $W^\pm$ bosons, it is immediately clear that the neutral current J_3^μ and, consequently, W_3^μ, cannot be identified with the electromagnetic current and its intermediate boson (γ) respectively. Two reasons support this conclusion: first, electromagnetic currents do not couple electrically neutral objects, such as neutrinos. Secondly, electromagnetic currents do not exhibit parity or charge conjugation violations: in fact, they are characterized by a vector Lorentz bilinear (*i.e.* $\overline{\ell}\gamma^\mu\ell$ – see pag. 7), allowing both left and right-handed fermions to be involved in the electromagnetic interaction.
However, from the comparison between the weak neutral current

$$J_3^\mu = \left(\overline{\nu}_{\ell L}\gamma^\mu \nu_{\ell L} - \overline{\ell}_L \gamma^\mu \ell_L\right) \tag{1.5}$$

and the electromagnetic current

$$J_{em}^\mu = -\left(\overline{\ell}_R \gamma^\mu \ell_R + \overline{\ell}_L \gamma^\mu \ell_L\right) \ , \tag{1.6}$$

it can be noted that the last term in the right-hand side of (1.5) is part of the electromagnetic current (1.6) as well. This suggests that the electromagnetic current can be expressed in terms of the weak neutral current J_3^μ and a new neutral current, indicated as 'weak hypercharge' current J_Y^μ associated to an *ad hoc* neutral generator Y of a gauge U(1) symmetry[8] which corresponds to a neutral gauge boson, B^μ. The simultaneous gauge-invariance under $\mathrm{SU}(2)_L$ and $\mathrm{U}(1)_{em}$ can therefore be expressed in terms of gauge-invariance under the $\mathrm{SU}(2)_L \times \mathrm{U}(1)_Y$ group, where $\mathrm{U}(1)_Y$ is the Abelian group generated by Y.

[7] This is the reason why this symmetry group is usually indicated as $\mathrm{SU}(2)_L$.

[8] By definition, the relation between the neutral generators is

$$Q \equiv I_3 + Y \ , \tag{1.7}$$

where $I_3 = \tau_3/2$ is called 'weak isospin'. The corresponding eigenvalues will be indicated by q, i_3 and y.

In this way, not only has the gauge symmetry group of the electroweak sector of the Standard Model been identified in $\mathrm{SU}(2)_L \times \mathrm{U}(1)_Y$, but also the interactions between gauge bosons and fermions ($gJ^\mu \mathrm{W}^-_\mu$, $gJ^{\mu\dagger}\mathrm{W}^+_\mu$, $gJ^\mu_3 \mathrm{W}_{3\mu}$ and $g'J^\mu_Y \mathrm{B}_\mu$, where g, g' – the so-called 'coupling constants' – describe the strength of the weak and hypercharge current interactions) have been established in a very natural way according to symmetry considerations. As anticipated for leptons, left-handed fermionic fields participating in this picture are arranged into 'weak isospin' doublets

$$\mathrm{L}=\begin{pmatrix} \nu_\ell \\ \ell \end{pmatrix}_L \begin{matrix} \longrightarrow\ q=0 \\ \longrightarrow\ q=-1 \end{matrix} \quad , \ \ell=\mathrm{e},\mu,\tau$$
$$\mathrm{Q}=\begin{pmatrix} u \\ d \end{pmatrix}_L \begin{matrix} \longrightarrow\ q=2/3 \\ \longrightarrow\ q=-1/3 \end{matrix} \quad , \begin{matrix} u=\mathrm{u},\mathrm{c},\mathrm{t} \\ d=\mathrm{d},\mathrm{s},\mathrm{b} \end{matrix} \quad ,$$

where

$$\begin{pmatrix} \cdot \\ \cdot \end{pmatrix}_L \begin{matrix} \longrightarrow\ i_3=1/2 \\ \longrightarrow\ i_3=-1/2 \end{matrix} \quad ,$$

while their right-handed partners are $\mathrm{SU}(2)_L$ singlets (*i.e.* with $i_3=0$)[9]:

$$\begin{matrix} \mathrm{E}=\ell_R, & \ell=\mathrm{e},\mu,\tau \\ \mathrm{U}=u_R, & u=\mathrm{u},\mathrm{c},\mathrm{t} \\ \mathrm{D}=d_R, & d=\mathrm{d},\mathrm{s},\mathrm{b} \end{matrix} \quad .$$

Hence, the model of electroweak interactions has been provided with a non-Abelian gauge invariance. Theories which exhibit this behaviour are known as Yang-Mills (YM) theories [4]. Their peculiarity consists in being renormalizable unless mass terms – which provide an explicit breaking of the gauge symmetry[10] – are introduced. Apparently, no step forward has been made with respect to the extension of the IVB theory. However, the mere essence of YM theories (symmetry), enables to exploit a mechanism that gives mass to both gauge bosons and fermions without an explicit violation of the gauge symmetry [5],[6],[7] nor the renormalizability [8].

1.1.3 The Higgs mechanism

The breaking of a continuous symmetry can be achieved in two ways

explicit: the Lagrangian density $\mathcal{L}$ contains terms which violate the gauge symmetry;

spontaneous: the Lagrangian density $\mathcal{L}$ is invariant under a given symmetry, while the vacuum state (ground state) is not.

As previously mentioned, explicit symmetry breakings lead to non-renormalizable models, in the following we will consider the aspects of spontaneously broken symmetries.

For a spontaneous symmetry breaking (SSB) to happen within the gauge theory of electroweak interactions, a pair of (complex) scalar fields has to be introduced into the

[9] Being $Q(\nu_{\ell R})=0$, $I_3(\nu_{\ell R})=0$ and, consequently, $Y(\nu_{\ell R})=0$, $\nu_{\ell R}$ states do not undergo electroweak interactions and, therefore, do not take part in the electroweak picture.

[10] Exactly as for QED, mass terms for gauge bosons are not allowed by symmetry requirements. The same holds true for fermion masses.

model. In order to be eligible for a SSB mechanism, these fields must exhibit non-trivial transformations properties under the gauge groups they are meant to break. The simplest way of doing this consists in arranging the two scalar fields into a SU(2) doublet:

$$\phi = \begin{pmatrix} \varphi^+ \\ \varphi^0 \end{pmatrix} = \frac{1}{\sqrt{2}} \begin{pmatrix} \varphi_1 + i\varphi_2 \\ \varphi_3 + i\varphi_4 \end{pmatrix} .$$

According to gauge invariance and renormalizability, the most general term of self-interaction for the scalar fields is described by the potential

$$V(\phi) = \mu^2 \phi^\dagger \phi + \lambda (\phi^\dagger \phi)^2 , \tag{1.8}$$

which, for $\lambda \geqslant 0$ and $\mu^2 < 0$ [11], has a minimum for:

$$|\phi|^2 = \frac{1}{2} \left[\varphi_1^2 + \varphi_2^2 + \varphi_3^2 + \varphi_4^2 \right] = -\frac{\mu^2}{2\lambda} \equiv \frac{v^2}{2} . \tag{1.9}$$

The spontaneous breaking of the $SU(2)_L$ symmetry takes place in the act of choosing a particular vacuum state from the multitude defined by (1.9). If the situation where

$$\varphi_1 = \varphi_2 = \varphi_4 = 0 \ , \ \varphi_3 = \sqrt{-\frac{\mu^2}{\lambda}} = v$$

is chosen, the vacuum expectation value (VEV) is

$$\phi_0 = \frac{1}{\sqrt{2}} \begin{pmatrix} 0 \\ v \end{pmatrix} \tag{1.10}$$

and the ϕ field variations around the minimum $\phi_0 = \phi(0)$ can be always written as

$$\phi(x) = \frac{1}{\sqrt{2}} e^{i\epsilon_i(x)\tau_i/v} \begin{pmatrix} 0 \\ v + h(x) \end{pmatrix} \tag{1.11}$$

by adjusting the value of the scalar fields $\epsilon_i(x)$. The number of these fields, which play the same rôle of the Goldstone bosons in the case of spontaneously broken global symmetries, corresponds to the number of broken generators. They are known as '*would-be* Goldstone' bosons since, in virtue of the SU(2)-invariance exhibited by $V(\phi)$, they can be gauged away by the transformation $U(x) = e^{-i\epsilon_i(x)\tau_i/v}$. Therefore[12]:

$$\phi(x) = \frac{1}{\sqrt{2}} \begin{pmatrix} 0 \\ v + h(x) \end{pmatrix} \tag{1.12}$$

This is essentially the core of the Higgs mechanism [9]: of the four degrees of freedom associated to the initial scalar fields φ_i, three are absorbed in the *would-be* Goldstone bosons gauging procedure, to be returned in terms of longitudinal degrees of freedom of three gauge bosons, which in this way acquire a mass. The fourth degree of freedom is associated to $h(x)$ (the Higgs boson H^0) and represents the only physical scalar field of the model. Its mass,

$$M_H = \sqrt{2\lambda v^2} , \tag{1.13}$$

depends on the free parameter λ, and therefore is not predicted by the theory.

[11] The first condition ensures the existence of a lower bound for V, while the second selects a degenerate vacuum.

[12] In the so-called unitary gauge.

However, the renormalizability of the SM enables to set a range of admissible values of M_H. This can be done by solving the system of the one-loop renormalization group equations, which eventually describes the running of the quartic coupling constant λ as a function of μ, the renormalization scale. The behaviour of $\lambda(\mu)$ for different initial conditions $\lambda(M_Z)$ – each related to a given value of M_H by the relation (1.13) – is depicted in fig. 1.8 (where the initial conditions $M_H = 60, 100, 130, 150, 190,\ 210$ GeV/c^2 have been used [10]). Upper and lower bounds can then be set on M_H by requiring that $\lambda \lesssim 1$ (perturbative regime condition) and at the same time $\lambda > 0$ (*triviality* limit) up to a certain scale Λ which will define the upper limit of validity for the Higgs sector of the SM.

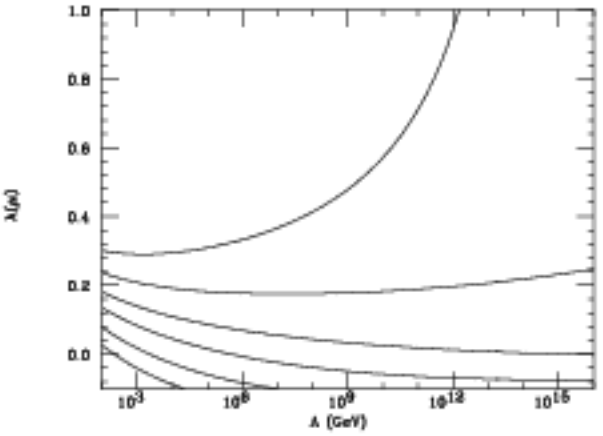

Figure 1.8: *Running of λ in function of energy scale Λ.*

The actual symmetry exhibited by $V(\phi)$ is larger than SU(2). Indeed, $V(\phi)$ is left invariant by the action of the U(1) transformation.
The vacuum state (1.10), violating the residual U(1) symmetry as well, leads to the spontaneous breaking of all four generators of the gauge symmetry. The possibility of giving mass to the photon, arising from the additional *would-be* Goldstone boson implied by the U(1) breaking, is however ruled out since (1.10) preserves $(\tau_3+1)/2$, generator of $\mathrm{U}(1)_{em}$ (see (1.7)). Since this is a combination of broken generators the violated gauge symmetry is partly recovered

$$\mathrm{SU}(2)_L \times \mathrm{U}(1)_Y \longrightarrow \mathrm{U}(1)_{em} \ ,$$

and only three *would-be* Goldstone bosons are allowed.

Once the $\mathrm{SU}(2)_L \times \mathrm{U}(1)_Y$-gauge invariant Lagrangian density for the scalar field ϕ has been obtained

$$\mathcal{L}_S = (D^\mu \phi)^\dagger (D_\mu \phi) - V(\phi) \ ,$$

where

$$D^\mu = \partial^\mu + ig \mathrm{W}_a^\mu(x) \frac{\tau_a}{2} + ig' \mathrm{B}^\mu(x) \frac{1}{2}$$

(with $a = 1, 3$), the mass terms for the gauge bosons can be found by computing the kinetic term of $\mathcal{L}_S$ for $\phi = \phi_0$:

$$\frac{1}{8} v^2 g^2 \left(\mathrm{W}_1^\mu \mathrm{W}_{1\mu} + \mathrm{W}_2^\mu \mathrm{W}_{2\mu}\right) = \frac{1}{4} v^2 g^2 \mathrm{W}^{+\mu} \mathrm{W}_\mu^- \tag{1.14}$$

$$\begin{aligned} &\frac{1}{8} v^2 \left(g' \mathrm{B}^\mu - g \mathrm{W}_3^\mu\right)\left(g' \mathrm{B}_\mu - g \mathrm{W}_{3\mu}\right) = \\ &\quad = \frac{1}{8} v^2 \begin{pmatrix} \mathrm{W}_3^\mu & \mathrm{B}^\mu \end{pmatrix} \begin{pmatrix} g^2 & -gg' \\ -gg' & g'^2 \end{pmatrix} \begin{pmatrix} \mathrm{W}_{3\mu} \\ \mathrm{B}_\mu \end{pmatrix} . \end{aligned} \tag{1.15}$$

While (1.14) states that the combinations $\mathrm{W}^{\pm\mu}=(\mathrm{W}_1^\mu \mp \mathrm{W}_2^\mu)/2$, which can be interpreted in terms of $W^\pm$ bosons, acquire a mass of

$$M_\mathrm{W}=\frac{1}{2}vg \ ,$$

expression (1.15) predicts the mass eigenvalues $M_{1,2}=(v/2)\sqrt{g^2+g'^2}$, 0 for the neutral bosons mass eigenstates

$$\begin{pmatrix} \mathrm{Z}^\mu \\ \mathrm{A}^\mu \end{pmatrix} = \begin{pmatrix} \cos\theta_W & -\sin\theta_W \\ \sin\theta_W & \cos\theta_W \end{pmatrix} \begin{pmatrix} \mathrm{W}_3^\mu \\ \mathrm{B}^\mu \end{pmatrix} \ ,$$

where θ_W (Weinberg angle) is defined by the diagonalization condition $\tan\theta_W=g'/g$ for the mass matrix contained in (1.15). Once A^μ, the massless eigenstate associated to the unbroken generator Q, is identified with the photon field γ, the remaining field Z^μ will represent the neutral boson Z^0. In this way, Z^0 will be given the mass:

$$M_\mathrm{Z}=\frac{1}{2}\frac{vg}{\cos\theta_W} \ .$$

The rotation in the space of neutral boson fields modifies the couplings of the neutral currents to the corresponding gauge bosons

$$\begin{array}{rcl} \mathrm{Z}^0\mathrm{f}\bar{\mathrm{f}} & \sim & \left(I_3-\sin^2\theta_W Q\right) g/\cos\theta_W \\ \gamma\mathrm{f}\bar{\mathrm{f}} & \sim & g\sin\theta_W Q \end{array} \ ,$$

expressions that establish a formal relationship between weak and electromagnetic interactions. In particular, the latter suggests that

$$e=g\sin\theta_W \ ,$$

which in turn – together with the diagonalization requirement ($\tan\theta_W=g'/g$) – implies:

$$e=g'\cos\theta_W \ .$$

The interaction of H^0 with the gauge bosons can be found by following a similar procedure: the kinetic term of $\mathcal{L}_S$ this time has to be expanded in terms of (1.12). Neglecting the kinetic term for h, one obtains

$$(D^\mu\phi)^\dagger(D_\mu\phi)\supset\left(M_\mathrm{W}^2\mathrm{W}^{+\mu}\mathrm{W}_\mu^- + \frac{1}{2}M_\mathrm{Z}^2\mathrm{Z}^\mu\mathrm{Z}_\mu\right)\left(1+\frac{h}{v}\right)^2 \ ,$$

expression which describes, besides the gauge bosons mass terms, the interaction vertices:

$$\begin{array}{rcl} h\mathrm{Z}_\mu^0\mathrm{Z}_\nu^0 & \sim & M_\mathrm{Z}^2 g_{\mu\nu}/v \\ h\mathrm{W}_\mu^+\mathrm{W}_\nu^- & \sim & M_\mathrm{W}^2 g_{\mu\nu}/v \\ hh\mathrm{Z}_\mu^0\mathrm{Z}_\nu^0 & \sim & M_\mathrm{Z}^2 g_{\mu\nu}/(2v^2) \\ hh\mathrm{W}_\mu^+\mathrm{W}_\nu^- & \sim & M_\mathrm{W}^2 g_{\mu\nu}/(2v^2) \end{array} \ . \tag{1.16}$$

As previously mentioned, explicit fermion mass terms are forbidden by the electroweak gauge symmetry. However, fermion masses can be generated by the Higgs boson VEV if

the Lagrangian density of the model includes a $SU(2)_L \times U(1)_Y$-symmetric term which describes the interactions between fermions and H^0 in terms of Yukawa couplings

$$\mathcal{L}_{Yuk} = -(\overline{L}\phi h_E E) - (\overline{Q}\phi h_D D + \overline{Q}\tilde{\phi} h_U U) + h.c. \ , \tag{1.17}$$

where $\tilde{\phi}$ is defined as the charge conjugate of ϕ [13]

$$\tilde{\phi} \equiv i\tau_2 \phi^* = \begin{pmatrix} \varphi^{0*} \\ -\varphi^- \end{pmatrix}$$

and h_E, h_D and h_U are generic $n \times n$ matrices in the generation space[14], since $SU(2)_L$ singlets and doublets carry the same quantum numbers across fermion generations.

Fermion masses and couplings with H^0 emerge explicitly when expression (1.17) is evaluated in the unitary gauge (*i.e.* in terms of (1.12) and (1.18)):

$$\mathcal{L}_{Yuk} = -\frac{1}{\sqrt{2}}(v+h)\left[(\bar{\ell}_L h_E \ell_R) + (\bar{d}_L h_D d_R + \bar{u}_L h_U u_R)\right] + h.c. \ . \tag{1.19}$$

If quarks are considered, the determination of u and d-type quark masses corresponds to diagonalizing the matrices h_D and h_U. This can be done introducing the mass eigenstates u^0, d^0 connected to the interaction eigenstates u, d by two biunitary transformations

$$\begin{array}{ll} u_L = U_L u_L^0 \ , & u_R = U_R u_R^0 \\ d_L = V_L d_L^0 \ , & d_R = V_R d_R^0 \end{array} \ , \tag{1.20}$$

where the hermitian U_L, U_R, V_L, V_R matrices are chosen so that

$$\begin{aligned} U_L^\dagger h_U U_R &= diag(h_U^1, h_U^2, \dots, h_U^n) \\ V_L^\dagger h_D V_R &= diag(h_D^1, h_D^2, \dots, h_D^n) \end{aligned}$$

with $h_{U,D}^f$ real and non-negative. In this way, the hadronic sector of (1.19) can be written in the form

$$\mathcal{L}_{Yuk}^{had} = -\frac{1}{\sqrt{2}}(v+h)\sum_{f=1}^{n}\left(\bar{d}_{fL}^0 h_D^f d_{fR}^0 + \bar{u}_{fL}^0 h_U^f u_{fR}^0\right) + h.c. \ ,$$

which puts in evidence both quark masses

$$m_U^f = \frac{h_U^f v}{\sqrt{2}} \ , \ m_D^f = \frac{h_D^f v}{\sqrt{2}}$$

and quark couplings to H^0:

$$H^0 q\overline{q} \sim \frac{m_q}{v} \ . \tag{1.21}$$

[13] $\tilde{\phi}$ has the same transformation properties of ϕ under $SU(2)_L$. Furthermore, the fluctuations around its VEV $\tilde{\phi}_0$ can be written as:

$$\tilde{\phi}(x) = \frac{1}{\sqrt{2}}\begin{pmatrix} v+h(x) \\ 0 \end{pmatrix} \ . \tag{1.18}$$

[14] As of this writing, $n = 3$.

However, the rotation in the generation space induced by (1.20) affects the charged hadronic current. In fact, recalling (1.4)

$$J^\mu = \overline{\mathrm{Q}}\gamma^\mu\tau^+\mathrm{Q} = \overline{u}_L\gamma^\mu d_L = \overline{u}^0_L U^\dagger_L\gamma^\mu V_L d^0_L = \overline{u}^0_L\gamma^\mu U^\dagger_L V_L d^0_L \equiv \overline{u}^0_L\gamma^\mu V_{CKM} d^0_L \ ;$$

V_{CKM} is known as Cabibbo-Kobayashi-Maskawa matrix and describes the mixing amplitude in flavour changing currents[15] [12],[13].

A different behaviour is on the other hand predicted for leptons. The difference is essentially due to the $\nu_{\ell R}$ carrying no electroweak quantum numbers, therefore forbidding any Yukawa coupling involving $\bar{\phi}$. This implies the existence of only one mass matrix, h_{E}, which can be diagonalized by the biunitary transformation

$$V^{\ell\dagger}_L h_{\mathrm{E}} V^\ell_R = diag(h^1_{\mathrm{E}}, h^2_{\mathrm{E}}, \dots, h^{\mathrm{n}}_{\mathrm{E}})$$

(where h^f_{E} are required to be real and non-negative), which identifies the leptonic mass eigenstates

$$\ell_L = V^\ell_L \ell^0_L \ , \quad \ell_R = V^\ell_R \ell^0_R \ ;$$

at the same time, assuming ν_ℓ massless, the same transformation holds for the left-handed neutrino:

$$\nu_{\ell L} = V^\ell_L \nu^0_{\ell L} \ .$$

This makes the leptonic term in (1.19)

$$\mathcal{L}^{lept}_{Yuk} = -\frac{1}{\sqrt{2}}(v+h)\sum_{f=1}^{\mathrm{n}}\left(\overline{\ell}^0_{fL} h^f_{\mathrm{E}} \ell^0_{fR}\right) + h.c.$$

clearly diagonal, while leaving weak charged currents unaffected

$$J^\mu = \overline{\mathrm{L}}\gamma^\mu\tau^+\mathrm{L} = \overline{\nu}_{\ell L}\gamma^\mu\ell_L = \overline{\nu}^0_{\ell L} V^\dagger_L\gamma^\mu V_L \ell^0_L = \overline{\nu}^0_{\ell L}\gamma^\mu V^\dagger_L V_L \ell^0_L = \overline{\nu}^0_{\ell L}\gamma^\mu\ell^0_L \ .$$

Similarly to quarks, charged leptons masses are

$$m^f_\ell = \frac{h^f_{\mathrm{E}} v}{\sqrt{2}} \ ,$$

in terms of which their couplings to H^0 can be expressed:

$$\mathrm{H}^0\bar{\ell}\ell \sim \frac{m_\ell}{v} \ . \tag{1.22}$$

1.2 The role of the top quark in the Standard Model

Quarks and leptons constitute the basic building blocks of matter in the Standard Model. There are three generations of quarks and lepton in the model, with identical quantum numbers but different masses. Within each generation, quarks and leptons appear in pairs

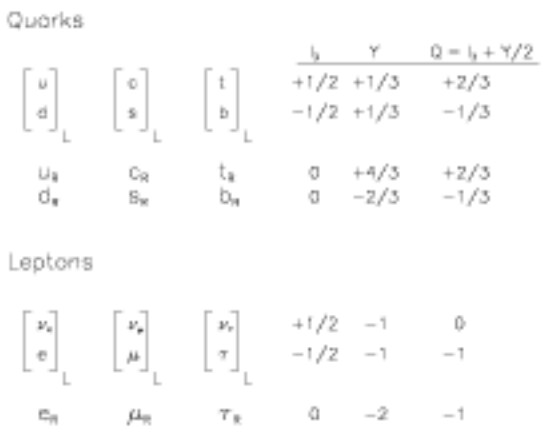

Figure 1.9: *Leptons and quarks in SU(2)×U(1). Also shown are the values for the SU(2) weak isospin (I_3), U(1) weak hyperchange (Y) and electric charge (Q).*

(see fig. 1.9). The left-handed quarks form weak-isospin doublets, with the electric charge Q=+2/3 and Q=-1/3 quarks having weak isospin I_3=+1/2 and -1/2 respectively.

The tau lepton (τ) was the first particle of the third generation to be discovered. A short time later, in 1977, the Υ was discovered at Fermilab as a resonance in the $\mu^+\mu^-$ invariant mass spectrum in the reaction p + nucleon $\rightarrow \mu^+\mu^-$ + X. This resonance was interpreted as a $b\bar{b}$ bound state (the Υ), wich subsequently decays into muon pairs.

In the past twenty years a tremendous amount of experimental data on the properties of the b quark and of b-flavored hadrons have become available, mostly from experiments at e^+e^- colliders. Both the charge and the weak isospin of the bottom quark are by now well established (Q_b= -1/3 and I_3= -1/2).

The value of the charge was first inferred from measurements of the Υ leptonic width at the DORIS e^+e^- storage ring. This width is proportional to the square of the charge of the b quark (see fig. 1.10) and can be quantitatively estimated from heavy quark-antiquark potential models.

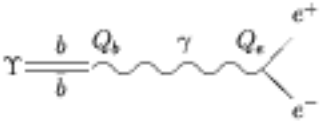

Figure 1.10: *Feynman diagram for* $\Upsilon \rightarrow e^+e^-$.

The charge assignment was subsequently confirmed by the measurement of the ratio R=$\sigma(e^+e^- \rightarrow \text{hadrons})/\sigma(e^+e^- \rightarrow \mu^+\mu^-)$.

[15] At tree-level, these processes can be described by charged current phenomena only. In fact, the detected suppression of flavour changing neutral currents (FCNC) lead to quark $SU(2)$ doublets through the GIM mechanism [11].

At lowest order and ignoring resonance effects, R= $\sum_{quarks} 3Q_q^2$, where the factor of three arises from the fact that quarks come in three colors. The sum is over all quarks that can be produced all quarks with mass below one-half the center-of-mass energy of the e^+e^- system.

The weak isospin of the b quark was first extracted from the forward-backward asymmetry (A_{FB}) in $e^+e^- \to b\bar{b}$. This asymmetry is defined in terms of the b-quark production cross section $\sigma(b)$ as

$$A_{FB} = \frac{\sigma(b, \theta > 90°) - \sigma(b, \theta < 90°)}{\sigma(b, \theta > 90°) + \sigma(b, \theta < 90°)} \tag{1.23}$$

where θ is the polar angle of the b quark in the e^+e^- center of mass as measured from the direction of flight of the e^-.

The asymmetry originates from the coupling of the Z to fermions, which in the Standard Model depends on the weak isospin through a term in the Lagrangian of the form $\overline{f}\gamma_\mu(g_V - g_A\gamma_5)Z^\mu f$, where f is the fermion spinor and the vector and axial couplings g_V and g_A are given by

$$g_V = \frac{I_3 - 2Qsin^2\theta_W}{2sin\theta_W cos\theta_W} \tag{1.24}$$

$$g_A = \frac{I_3}{2sin\theta_W cos\theta_W} \tag{1.25}$$

where θ_W is the Weinberg angle. The first measurement of A_{FB} was performed in the mid-eighties and was found to be consistent with the Standard Model prediction. Alternative isospin assignments for the bottom quark were also found to be inconsistent with the observed suppression of the flavor-changing neutral-current decays of B mesons.

If the b quark formed a weak-isospin singlet and if there were only five quarks (u, d, c, s, b), then it can be shown that the branching ratio $\mathcal{B}(B \to Xl^+l^-)$ $\geq$0.12 and $\mathcal{B}(B \to Xl\nu) \approx 0.026$. This was soon found to be inconsistent with the first upper limits placed on flavor-changing neutral currents in b decays, $\mathcal{B}(B \to Xl^+l^-)$ <0.008 at 90% C.L.

The I_3= -1/2 isospin of the bottom quark implies the existence of an additional quark, the top quark, as the third-generation weak-isospin partner of the bottom quark. Furthermore, the existence of such a third-generation quark doublet, in conjunction with the presence of three lepton generations, ensures the necessary cancellations in diagrams contributing to triangle anomalies.

For the electroweak theory to be renormalizable, the sum over fermions for diagrams like that displayed in fig. 1.11 should vanish. The contributions to this diagram for each fermion in the theory is proportional to $N_c g_A^f Q_f^2$, where the factor N_c=3 is the number of colors and applies to quarks only. Hence the contribution from a lepton isodoublet exactly cancels that of a quark isodoublet. With three lepton generations, the existence of a third quark isodoublet, whose members are the top and bottom quarks, results in the desired cancellation of triangle anomalies.

Measurement of the Z width at the LEP and SLC colliders rule out the existence of a fourth-generation neutrino with mass $M_\nu \leq M_Z/2$. Unless the fourth-generation neutrino is very massive, no additional generations are allowed in the context of the Standard Model. The top quark is therefore the last fermion expected in the Standard Model.

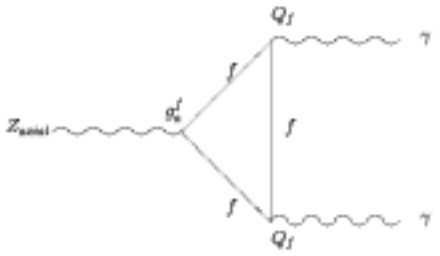

Figure 1.11: *An example of a fermion triangle diagram that could cause an anomaly.*

Only the Higgs boson is left to be discovered in order to complete the particle and field content of the minimal Standard Model.

While the Standard Model predicts the charge and weak isospin of the top quark (Q=2/3 and I_3=1/2), its mass remains a free parameter. The recent top mass measurements yield $M_{top} = 174.3 \pm 5.1$ GeV/c^2[14] a factor of 40 higher than the mass of the second-heaviest fundamental fermion (the b quark). The reason for such a high mass is a mystery of the Standard Model. It does, however, occur quite naturally in local supersymmetric theories where the electroweak symmetry is broken through radiative corrections.

The value of the top mass enters in the calculation of radiative corrections to a large number of electroweak observables. The level of precision achieved in these measurements is a good enough that a comparison between the measured top mass and the calculation of electroweak radiative corrections provides a stringent test of electroweak theory and is sensitive to physics beyond the Standard Model.

1.3 Top quark production

Because of its large mass, the top quark can only be observed directly in collider experiments where sufficiently high center-of-mass energies are achieved. In electron-positron collisions, top quark are produced in pairs via a photon or a Z. Since at lowest order this is a purely electroweak process, the cross section and production kinematics can be precisely predicted, but at present no e^+e^- collider has reached a sufficient energy.

Significantly higher center-of-mass energies have been achieved at hadron colliders: top quarks are produced by colliding partons (quarks, gluons, and antiquarks) from protons and antiprotons. There are three mechanisms for top production in $p\overline{p}$ collisions:

- pair production of top quark, $p\overline{p} \rightarrow t\bar{t} + X$. The leading-order Feynman diagrams for this process are shown in fig. 1.12. At higher order, gluon-quark initial states also contribute. $t\bar{t}$ pairs can also be produced through a Z or a photon, but with a much smaller cross section.

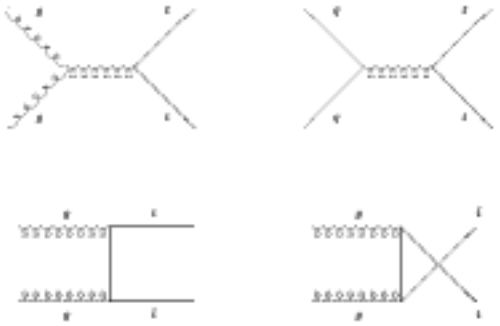

Figure 1.12: *Lowest-order Feynman diagrams for production of $t\bar{t}$ pairs in $p\bar{p}$ collisions.*

- Single top quark production is dominated by two processes: the s-channel W^*(W virtual) and the t-channel W-gluon fusion process. The cross section is proportional to the CKM matrix element V_{tb}^2 (see fig. 1.13).

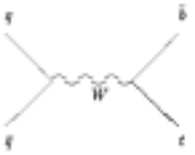

Figure 1.13: *Lowest-order Feynman diagrams for Drell-Yan production of $t\bar{b}$ pairs in $p\bar{p} \to W^* \to t\bar{b}$.*

- single top quark production via W-gluon fusion (see fig. 1.14). Photon-gluon and Z-gluon fusion are also allowed with a much lower cross section.

Figure 1.14: *Lowest-order Feynman diagrams for production of a single top quark via W-gluon fusion in $p\bar{p}$ collisions.*

At the Fermilab Tevatron the strong interaction pair-production process ($p\bar{p} \to t\bar{t}$) is the dominant one for a wide range of top masses. Furthermore, among all lowest order diagrams of fig. 1.12, the quark annihilation one ($q\bar{q} \to t\bar{t}$) provides the majority ($\approx 90\%$) of the production cross section.

The pair-production cross section for heavy quarks such as the top can be calculated in perturbative QCD. It is factorized as a product of the parton distribution functions

inside the protons and the parton-parton point-like cross section, and is written as a sum over contributions from partons inside the proton and antiproton:

$$\sigma(p\bar{p} \to t\bar{t}) = \sum_{i,j} \int dx_i F_i(x_i, \mu^2) \tag{1.26}$$

$$\times \int dx_j F_j(x_j, \mu^2) \hat{\sigma}_{ij}(\hat{s}, \mu^2, M_{top}) \tag{1.27}$$

The functions F_i and F_j are the number densities of light partons (quarks, antiquarks and gluons) evaluated at a scale μ in the proton and antiproton; x_i and x_j are the momentum fractions of the incoming partons, $\hat{\sigma}_{ij}$ is the point-like cross section for $i+j \to t\bar{t}$ and $\hat{s} = x_i x_j s$ is the square of the center-of-mass energy of the parton-parton collision.

The factorization and renormalization scale μ is an arbitrary parameter with the dimension of an energy, which is introduced in the renormalization procedure. The exact result for the cross section should be independent of the value of μ, however, since calculations are performed to finite order in perturbative QCD, cross section predictions are in general dependent on the choice of the scale, which is usually taken to be of the order of M_{top}. The sensitivity of perturbative calculations to reasonable variations in μ is used to estimate the accuracy of the prediction. Parametrizations of the parton number densities (F_i and F_j) are extracted from fits to a large number of experimental results, mostly from deep-inelastic scattering.

The cross section for $p\bar{p} \to t\bar{t}$ can also be written as

$$\frac{d\sigma}{d\tau} = \sum_{ij} \frac{dL_{ij}}{d\tau} \hat{\sigma_{ij}}(\hat{s}, \mu^2, M_{top}) \tag{1.28}$$

where $\tau = \hat{s}/s$ and $dL_{ij}/d\tau$ are the differential parton luminosities.

The reliability of the modelling of $t\bar{t}$ production is an important issue. Top production is usually modelled using a QCD-shower Monte Carlo program, such as ISAJET, HERWIG or PYTHIA.

In all these Monte Carlo programs, the initial hard scatter is generated from tree-level matrix elements convoluted with parametrizations of the parton distribution functions. Initial and final state partons are then developed into a gluon and $q\bar{q}$ radiation cascade. The QCD shower is terminated when the virtual invariant mass of the parton in the cascade becomes smaller than a minimum value at which point QCD is expected to break down.

The main differences between these Monte Carlo event generators are in the modelling of the radiation processes. ISAJET implies an independent fragmentation model, i.e., radiation from each parton occurs independently from the structure of the rest of the event, whereas in both HERWIG and PYTHIA the radiation is more realistically emitted taking into account color correlations between all partons in the initial and final states. The output of these Monte Carlo event generators consists of a list of stable particles which can be fed to a detector simulation for detailed studies of the expected signature of a top event.

1.3.1 Top quark hadronization

Quarks are not observed as free particles but are confined to form hadronic bound states. The top quark, however, is unique in that its mass is high enough that it decays before hadronization. According to the Standard Model, top quarks undergo the weak decay $t \to Wb$, where the W boson is real if $M_{top} > M_W + M_b$, and virtual otherwise.
Decay modes such as $t \to Ws$ and $t \to Wd$ are also allowed. They are suppressed by factors of $|V_{ts}|^2/|V_{tb}|^2 \approx 10^{-3}$ and $|V_{td}|^2/|V_{tb}|^2 \approx 5 \times 10^{-4}$ where, respectively, V_{ij} is the Cabibbo-Kobayashi-Maskawa (CKM) mixing matrix element.
The expected width of the top quark, and hence the lifetime as a function of its mass, is shown in fig. 1.15.

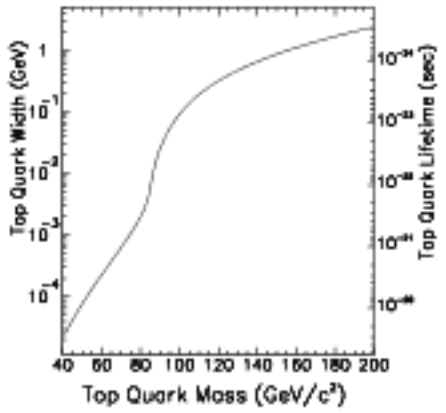

Figure 1.15: *The Standard Model width of the top quark as a function of its mass.*

The hadronization process is not well understood. However, the formation of hadrons is estimated to take place in a time of the order $\Lambda_{QCD}^{-1} \approx O(100MeV)^{-1} \approx O(10^{-23})$ seconds.
As can be seen in fig. 1.15 the top lifetime becomes shorter than this characteristic time if the top mass is higher than approximately 100 GeV/c^2.
The exceeedingly short top quark lifetime is due not only to the very high mass but also to the fact that $M_{top} > M_b$, so that the top can decay into Wb and this decay mode is not CKM suppressed.
Even if hadronization effects do occur in $t\bar{t}$ production, they, although potentially, are not expected to be experimentally observable. The reason is that the fragmentation of heavy quarks is hard, i.e., the fractional energy loss of the top quark as it hadronizes is small. Distorsions to the kinematics of the top quark from the perturbative partonic calculation are minimal. Additional particles produced in the hadronization process have little effect on the overall event topology.
If a top hadron is indeed produced, the kinematics of the top decay will not be very different from that of a free quark decay, since the companion quark is so much lighter.

1.3.2 Underlying event

After the hard collision, the remnants of the proton/antiproton also hadronize. This process cannot be described within the framework of perturbative QCD and is therefore

poorly understood. The particles from the remnant hadronization are usually referred to as the *underlying event*. The structure of the underlying event is similar to that of the bulk of soft $p\bar{p}$ collisions (the so called minimum bias events).
Minimum bias events are events collected with a simple interaction trigger. This trigger usually consists of a coincidence between large banks of scintillator counters in the very forward and backward regions and is highly efficient for all types of inelastic $p\bar{p}$ collisions. In minimum bias events the average transverse momentum of the hadrons is $< P_T > \approx 500$ MeV/c.
Most of energy is carried away by particles that remain inside the beam pipe and are not seen in the detector. The charged particle multiplicity in the central region per unit pseudorapidity ($dN^{ch}/d\eta$) grows approximately logarithmically with the center of mass energy.

1.4 Top quark decay

Since the top quark decays with a very short lifetime, only its decay products can be detected.
According to the Standard Model the top quark decays as $t \to Wb$ where the W boson is real or virtual depending on the top mass.
Typical final states for the leading pair-production process therefore belong to three classes:

1. $t\bar{t} \to WbW\bar{b} \to q\bar{q}'bq''\bar{q}'''\bar{b}$,

2. $t\bar{t} \to WbW\bar{b} \to q\bar{q}'b\ell\bar{\nu}_\ell\bar{b} + \bar{b}\nu_\ell bq\bar{q}'\bar{b}$,

3. $t\bar{t} \to WbW\bar{b} \to \bar{\ell}\nu_\ell b\ell'\bar{\nu}_{\ell'}\bar{b}$,

where 1,2 and 3 are referred to as the all-hadronic, lepton + jets and dilepton channels respectively. The quarks in the final state can emit radiation and eventually evolve into jets and hadrons. The precise number of jets reconstructed by the detectors varies event by event.

1.4.1 Dilepton Mode

In this channel, both W's decay leptonically ($W \to l\mu$) and we search for leptonic W decays to an electron or a muon[16] . The nominal signature in this channel requires two high-P_T leptons, missing transverse energy (from the two neutrinos) and two jets from the b-quarks.
Acceptance for this channel is small mostly due to the product branching ratios of both W's decaying leptonically ($BR(W \to l\nu) \times BR(W \to l\nu) \approx 5\%$). Backgrounds however are very small. Although not *a-priori* part of the search, we examine the jets in dilepton events for indications that they originated from b quarks.

[16]Decays into τ's lead to a more complicated experimental signature and are not usually considered in this channel

1.4.2 Lepton + Jets Mode

In this channel, one of the W's decays leptonically to either an electron or muon[17] (plus neutrino) and the other W decays decays hadronically to a pair of quarks. The nominal signature is a lepton, missing transverse energy and four jets: two from the b quarks and two from the decay of the W. Approximately 30% of the $t\bar{t}$ events have this decay signature.
The background from W+multijet production is large. However, $t\bar{t}$ events contain two b quarks jets and these can be distinguished from gluon and light quark jets in the background using two b quark tagging techniques. The first technique locates a displaced vertex using the silicon vertex detector (SVX Tag).
The second locates a low P_T electron or muon primarily from the semileptonic decay of a b quark or sequential c quark (SLT Tag).
The first technique looks for displaced vertices, while the second one locates low-P_T electrons or muons from the semileptonic decays of b quarks (or sequential c quarks).

1.4.3 All Hadronic Mode

In this channel both W bosons decay into quark-antiquark pairs, leading to an all hadronic final state, containing no hogh P_T leptons, and with a total branching ratio of about 4/9 into quark-antiquark pairs, leading to an all hadronic final state, containing no high P_T leptons.
Since the expected decay signature involves only hadronic jets, a very large background from standard QCD multijet production is present and dominates over $t\bar{t}$ production. To reduce this background it is important to search for a b quark decays with a displaced secondary vertices.

1.5 Production Cross section $\sigma_{t\bar{t}}$

An accurate measurement of the $t\bar{t}$ production cross section is a precision test of QCD. A cross section which is significantly higher than the theoretical expectation would be a sign of non-Standard Model production mechanisms, for example an anomalous couplings in QCD.
In order to correctly evaluate the acceptance, the reliability of the jet counting and b tagging are important issue. With 2 fb^{-1} of data it will be possible to measure the b tagging efficiency in top events, using dilepton events selected without a b tag and the ratio of single to double tags in lepton+jets events. These studies will give uncertainties that scale with $\sqrt{N}$.
With large samples, one can measure the bottom and charm content as a function of jet multiplicity in W + jet events using the $c\tau$ distribution of the tagged jets and use this to tune the Monte Carlo models for W+ $\geq$ 3-jet backgrounds.
Accounting for all effects the total $t\bar{t}$ cross section at $\sqrt{s} = 1.8$ TeV, measured by CDF, with 110 pb^{-1} of data (Run I) is $6.5^{+1.7}_{-1.4}$ pb [15], to be compared to the value measured by D0, $5.69 \pm 1.21 \pm 1.04$ pb[16]. At $\sqrt{s} = 2$ TeV we expect a slightly larger cross section.

[17] Again decays into τ's are not considered to be part of this channel

Theoretical calculations[17] give $\sigma_{t\bar{t}}(\sqrt{s} = 2 \text{ TeV}) = 7$ pb. For the 2 fb^{-1} of Run II we expect a precision of about 9%. This will challenge QCD, and provide a sensitive test for non standard production and decay mechanisms.

1.6 Top quark Mass

The top quark mass will be one of the most important electroweak measuerement made at the Tevatron. In combination with the W mass, m_{top}, constrains the mass of the Standard Model Higgs boson. Fig.1.16 shows how the top and W mass measurements constrain the Higgs mass. In the figure, the uncertainty on the top mass is taken as 4 GeV/c^2.

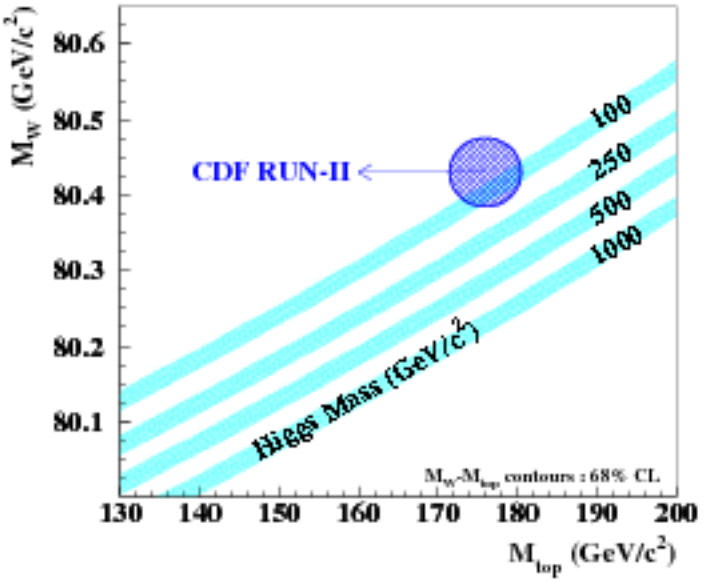

Figure 1.16: *W and top masses expected for 2 fb^{-1}. Different values of Higgs mass are shown.*

CDF measures the top mass in all three channels obtaining an average value of 176.1±6.6 GeV/c^2[18]. D0 measures top mass using the single and double lepton channels with an average of 172.1±7.1 GeV/c^2[19]. The combination of the two measurements amounts to 174.3±5.1 GeV/c^2. Currently, the statistical and systematic uncertainties on CDF's top mass measurement are both about 5 GeV. The statistical uncertainty scales as $1/\sqrt{\int \mathcal{L}dt}$, so in Run II the uncertainty will be dominated by systematics.
Almost all of the systematic uncertainties in the top mass measurement are coupled to the reliability of the Monte Carlo models for the mass spectrum for signal and background events. Assuming the model is accurate, most of the uncertainty is related to resolution effects. Instrumental contributions include calorimeter nonlinearity, losses in cracks, dead zones and the uncertainty of the absolute energy scale. A larger and more difficult part of the energy uncertainty concerns the reliability of the extrapolation to parton energies.

If all systematic effects can be measured the systematic uncertainties should also scale as $1/\sqrt{\int \mathcal{L}dt}$ and in this case the systematic error would be reduced to $\approx 2\ GeV/c^2$.

Bibliography

[1] E. Fermi, *Z. Physik* **88**, 161 (1934).

[2] F. Mandl, G. Shaw, *"Quantum Field Theory"*, John Wiley & Sons (1996).

[3] M. E. Peskin, D. V. Schroeder, *"An Introduction to Quantum Field Theory"*, Addison-Wesley (1997).

[4] C. N. Yang, R. L. Mills, *Phys. Rev.* **D 50**, 1173 (1954).

[5] S. Glashow, *Nucl. Phys.* **22**, 579 (1961).

[6] S. Weinberg, *Phys. Rev. Lett.* **19**, 1264 (1967).

[7] A. Salam, *Elementary Particle Theory: Relativistic Groups and Analicity*, Proc. of the 8th Nobel Symp., p. 367, ed. N. Svartholm, Almqvist and Wiksell, Sweden (1968).

[8] G. 't Hooft, *Nucl. Phys.* **B 33**, 167 (1971).

[9] P. W. Higgs, *Phys. Lett.* **12**, 132 (1964); *Phys. Lett.* **13**, 508 (1964).

[10] G. Ridolfi, *"An Introduction to the Standard Model of Electroweak Interactions"*, lecture notes.

[11] S. Glashow, J. Iliopoulos, L. Maiani, *Phys. Rev.* **D 2**, 1285 (1970).

[12] N. Cabibbo, *Phys. Rev. Lett.* **10**, 531 (1963).

[13] M. Kobayashi, K. Maskawa, *Progr. Theor. Phys.* **49**, 652 (1973).

[14] K. Hagiwara et al., (Particle Data Group), *Phys. Rev.* **D 66**, 010001 (2002).

[15] CDF Collaboration, T. Affolder *et al.*, *Phys. Rev.* **D 64**, 032002 (2001).

[16] D0 Collaboration, B. Abbott *et al.*, *Phys. Rev.* **D 60**, 012001 (1999).

[17] R. Bonciani *et al.*, *Nucl. Phys.*, B529, 424 (1998), *hep-ph*/9801375.

[18] CDF Collaboration, T. Affolder *et al.*, *Phys. Rev.* **D 63**, 032003 (2001).

[19] D0 Collaboration, B. Abbott *et al.*, *Phys. Rev.* **D 58**, 052001 (1998).

Chapter 2

Tevatron and CDF upgrades for Run II

With the shutdown of LEP, occurred at the beginning of November 2000, Tevatron remains the only machine where collisions above the TeV-scale are observable, making this accelerator the best candidate for new physics discoveries until the start of LHC.

The machine and detectors setup for Run I were not optimal for these kind of searches, and the statistics was too small to achieve enough sensitivity on rare processes (like Higgs physics) whose limited production cross sections essentially reflect the smallness of the electroweak coupling constant and the high mass of the new particles involved. The ambitious physics goals that have been proposed for Run II therefore needed specific upgrades of both the accelerator complex and detector components.

This chapter describes the upgrades that the Tevatron accelerator and the CDF detector[1] have undergone, leaving to the following chapter the discussion of the optimization of physics tools in terms of the new detector setup.

2.1 The accelerator upgrade

The number of events which are expected for a given process is given by the expression:

$$N_{evts} = \sigma \cdot \int \mathrm{d}t\mathcal{L} \ ,$$

where σ is the cross section of the considered process and $\mathcal{L}$ is the experiment instantaneous luminosity. The N_{evts} can be increased in three ways:

1. performing the experiment in a situation that maximizes σ;
2. augmenting the experiment instantaneous luminosity;
3. increasing the running time of the experiment.

Being aimed at pursuing a larger statistics, the proposed upgrades for Tevatron, the accelerator facility at Fermilab, essentially follow the previous scheme. Steps 1 and 2 respectively translates into:

[1] Most of the information about the detector upgrades is contained in [1].

- ◇ increasing the center of mass energy of the $p\bar{p}$ collisions;
- ◇ increasing the luminosity of the accelerator.

Collision energy. As mentioned in the previous chapter, the Run II of Tevatron is characterized by a center of mass energy of $\sqrt{s}=2$ TeV, some 10% higher than in Run I; this enhances production cross sections for signals which are within the physics goals of Run II: for instance, $t\bar{t}$ and H^0V production cross sections are respectively $\sim 40\%$ and $\sim 30\%$ higher than in the Run I scenario.

Accelerator luminosity. While the collision energy influences the production cross section, the accelerator luminosity – related to the collision frequency – affects the datasets in the sense that determines the rate at which $p\bar{p}$ collisions occur. The instantaneous luminosity can be expressed as:

$$\mathcal{L} \propto \frac{f B N_{\mathrm{p}} N_{\bar{\mathrm{p}}}}{2\pi(\sigma_{\mathrm{p}}^2+\sigma_{\bar{\mathrm{p}}}^2)} \ ,$$

where:

f : beam revolution frequency,
B : number of proton/antiproton bunches,
$N_{\mathrm{p},\bar{\mathrm{p}}}$: number of protons/antiprotons per bunch,
$\sigma_{\mathrm{p},\bar{\mathrm{p}}}$: transverse proton/antiproton bunch dimension at interaction point,

while the proportionality is provided by a form factor depending on the beam longitudinal size and on its dispersion in phase space.

While maintaining the number of protons/antiprotons per bunch almost the same than in Run I, the most significant improvement towards high luminosities has been achieved by increasing the number of bunches from 6 to 36; this, together with reduced bunch sizes, is responsible for an expected instantaneous luminosity of $\sim 10^{32}\ cm^{-2}s^{-1}$ for Run II.

Two side-effects come as consequences of augmenting the number of bunches, affecting both detector operation and event reconstruction. First, a higher number of bunches reduces the time between collisions, which in turn implies a shorter time available for readout. According to the number of bunches, the crossing time decreases from 3.5 μs (Run I, 6 bunches) to 396 and 132 ns in Run II for 36 and 108 bunches respectively. This has a strong consequence on readout and triggering procedures: events collected by the detector need to be piled up in memory and fed to the trigger boards through a pipeline in order to avoid readout latency during processing. Secondly, more than one hard or semi-hard scattering can occur in a beam crossing; the average number $\overline{N}$ of interactions per beam crossing is determined by the number of bunches and by the instantaneous luminosity (see fig. 2.1).

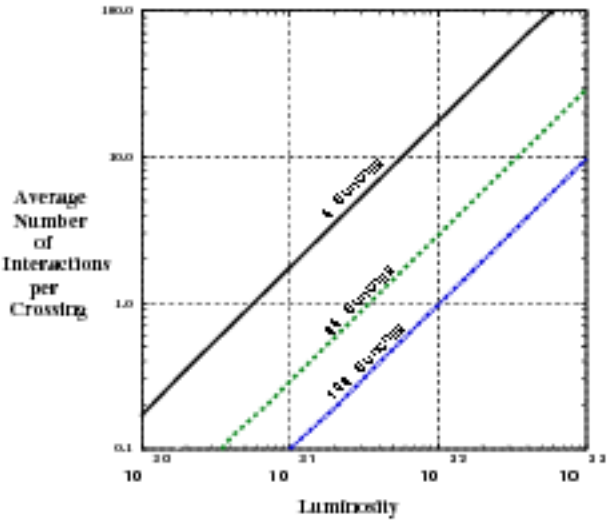

Figure 2.1: *Average number of interactions per beam crossing.*

In the following, a description of the various components of Tevatron in Run II configuration is provided.

2.1.1 Proton production and Booster

The proton source at Fermilab is composed by a 400 MeV linear accelerator 150 m long, the Linac, which is fed with 750 keV negative hydrogen ions by a Cockcroft-Walton accelerator. Exiting from the Linac, the two electrons are stripped off the ions when the latter traverse a thin sheet of graphite. The so-obtained protons are injected into a small synchrotron having a diameter of 150 m, the Booster, which accelerates protons to an energy of 8 GeV. At the same time, the Booster collects the protons into bunches, part of which are used for antiproton production.

2.1.2 The Main Injector

The bunches of protons produced in the Booster are injected into the Main Injector, a 3 km proton syncrotron, whose main function is accelerating protons and antiprotons to an energy of 150 GeV, ready to be injected into the Tevatron. Another feature of the Main Injector consists in its capability of decelerating antiprotons, a functionality which reveals very useful for recovering unused antiprotons when Tevatron is not in colliding mode.

The Main Injector replaces the Main Ring, in use during Run I, which, being initially planned for proton acceleration in fixed target experiments, was not optimal to be driven as an injector for the Tevatron due to its low phase space acceptance.

2.1.3 Antiproton production and cooling

Antiprotons are produced by dumping a 120 GeV proton bunch from the Main Injector onto a nickel target; the antiprotons produced in the collision are collected by a lithium lens, from which they emerge with an energy of ~ 8 GeV. The pulses of antiprotons are fed into the Debuncher Ring, where they are collected as a continuum and stochastically cooled; further cooling proceeds in the Accumulator, into which they are moved from the Debuncher Ring. When a sufficiently high number of antiprotons is available, they are cooled into a bunch and this is injected into the Recycler Ring.

2.1.4 The Recycler Ring

The Recycler Ring serves as an antiproton accumulating ring and is located in the same cavity hosting the Main Injector. The purpose of this device – which did not exist at all during Run I – is electron-cooling and storing the bunches of antiprotons produced by the Accumulator or recovered by the Main Injector until they are used again. This enables an efficient management of the antiproton bunches: on one hand, at the end of a run they are not dumped (as it used to be during Run I), while on the other – thanks to the architecture of the Recycler Ring, based upon permanent magnets – they can be stored without the risk of loosing the beam as a consequence of power losses or surges. The importance of this device is related to the limiting power of the antiproton production

on the colliding procedure at Fermilab: for this reason, the recycling of antiprotons can provide itself a factor two increase on the average integrated luminosity.

2.1.5 The Tevatron

The Tevatron is a 6 km $p\bar{p}$ circular collider: oppositely charged beams are arranged to circulate in opposite directions within the same beam pipe. The energy of proton and antiproton bunches is raised from 150 GeV (*i.e.*, the nominal value of the beam energy on exiting the Main Injector) to 1 TeV before beams are crossed[2] and collisions take place.

Exploiting the upgrades developed specifically for each component of the accelerator chain, the Tevatron will be capable of producing $p\bar{p}$ collisions at $\sqrt{s} = 2$ TeV with a luminosity that, after machine fine tuning, should reach the value of $\mathcal{L} \simeq 2 \times 10^{32}\ cm^{-2}s^{-1}$, which would allow the delivery of a total integrated luminosity of 2 fb^{-1} in approximately two years[3].

2.1.6 The Tevatron Monitors

The quality of the beams provided by the Tevatron needs to be constantly monitored in order to permit effective control of the physics processes taking place in the detectors; in particular, beam luminosity and loss, together with positioning and dispersion, need to be kept under control.

Luminosity monitor: although for Run II the instantaneous luminosity $\mathcal{L}$ is expecetd to undergo a factor ten increase, the average luminosity per bunch remains almost constant with respect to Run I. For this reason, a luminosity monitor based on the same technology used during Run I – that is, scintillator arrays placed on both sides of the interaction region – can be used in Run II. Luminosity is defined by considering time coincidences between particles (both in p and $\overline{\text{p}}$ directions) leaving the interaction point, while an estimate of beam losses can be given in terms of another time coincidence, fulfilled by particles moving through the interaction region in the proton *or* antiproton direction.

Beam position monitor: beam position and profile monitoring follows essentially the scheme used in Run I. In this picture, the tracking devices of each detector are engaged at the beginning of each data-taking fill for determining the beam average position, as well as their profiles and direction. This information is made immediately available to the Tevatron control room in order to optimize the accelerator performance.

2.2 The CDF II detector

The Collider Detector at Fermilab (CDF) has been upgraded in order to accommodate both the increased luminosity and the reduced time-interval between consecutive bunches, which require faster readout and triggering.

[2] Of the twelve beam crossing possible points, ten are avoided by means of electrostatic separators; the remaining two correspond to the CDF and D0 interaction points.

[3] At present the recycler is not yet completed, and the typical luminosity is of the order of 3-4$\times 10^{31} cm^{-2}s^{-1}$

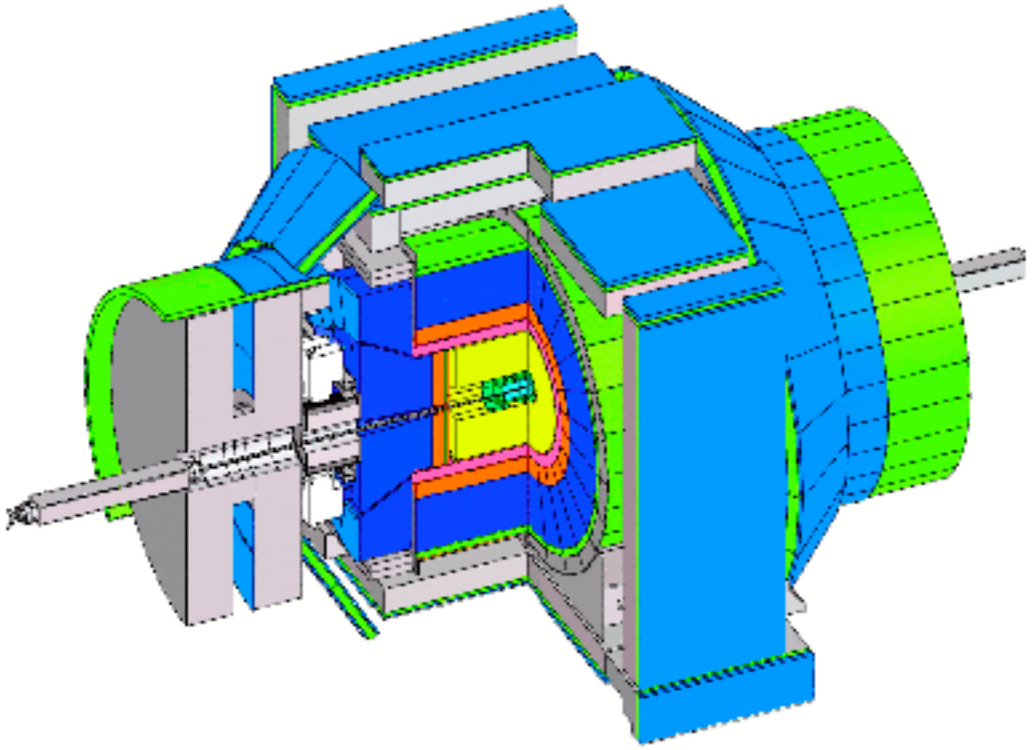

Figure 2.2: *The* CDF II *detector*

For these reasons all tracking devices, which are concentrated in the inner part of CDF, have been redesigned. At the same time, new readout electronics has been provided to all detector subsystems.

Furthermore, the long period of machine development (started in 1996) has permitted the review of the whole detector in terms of an acceptance increase, which has mainly interested the tracking, the calorimeter and the muon systems (whose increased geometrical coverage can be appreciated in fig. 2.2).

Before giving a brief description of CDF II subdetectors, it is convenient to define the two currently used coordinate systems.

Cartesian system: the z axis is coincident with the beamline, its positive direction parallel to the motion of protons. The xy plane contains the nominal interaction point, which coincides with the center of CDF. The x axis is oriented horizontally towards the outer side of the accelerator ring, while the y axis remains defined by requiring (x, y, z) to a be right-handed system.

Polar system: the origin of the system is the same as in the Cartesian case. The azimuthal angle ϕ is measured in the xy plane starting from the x axis, being positive in the anti-clockwise direction. The polar angle θ is measured from the positive direction of the z axis. Finally, r defines the transverse distance from the z axis. The *pseudorapidity*, defined in terms of θ as:

$$\eta = -\ln\left(\tan(\theta/2)\right) \ ,$$

is particularly useful at hadron colliders, where events are boosted along the beamline[4],

[4]The longitudinal momenta of the colliding partons are distributed according to the Bjorken x , therefore not leading to a complete cancellation of p_z in the collision.

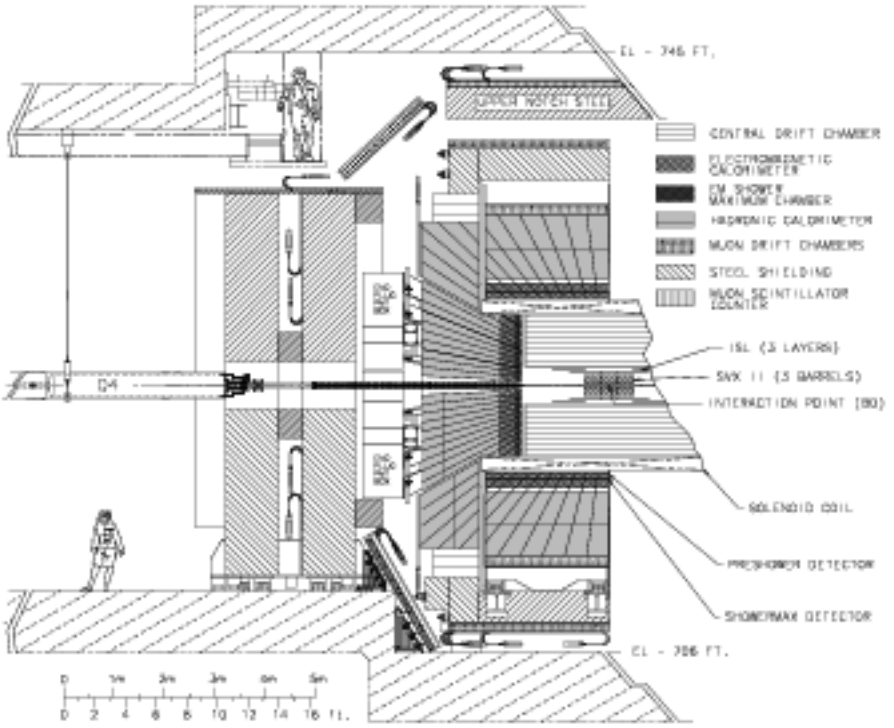

Figure 2.3: *$r-\phi$ view of the* CDF II *detector (half detector shown).*

since it transforms linearly under Lorentz-boosts:

$$\eta \longrightarrow \eta + \tanh^{-1}\beta$$

(having indicated with β the relative velocity associated to the boost). This implies that pseudorapidity gaps, $\Delta\eta$, are relativistic invariants, preserving in this way the average particle flux per unit of η. This fact has influenced the segmentation of the calorimetric apparatus.

2.2.1 The tracking system

The detector subsystems, enclosed in a superconducting solenoid providing a uniform magnetic field[5] of 1.5 T, are essentially dedicated to the reconstruction of the charged particles trajectories. The description of the each component of the tracking system is arranged according to an 'outside-in' scheme.

The Central Outer Tracker

The Central Outer Tracker (COT) is a new open-cell drift chamber, replacing the Central Tracking Chamber (CTC) that was unable to meet the necessary specifications needed for working in the typical Run II environment, where high occupancies and event rates are expected.

[5]The magnetic field produced by the solenoid is parallel to the beamline; its uniformity refers to a cylindrical fiducial volume $\sim$3.5 m long and $\sim$2.8 m wide.

From the mechanical point of view, the problem of occupancy has been solved by reducing the physical dimensions of the cells. This has been done by increasing by a factor of four the number of available cells. Each cell, containing an array of 12 sense wires, is tilted with respect to the radial direction (see fig. 2.4) by an angle which minimizes the drift time, which in the COT is ~ 5 times shorter than in the CTC. This result, obtained also by optimizing the gas mixture contained by the chamber volume, meets the necessity of completing the collection of showering electrons before the next bunch crossing.

The overall cell layout follows from the Run I configuration: cells are organized in eight *superlayers*, whose arrangement is visible in fig. 2.4. Even-numbered superlayers, equipped with axial wires, provide $r-\phi$ information, while $r-z$ information comes from the odd-numbered superlayers, whose wires are assembled with a small stereo angle ($\pm 3^\circ$). Since all cells contain 12 sense wires, stereo sampling in the COT is double than in the Run I CTC.

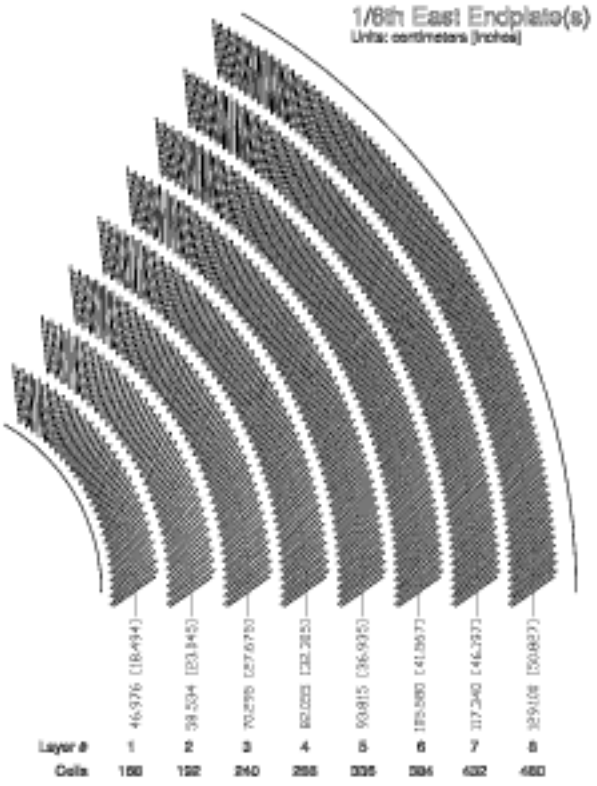

Figure 2.4: $\Delta\phi = 60^\circ$ *sector of* COT.

The COT, covering a radial region between 40 and 138 cm, is capable of tracking in the region with $|\eta| < 1$, provided that the track traversing its volume has $P_T \gtrsim 300\ MeV/c$.

The Intermediate Silicon Layers

The Intermediate Silicon Layers (ISL) detector is based on double-sided silicon crystals: one side of each crystal provides an axial (*i.e.* pure $r-\phi$) measurement, while the other one has stereo microstrips supplying z information.
The structure of this detector varies according to the η range:

- $|\eta| < 1$: a single layer of silicon crystals is placed at an average radius of ~ 22 cm;
- $1 < |\eta| < 2$: two layers of silicon crystals are placed at average radii of ~ 20 and ~ 29 cm.

The number of layers in the ISL ranges between one and two according to η to ac-

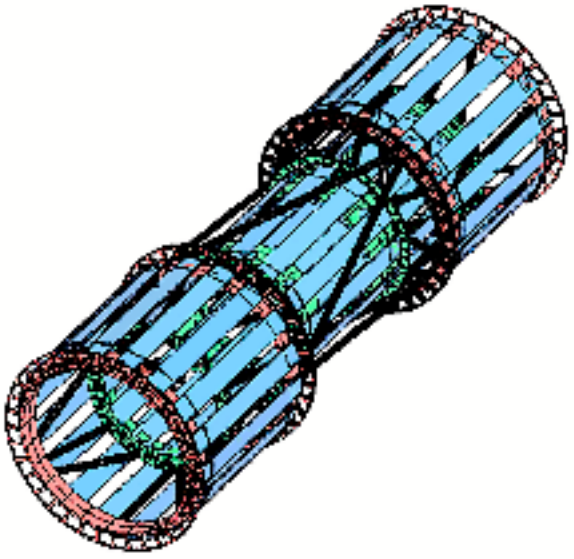

Figure 2.5: *Perspective view of* ISL.

commodate the possibility of stand-alone silicon tracking (in combination with SVX II – see next section and fig. 2.8) in the central region but also where COT information is incomplete or missing. In both cases, the contribution of ISL, thanks to its stereo sampling, enables a full three-dimensional reconstruction.

The Silicon Vertex Detector

The Silicon Vertex Detector (SVX II) is a five-layer detector wrapped around the beam pipe: layers, grouped into 12 ϕ-wedges, are placed at radii ranging from 2.5 and 10.6 cm (see fig. 2.6, where outermost radius is 12.9 cm). Each layer is assembled by means of double-sided silicon wafers. The detector is subdivided into three identical barrels, which are aligned along the beamline (see fig. 2.6), in order to provide adequate z coverage (± 45 cm from the nominal interaction point).

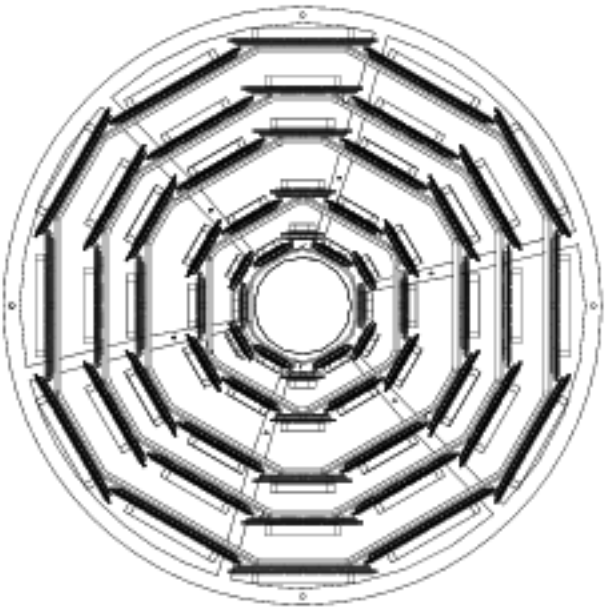

Figure 2.6: $r-\phi$ *view of* SVX II.

One side of all layers is characterized by axial microstrips, providing $r-\phi$ information. The other side of the layers, conversely, supplies $r-z$ information by means of stereo microstrips. Microstrips belonging to layers[6] 0, 1 and 3 have a 90° stereo angle; this angle reduces to 1.2° for the remaining layers.

SVX II provides information to a dedicated trigger system (SVT – see § 3.1.2), that performs a fast search for displaced tracks (*i.e.* tracks not originated in the primary vertex).

Layer 00

Layer 00 is a single-sided layer of silicon crystals placed on the outer side of the beam pipe at a radial distance of ~ 1.5 cm from the beamline (see figs. 2.7). It supplies $r-\phi$ information only, but its position makes it the perfect tool for increasing the track impact parameter resolution of the tracking system.

[6] Layers are numbered from 0 to 4 according to an 'inside-out' order.

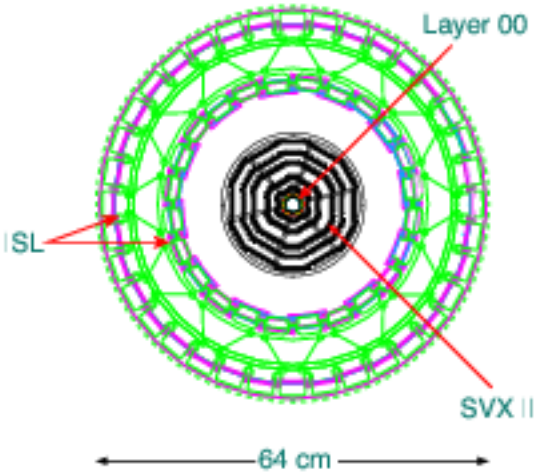

Figure 2.7: *r–φ view of silicon detectors.*

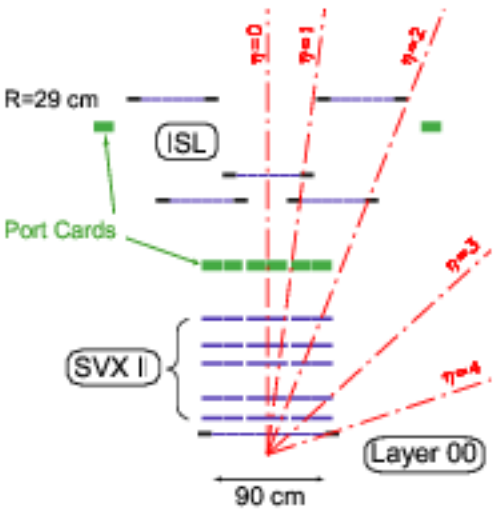

Figure 2.8: *r–z view of silicon detectors.*

2.2.2 The time of flight

Placed in the gap between the magnet and the outer wall of the COT, the detector for time of flight measurement [2] is essentially an array of scintillator bars ∼3 m long and ∼4 cm thick. The beam section is trapezoidal in shape, in order to better fit the cylindrical cavity they are supposed to fill, at the same time reducing the uninstrumented regions (*cracks*). The average bar width, on the other hand, turned out to be ∼4 cm in order to fulfill occupancy requirements.

Scintillator bars are read-out at both ends by photomultiplier tubes, both providing a time of passing and a pulse-height. The comparison of the readings performed at each end provides an estimate of the z-coordinate of the charged particle that traversed the scintillating material, which is then used for matching the time of flight determination – leading to particle identification – to a track reconstructed by the tracking system. The time of flight measurement is performed computing the time interval between the interaction and the signal in the scintillators.

2.2.3 The calorimeters

The calorimetry system consists of inner electromagnetic and outer hadronic sections, both segmented according to a common scheme which relies on azimuthal wedges ($\Delta\phi = 15^\circ$), each wedge corresponding to an array of towers projecting towards the geometrical center of the detector. The result is a cylindrical barrel providing almost full azimuthal acceptance and coverage up to $|\eta| \leq 3.64$.

The purpose of calorimetry is performing measurements of the energy[7] depositions released by charged and neutral particles leaving the tracking and magnet regions, as well

[7] Although calorimetry measurements provide estimates of $E = E_L + E_T$ (where E_L, E_T are defined with respect to the z axis), only transverse energy components (E_T) are relevant at hadron colliders. This is because the total energy of hard scattering processes emerging from $p\bar{p}$ collisions is variable due to the Bjorken x-dependence carried by the energy of each colliding parton.

as providing information about the missing transverse energy. As will be explained in the next chapter, this detector is of crucial importance also for *cluster* and *jet* reconstruction.

The central and endwall calorimeters

The central and endwall calorimeters, providing acceptance in the $|\eta|<1.1$ region ($|\eta|<1.2$ for hadronic section), have been retained almost unchanged from Run I, the only major upgrades being related to readout electronics. Each tower, corresponding to $\Delta\eta\times\Delta\phi=0.11\times15°$, is an independent sampling system consisting of alternating layers of lead and scintillator, backed by an iron-scintillator sandwich. The former, contributing a total thickness of ~ 18 radiation lengths[8] (X_0), is dedicated to the electromagnetic energy component, while the latter, corresponding to ~ 5 interaction lengths (λ_0), provides a measure of the hadronic energy.

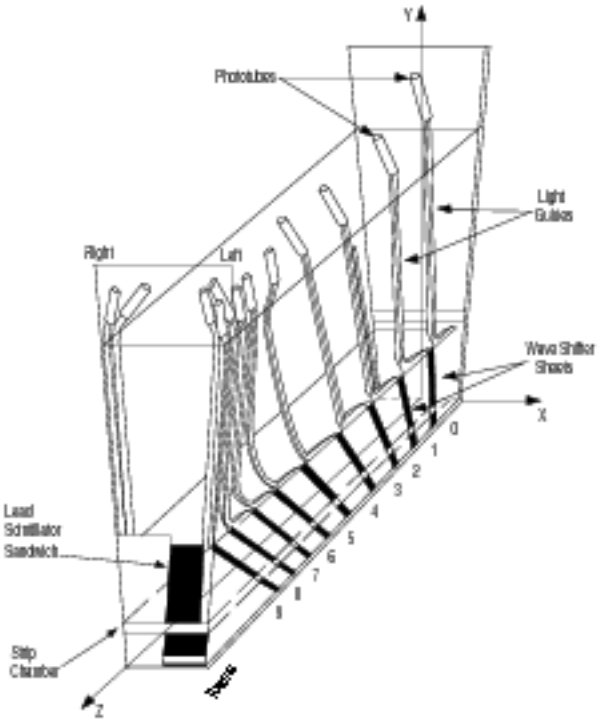

Figure 2.9: *Perspective view of central calorimeter half-wedge.*

Light pulses recorded in the various scintillator tiles are collected by wavelength shifters and carried outside the detector volume by light guides, where they are read by photomultiplier tubes. A perspective view of a central calorimeter half-wedge ($\eta > 0$) is depicted in fig. 2.9, where both the arrangement in projective towers and the light-gathering system (only the electromagnetic system is sketched) are visible. Energy resolutions achievable by this detector are influenced by their mechanical structure (sampling) and by stochastic fluctuations due to the photomultipliers response. Global estimates assign resolutions of $14\%/\sqrt{E_T[\mathrm{GeV}]}$ for electromagnetic and $75\%/\sqrt{E_T[\mathrm{GeV}]}$ for hadronic towers.

Two position detectors are included in each wedge of the central electromagnetic calorimeter:

Shower Maximum Detector: embedded within the lead-scintillator sandwich at a radial depth of $r = 184\,\mathrm{cm}$ [9], in correspondence to the maximum shower development, two-dimensional strip-wire chambers (CES, for Central Electromagnetic Strip chamber) provide position and pulse-height information about electromagnetic showers by measuring their charge deposition. Chamber geometry is usually described in terms of the local wedge-coordinate system defined in fig. 2.9: each half-wedge[10] hosts two CES modules, providing coverage in the $z=6.2\div121.2\,\mathrm{cm}$ and $z=121.2\div239.6\,\mathrm{cm}$ regions. Chambers are segmented along the z direction in strips having an approximate pitch of 2 cm, leading

[8] Equivalent to $\sim$1 interaction length.

[9] Equivalent to $\sim 5.9X_0$ (including coil, which contributes by $\sim 1X_0$).

[10] As previously mentioned, a half-wedge subtends a $\Delta\phi=15°$, $\eta\gtrless 0$ region.

to a total of 64 strip channels in each chamber module. A 32-wire array is coupled to each chamber module. Wires, with a $\sim 2.5\,\text{cm}$ spacing, are parallel to the z direction, providing in this way a 90° reading of the charge deposition with respect to strips. As will be discussed in the next chapter, CES can contribute effectively to increasing the purity of electromagnetic objects: besides providing a finer azimuthal segmentation than calorimeter towers, CES can reject early hadronic showers occurring in the outer portion of the electromagnetic towers.

Preradiator: (CPR) mounted in front of the innermost face of the electromagnetic towers, the preradiator consists of two wire chamber modules for each half-wedge. In practice, this device follows the same structure and wire arrangement provided to the CES wire chamber, the only difference being related to shorter wire spacing ($\sim 2.2\,\text{cm}$) to fit the projecting wedge profile and slightly reduced η-acceptance ($z = 7.14 \div 119.7\,\text{cm}$ and $z = 123.5 \div 235.76\,\text{cm}$ delimit the boundaries of active regions). The preradiator collects the charge depositions released by showers that initiate in the tracking or coil material. The information provided by this detector can be used for a further background rejection on selecting electrons or photons (which can be better separated from pions according to their average larger deposition in the CPR).

Although calorimeter response is fast enough to meet the tighter time requirements imposed by Run II, wire chambers associated to CES and CPR may need to undergo integration over several beam crossings; this, however, should not be a problem since the high granularity exhibited by these devices guarantees a low detector occupancy.

The plug calorimeters

The active material for the Run I plug calorimeter consisted of proportional tubes, whose time response could not be matched to the operational conditions of Run II. For this reason, this detector has been substituted by a new unit, whose $r-\phi$ section is depicted in fig. 2.10, which also shows its relative position within CDF. From a functional point of view, the upgraded plug calorimeters essentially follow the scheme of the central calorimeter, with both the electromagnetic and hadronic sections relying on alternating layers of absorbing material (lead and iron respectively) and scintillator tiles, leading to a thickness of $\sim 21 X_0$ ($\sim 1\lambda_0$) and $\sim 7\lambda_0$ in the two cases. As for the central calorimeter, scintillators are read out by photomultiplier tubes (placed on the outside of each end plug) receiving the light pulses through a complex of wave length shifters, which collect the signals from the tiles, and light guides.

The upgraded plug calorimeters provide acceptance throughout the region $1.10 < |\eta| < 3.64$. While the central calorimeter is characterized by an almost constant $\eta - \phi$ granularity, both the η and ϕ segmentation of the plug are variable: according to increasing η, $\Delta\eta$ ranges from 0.10 to 0.64 on approaching the beamline. At the same time, the azimuthal segmentation decreases from 7.5° to 15° at the boundary between the fifth and the fourth highest η towers.

Also in this case, the energy resolutions are the result of limited sampling performed by scintillating tiles and stochastic fluctuations affecting the photomultipliers. Electromagnetic and hadronic resolutions, respectively $16\%/\sqrt{E[\text{GeV}]}$ and $80 \div 90\%/\sqrt{E[\text{GeV}]}$, have been measured for single electrons and pions.

A **Shower Maximum Detector** (SMD) is embedded in correspondence of a radial depth of $\sim 6X_0$. Instead of relying on the wire-strip chamber technique used for the

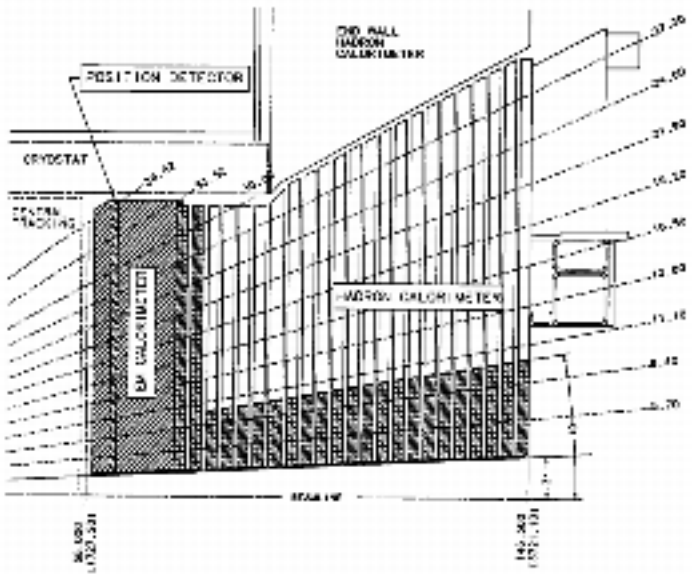

Figure 2.10: *$r-z$ view of plug calorimeter system.*

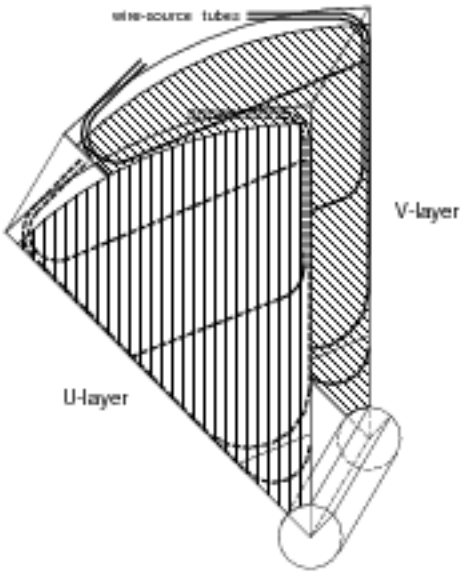

Figure 2.11: *Perspective view of plug shower maximum detector.*

central calorimeter, in this case arrays of scintillating strips have been chosen. The SMD is divided in eight 45° azimuthal sectors[11], each consisting of two layers (named U and V) of 5 mm pitch scintillating strips. Strips belonging to the same layer are oriented along a common direction coincident with one of the two sector radial boundaries (see fig. 2.11), in such a way that U and V strips form an angle of 45° among them, which enables two-dimensional position measurements. Furthermore, in order to reduce detector occupancy, on the basis of which the strip pitch has been optimized, η segmentation is provided to the strips (visible in fig. 2.11).
Light signals in this detector are collected by wavelength shifter fibers embedded in the strips and read-out by means of photomultiplier tubes placed at the rear of the plug calorimeter.

2.2.4 The muon system

Muon detectors are arranged in such a way to enclose the whole detector (see fig. 2.2). This arrangement is aimed at exploiting the fact that, being muons very penetrating particles, a natural separation from other charged tracks arises from inner detector shielding.

The muon system has undergone two substantial upgrades for Run II: first, a global increase in the acceptance, essentially achieved by extending Run I coverage to uninstrumented regions (see fig. 2.12). Second, the forward muon detection relies on the improved tracking capabilities, which allows momentum determinations based only on the central solenoidal field. For this reason, during Run II there will be no need for the toroidal fields. Instead, the steel toroids will provide mechanical support for the new forward detectors as well as adequate shielding. Furthermore, toroids will be pushed towards the central detector for increasing the acceptance also in the forward regions.

[11] Sectors segmentation is matched to tower boundaries.

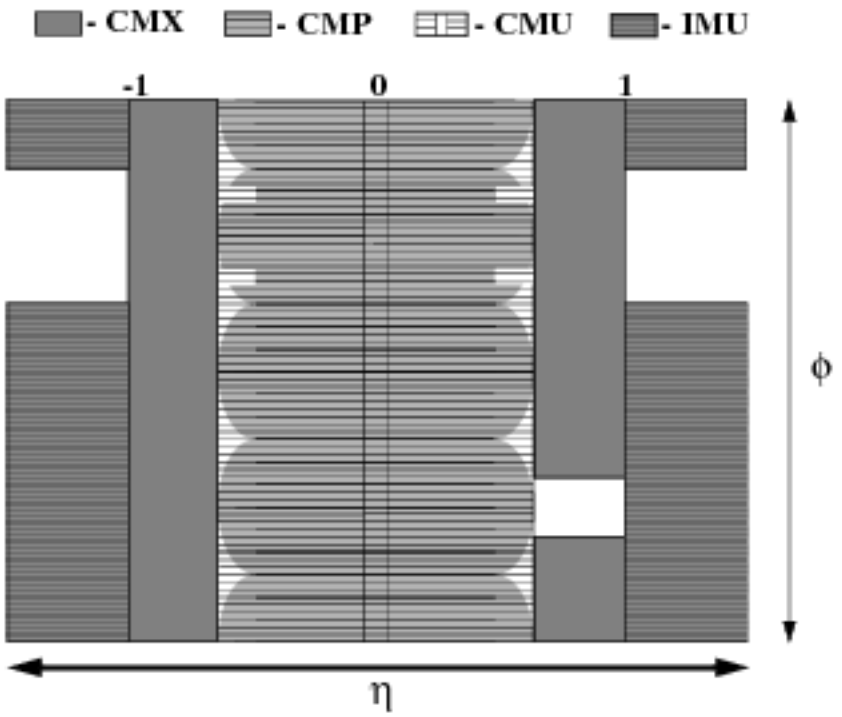

Figure 2.12: *Muon system $\eta-\phi$ map.*

The muon system consists of four subdetectors:

Central Muon Chambers (CMU), placed immediately outside the hadron calorimeter, are substantially unchanged from Run I. They consist of 144 modules each containing 16 6.35×2.68 cm rectangular drift cells stacked in four layers with a small azimuthal offset. Three such modules cover a half-wedge of the calorimeter, providing a global $|\eta| \lesssim 0.6$ coverage. Muons with $P_T \gtrsim 1.5\ GeV/c$ are able to traverse the whole calorimeter region and leave a signal in the CMU. Their position can be determined by merging the information coming from drift times (supplying ϕ) with a z coordinate estimated on the basis of charge division. Drift tubes will be driven in proportional mode with a maximum drift time of 800 ns.

Central Muon Upgrade (CMP) consists of a second set of four staggered layers of 2.5×15 cm drift tubes arranged behind an additional 60 cm of steel[12] according to a rectangular geometry (*i.e.*, they form a box around the central detector). The mismatch between the inner cylindrical structure and the outer box results in a curved acceptance boundary, which is evidenced in fig. 2.12. Muons must have $P_T \gtrsim 2.2\ GeV/c$ for reaching the CMP. Similarly to CMU, drift tubes are run in proportional mode (maximum drift time of 1.4 μs), but, on the contrary, they do not provide z information.

On the outer surface of CMP a layer of rectangular scintillator counters[13] is installed in such a way that each scintillator tile covers two drift cells in width and half a cell in length.

CMP acceptance has been increased by 17% for Run II.

Central Muon Extension (CMX) provides coverage in the $0.6 \lesssim |\eta| \lesssim 1$ by means of arrays of drift tubes arranged in conical sections, which are then positioned at each end of

[12] Provided by the magnetic field return yoke.

[13] These form the Central Scintillator Upgrade, or CSP.

the central detector and follow the CMP scheme. Drift tubes are embedded within two layers of scintillator counters[14]; four scintillator tiles cover a $\Delta\phi = 15^{\circ}$ range, with tiles being staggered between them in the two layers. Drift tubes, reachable by muons with $P_T \gtrsim 1.4\ GeV/c$, are operated in proportional mode with maximum drift time of $1.4\,\mu s$ and provide ϕ information; z information, on the other hand, is obtained from scintillator timing.
CMX will benefit of an improved acceptance by 45% in Run II.
Intermediate Muon Detectors (IMU) extend muon identification up to $|\eta| \leq 2$, providing at the same time trigger capabilities for $|\eta| \leq 1.5$. Placed on the outer surface of each toroid, its main structure consists of a barrel of drift chambers (run in proportional mode with a maximum drift time of 800 ns) coupled with scintillator tiles; the arrangement follows the CMP/CSP scheme. These detectors are reachable by muons with $P_T \gtrsim 1.4 \div 2.0\ GeV/c$.

The slow response of the muon system can be overcome by exploiting their high granularity, which, in principle, enables integration of signals collected by muon chambers over several beam crossings. This, however, is a feasible possibility only in case a strong reduction of the detector occupancy is achieved. During Run I, it was observed that most ($\gtrsim$95%) of the ionization detected in the muon system was originated by the Main Ring rather than by $p\bar{p}$ collisions and Tevatron beam halo. In Run II, this situation is expected to be much better, since, having replaced the Main Ring with the Main Injector and having provided stronger shielding from beam halo to the most exposed devices (CMX), should reduce the activity – and, therefore, the occupancy – of muon detectors. These side-improvements, together with the detector upgrades described above, are expected to produce an effective enhancement in the performances of the muon system in Run II.

[14] Central Scintillator Extension or CSX.

Bibliography

[1] F. Abe *et al.* (The CDF II Collaboration), *"The CDF II Detector Technical Design Report"*, FERMILAB-PUB-96-390-E, Oct 1996.

[2] The CDF Collaboration, *"A Time of Flight System for CDF"*, CDF internal note 2573, Feb 1994.

Chapter 3

The Trigger system and Data Production

At $\sqrt{s}=2$ TeV, the inelastic cross section for $p\bar{p}$ scattering is 56 mb, which, in terms of rate, means 5.6 million collisions per second for a typical instantaneous luminosity of $10^{32}\ cm^{-2}s^{-1}$ expected for Run II. This value has to be compared with the typical rate for processes of high interest at hadron colliders, respectively 7×10^{-4} Hz for top (corresponding to $\sigma=7$ pb for $M_{\mathrm{t}}=175\ GeV/c^2$) and 3×10^{-5} Hz for Higgs production (corresponding to $\sigma=0.26$ fb for $M_{\mathrm{H}}=120\ GeV/c^2$).

The overwhelming abundance of $p\bar{p}$ collisions, therefore, requires data-taking being controlled by a mechanism that filters out all events which do not present the characteristic signatures of the physical processes one is interested in. This mechanism is known as trigger system and essentially consists of a collection of specific hardware modules driven by speed-optimized software capable of performing a selection on the basis of pattern recognition and reconstruction.

Events which are selected by the trigger system are saved permanently on a mass storage device and subsequently fully reconstructed offline.

3.1 Trigger primitives

The trigger system is organized according to a three-level architecture. The output of each level is feeded as input into the next level. The underlying philosophy of this procedure consists essentially in reducing the rate at lower levels by means of very conservative requirements aimed mainly at reducing the dead time, enabling in this way more sophisticated selections to be performed at higher levels.

For each level, a set of primitives, essentially physics objects directly measured by the detector (such as energy depositions in the calorimeter) or obtained from them by running some algorithm (such as jets), is defined. According to the signal one wants to isolate, specific requirements are applied to a subset of primitives available at a given level; this sets the trigger for that level.

The maximum allowed rate for a given level (which is often referred to as 'bandwidth') reflects the hardware capability of buffering and, at the final level, of storing permanently the collected events in the unit time. Table 3.1 summarizes some of the assumed boundary conditions relative to two different scenarios at Run II. Once triggers are built for each

$\int \mathcal{L}dt$ regime	Medium	High
$\sqrt{s}$	2.0 TeV	2.0 TeV
$\mathcal{L}$	$1\times10^{32}cm^{-2}s^{-1}$	$2\times10^{32}cm^{-2}s^{-1}$
Number of bunches	36	108
Bunch-crossing time	396 ns	132 ns
Mean interactions per crossing	2.3	1.5
Level 1 bandwidth	40 KHz (400 μb)	40 KHz (200 μb)
Level 2 bandwidth	300 Hz (3.0 μb)	300 Hz (1.5 μb)
Level 3 bandwidth	75 Hz (750 nb)	75 Hz (375 nb)

Table 3.1: *Run II nominal boundary conditions [1].*

level, links across different levels are established by defining trigger paths. A trigger path identifies a unique combination of Level 1, Level 2 and Level 3 triggers.

Datasets (or data streams) are then formed by merging the data samples collected via different trigger paths. Hence, datasets are defined by a logic OR between trigger paths. This definition of datasets enables a monitoring of the cross section of individual triggers within the same trigger path in terms of luminosity variations and detector noise without loss of information, since for each event its 'trigger history' is recorded.

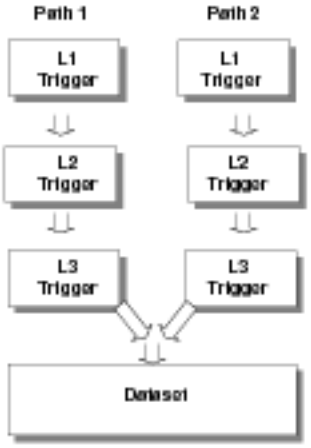

Figure 3.1: *Schematic diagram of trigger primitives, paths and datasets.*

A graphical representation of the trigger layout is depicted in fig. 3.1. In the following, a list of trigger primitives will be presented for each of the three trigger levels.

3.1.1 Level 1

Level 1 trigger primitives have been conceived on the basis of a very simple mechanism, aimed at minimizing the dead-time required for making a decision: finding simple physics objects and, at most, counting them. The nominal dead-time is $\sim$5.5 μs.

Primitives can be divided into four categories, according to the detector they are based on, and are completely hardware-based.

Calorimetry

Calorimetry primitives can be subdivided into two classes:

object primitives: energy deposits detected[1] in the central and plug calorimeter weighted by an appropriate $\sin\theta$ factor.

Within Level 1, towers are not considered individually, but merged in pairs along η. The primitives are addressed as 'trigger towers' and are $\Delta\eta \simeq 0.2 \times \Delta\phi = 15°$ wide[2]; the result is a 24×24 $\eta - \phi$ map of the calorimeter region extending to $|\eta| < 3.6$. Electromagnetic (EM) and total (EM+HAD) contributions are treated independently;

global primitives: transverse energy (EM+HAD) deposits recorded in all trigger towers above a threshold[3] are involved into two different sum procedure:

- ◇ all $\eta - \phi$ towers are summed together into the definition of ΣE_T;
- ◇ all 24 modules corresponding to each ϕ-wedge are added together and the $\Sigma E_{T_x} = \Sigma E_T(\phi)\cos\phi$, $\Sigma E_{T_y} = \Sigma E_T(\phi)\sin\phi$ sums computed

Correspondingly, object and global triggers can be defined. In both cases the trigger requires a comparison between a detected transverse energy (single trigger tower E_T and E_T^{had}/E_T^{em}, ΣE_T) and a threshold (EM and EM+HAD thresholds can be set independently). In the case of object triggers, the number of towers above threshold is counted. This is done by a 1-bit sum $(0, \geqslant 1)$ for single-object triggers and by a 2-bit sum $(0, 1, 2, \geqslant 3)$ for di-object triggers.

XFT

XFT is the acronym of eXtremely Fast Tracker and stands for a hardwired algorithm for track finding. A similar device (CFT, Central Fast Tracker) was in use during Run I for identifying high momentum charged tracks in the CTC (Central Tracking Chamber). For Run II, a new fast track finder has been designed for the COT. The guiding idea, on the other hand, remains the same: performing a fast $r - \phi$ track reconstruction and returning P_T, ϕ_0 (the azimuthal direction of the track at the point of minimum approach with respect to the beam axis) and the extrapolated position at the outer layer of the COT of the fitted track in case of success.

The XFT standards have been established in order to, at least, reach and possibly overcome the performances exhibited by the CFT. On this basis, the main design goals are[4]:

- ◇ track-finding efficiency greater than 96% for tracks with $P_T > 1.5\ GeV/c$;

[1] Although calorimeter responses are digitized into 10-bit words, allowing a precision of 125 MeV, at Level 1 only a precision of 250 MeV is available.

[2] Except for the highest $|\eta|$ towers, whose coverage is $\Delta\eta \simeq 1$.

[3] A 1 GeV threshold has been set on the basis of efficiency maximization studies computed on $W \to e\nu_e$ signal.

[4] The corresponding measured performances for CFT are reported in brackets for comparison.

- $\delta P_T/P_T^2 < 2\%\,(\,GeV/c\,)^{-1}$;
- double fake-rate rejection with respect to the CFT.

A good resolution on the fitted track ϕ_0 ($\delta\phi_0 \lesssim 8$ mrad) is required if the XFT output is to be used as a seed for the Silicon Vertex Tracker (SVT), a Level 2 trigger algorithm that will be described later in this chapter.

The XFT works on the basis of a two-step procedure. First, track segments are identified in each axial superlayer of the COT (here numbered between 1 and 4). A track segment is searched for by a pattern recognition algorithm among all possible hit patterns achievable by a track with $P_T \geqslant 1.5\ GeV/c$ in the 12 layers of sense wires of four adjacent COT cells. Track segments (*pixels*) – defined by their ϕ position at superlayer 3 and slope[5] – are then linked together into tracks. The starting point of the linking procedure is a valid pixel in superlayer 3, corresponding to a 1.25°-wide COT slice. Starting from this pixel, all combinations of track segments (*roads*) compatible with a $P_T \geqslant 1.5$ GeV/c -track hypothesis are computed through different superlayers. Among all roads found in each 1.25° COT slice, the one with the greatest number of associated pixels[6] and highest P_T is returned by the algorithm together with its charge, P_T and ϕ at superlayer 3.

Once the tracks have been found, their information is sent to the extrapolation unit (XTRP), whose task primarily consists in mapping the XFT tracks by means of lookup tables onto muon and electron primitives found by other Level 1 trigger processors. At the same time, for each track, the ϕ, P_T information is made available to Level 2 processors, such as SVT.

Furthermore, the XTRP can generate itself a Level 1 trigger accept, according to number of tracks, their topology and P_T threshold.

Muons

A Level 1 trigger muon object is obtained by matching a tracking primitive (*i.e.*, a XFT track) to a muon primitive.

The definition of muon primitive depends on the specific muon detector type: for scintillators (CSP, CSX), a muon primitive corresponds either to single-hits or to coincidences of hits. Differently, for wire chambers (CMU, CMP, CMX), a cluster of hits (*stub*) is searched for. In the case of CMU, CMX, a stub is defined whenever a coincidence, within a given time[7], is achieved between at least two hits collected in projective wires, *id est*, in wires belonging to different radial layers. For CMP, on the other hand, a pattern of hits in a tube stack consistent with a traversing track is required for stub definition. A further muon primitive is supplied by the hadron calorimeter, which is capable of signalling the passing of a minimum ionizing particle in each trigger tower.

Two major improvements distinguish the Run II from the Run I muon trigger:

[5] Slope is determined by the two outer superlayers only.

[6] The possibility of a three-out-of-four match is permitted for 'short tracks', which do not reach the outer superlayer; large $|\eta|$ tracks are included into this definition.

[7] The time interval is implicitly connected with a lower P_T bound, therefore P_T requirements for stubs are achieved by adjusting the time window in the stub definition.

- an increased coverage for CMP (+17%) and CMX (+50%) – see fig. 3.2 –, which results both in an augmented purity of the sample collected by combining CMU and CMP primitives and in an enhanced global acceptance;
- central tracking information from the XFT-XTRP will be available already at Level 1, providing a more effective fake-rate rejection;

As previously mentioned, XFT tracks and muon stubs information can be merged into muon objects by means of a matching between trigger primitives. These procedures consists of a $r-\phi$ track-stub match, which at Level 2 exploits only half of the full detector azimuthal granularity[8] ($\sim 1.25°$), and, eventually, of a P_T-based match, since independent thresholds can be set on the P_T of the track and of the stub[9]. In order to avoid a double-counting when considering dimuon objects, at least an empty $\Delta\phi = 2.5°$ segment is required between stubs.

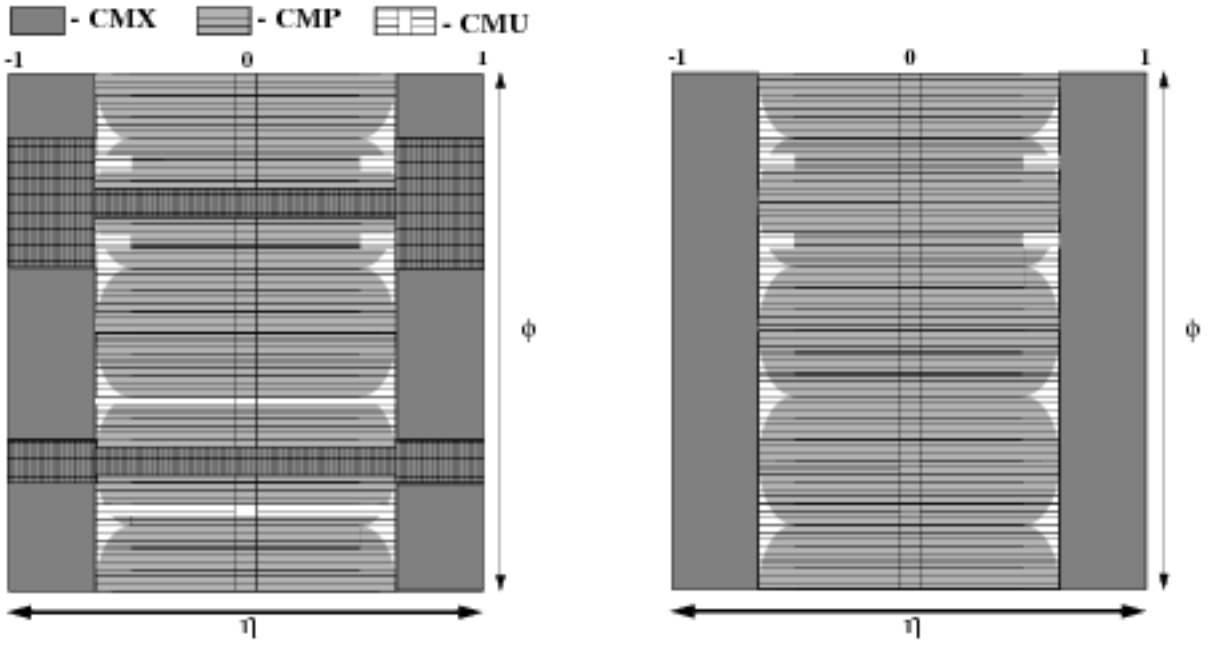

Figure 3.2: *Comparison between* CDF *central muon system* $\eta-\phi$ *map: Run I (left) and Run II (right) configurations.*

Electrons

Electron triggers are formed in the same way as for muons. In this case, however, the electron-oriented primitives achievable at Level 1 are essentially the calorimeter towers which have been described in detail on page 49. A Level 1 electron trigger can be

[8]The 2.5° azimuthal resolution of the Level 1 track-stub match in Run II is twice the exploited resolution in Run I, thanks to the improved performances of XFT with respect to CFT.

[9]However, it should be kept in mind that the precision on the P_T measurement achieved by the differential timing in the muon chambers is lower than the corresponding quantity measured by the XTRP.

obtained requiring a trigger tower with an electromagnetic energy content above a certain threshold to be matched to a XFT track fulfilling some P_T requirement. Rate constraints effectively influence the possibilities one can pursue in choosing thresholds: in particular, one can hope to lower the energy/momentum thresholds only by considering a two-electron topology in order to recover an acceptable trigger rate.

3.1.2 Level 2

Selection procedures at Level 2 become more sophisticated than at Level 1, in the sense that, while Level 1 is primarily devoted to rate reduction, at this point the less stringent time constraints ($\sim 20\,\mu$s) together with considerably lower rate, enable to concentrate on the true aim of a selection: the improvement of the signal to background ratio, a fundamental quantity for isolating a certain physical process.

If the core of the tools available at Level 2 is still given by hardwired requirements, a set of time-optimized software procedures can be integrated in the trigger system.

Calorimetry

One of the most common features of high energy hadron collisions final states is jets: they originate from the hadronization of energetic partons when, as a consequence of the Lorentz boost, the particles produced in such a process tend to be compressed into a narrow region of phase-space.

Since in general jets are not expected to be fully contained into a single trigger tower, the energy threshold for Level 1 jet trigger requirements has to be set at a considerably lower value than the typical jet energy in order not to loose efficiency. This, however, implies trigger rates which are too high to be fed directly into Level 3.

An effective rate reduction can be achieved at Level 2 by considering, instead of single trigger tower energies[10], the energy associated to clusters of contiguous trigger towers. The definition of clusters within an event requires an algorithm (*cluster finder*) whose working principle – essentially unchanged from Run I – can be explained in terms of four steps, a graphical representation of which can be found in fig. 3.3.

Step 1 Two energy thresholds must be fed to the cluster finder: the *seed* threshold will define which trigger towers have to be used as a starting point by the algorithm. The *shoulder* threshold, on the other hand, essentially establish the duration of a recursive procedure which will be described in the third step.

Step 2 All trigger towers with energy content above the seed threshold are identified and recorded as 'seed towers'. When all seed towers have been found, a second loop is performed on the remaining trigger towers in order to tag the 'shoulder towers', that is, the trigger towers whose energy exceeds the shoulder threshold.

Step 3 Iterative procedure starting from the seed tower that, among all seed towers with lowest η address (η_s), has the lowest ϕ address (ϕ_s): a signal is sent to the four $\eta = \eta_s \pm 1$ and $\phi = \phi_s \pm 1$ neighbouring trigger towers. If a signalled trigger tower is a shoulder tower[11], then, after being flagged as 'found', it signals in turn its three

[10] Here and in the following, the term 'energy' indicates the transverse component E_T.

[11] Note that seed towers fulfill also the shoulder condition, unless the shoulder threshold is higher than the seed threshold.

neighbouring trigger towers. The procedure is repeated until no more contiguous shoulder towers are found.

Step 4 Step 3 is repeated for all seed towers not being flagged as 'found' in previous iterations.

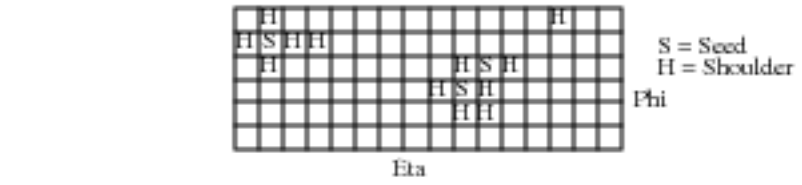

Step 1: seed and shoulder trigger tower tagging

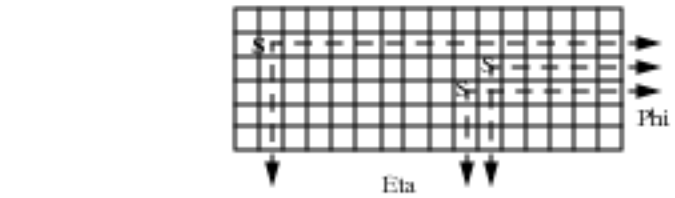

Step 2: seed and shoulder trigger tower eta-phi address recording

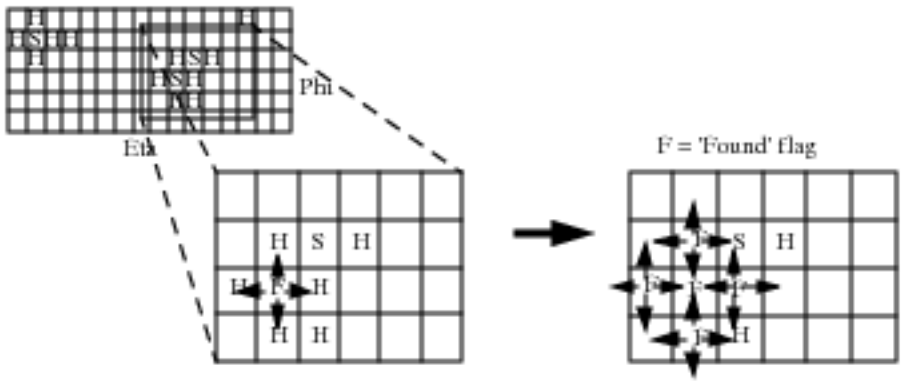

Step 3: contiguous shoulder towers are merged into clusters

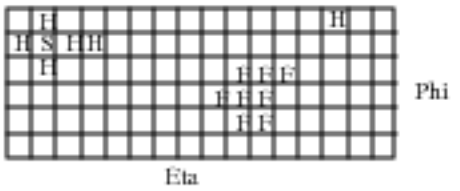

Step 4: trigger towers assigned to a cluster are excluded from further iterations

Figure 3.3: *Cluster finding procedure.*

When the procedure comes to an end, clusters are identified with the groups of contiguous trigger tower that have developed around a seed tower. Each cluster is assigned an energy equal to the sum of the energies[12] of all trigger towers belonging to the same group. The $\eta-\phi$ position of each cluster is then identified with the $\eta-\phi$ position of the seed tower which initiated the iterative procedure.

Within each event, the cluster finder procedure will be performed for each set of *seed, shoulder* thresholds (*pass*) that has been defined. in this way, within the same event, different topologies will be returned according to the typology of the clustering. The four passes that have been defined for Run II are:

- **type 1:** $E_T^{em}(seed)=3.0$ GeV , $E_T^{em}(shoulder)=1.0$ GeV and $E_T^{had}(seed,shoulder)=\infty$ for low-P_T electron/photon;
- **type 2:** $E_T^{em}(seed)=8.0$ GeV , $E_T^{em}(shoulder)=7.5$ GeV and $E_T^{had}(seed,shoulder)=\infty$ for high-P_T electron/photon;
- **type 3:** $E_T(seed)=3.0$ GeV , $E_T(shoulder)=1.0$ GeV (both hadronic and electromagnetic components) for *jet* clustering;
- **type 4:** $E_T^{em}(seed)=2.0$ GeV , $E_T^{em}(shoulder)=\infty$ and $E_T^{had}(seed,shoulder)=\infty$ for low-P_T electron in B-physics.

In the case of type 4 clusters, the choice of an infinite electromagnetic shoulder threshold corresponds essentially to an implicit isolation requirement, since this procedure will lead to single trigger tower clusters. Isolation patterns can be explicitly required during clustering by asking the smallest of the sums depicted in fig. 3.4 to be less than a given threshold. However, for low-P_T electrons, produced for instance in the semileptonic decays of B or C-hadrons, a type 4 clustering is preferred, since, assuming the identified cluster correctly tags the tower struck by the electron, any further tower contribution to the energy would dilute the information deposited in the calorimeter by the electron.

Figure 3.4: *Tower isolation patterns.*

Exactly as for Level 1, Level 2 calorimetry primitives can be grouped into two categories:

object primitives: energy depositions[13] associated to hadronic (type 3) or electromagnetic (type 1, 2 and 4) clusters. Besides energy content and type, the information concerning the position of cluster($\eta-\phi$ address of seed towers) is stored, in order to enable combinations between calorimetric and tracking (XFT) primitives;

global primitives: the number of clusters, according to cluster type and energy, is available at Level 2. Global energy sums are cluster-based, *i.e.* they are obtained by summing the contributions of all clusters in an event. The total energy, ΣE_T, is performed over all type 3 clusters, while other ΣE_T observables can be defined considering different clusters subsets (for instance, on can compute the sum over

[12] Electromagnetic and total contributions separately.

[13] At Level 2, the full calorimeter resolution of 125 MeV is exploited.

all type 3 clusters with E_T greater than a given minimum threshold). Global non clusterized energies, on the other hand, are available at Level 1 only.

SVT

The study of B-physics, that is processes involving b quarks, is of crucial importance at hadron colliders. On one hand, this kind of physics allows precision measurements on the Yukawa section of the Standard Model – related to the Cabibbo-Kobayashi-Maskawa matrix and *CP* violation phenomena – by exploiting channels like $B_d^0 \to J/\psi + K_S$, $B^0 \to \pi^+\pi^-$, $B_s \to \rho + K_S$. On the other hand, a high-P_T b enhanced statistics translates into an improved knowledge on dijet mass resolution (for instance from $Z^0 \to b\bar{b}$), therefore enabling more control of energy-scale systematics. These studies are crucial for improvements in top physics measurements and searches for new phenomena ($H^0 \to b\bar{b}$).

Already during Run I CDF, being equipped with a vertex detector, was capable of performing such studies, which essentially rely on reconstructing secondary vertices which are produced as a consequence of the remarkable B-hadrons decay length ($\sim 500\,\mu$m). However, this capability was confined to the offline analysis, while the tagging of the interesting events was left to leptonic triggers. For this reason, the global efficiency on B-physics was drastically reduced, while some specific processes – like, for instance, $B^0 \to \pi^+\pi^-$, important for *CP*-violations measurements – were virtually undetectable.

During Run II, this lack will be filled by the introduction of the SVT (Silicon Vertex Tracker [2]), a device for tagging displaced tracks already at trigger level. As previously mentioned, in fact, displaced tracks (*i.e.* with large impact parameter) can be interpreted as signals of the existence of secondary decay vertices of heavy-flavoured objects. This tool provides a response by merging the information supplied by the new silicon vertex detector (SVXII) with the output of the Level 1 fast tracker (XFT, see pag. 49) in time for the Level 2 decision. In this way, the SVT will allow the collection of fully hadronic decay modes of B-hadrons as well as an efficiency enhancement for the semileptonic channels by enabling a lower P_T threshold for lepton tagging.

The working strategy of SVT is summarized in fig. 3.5. First, SVXII channels, grouped into 24 ϕ sectors (each one of the 12 azimuthal wedges is divided in two sectors according to the sign of z), are read out by 72 *Hit Finders*, which perform pedestal and bad-channel subtraction. Once strip readout is completed, the *Hit Finders* search for hit clusters on each layer contained in the corresponding sectors, computing the centroid of each admissible cluster. Centroids represent the most likely intersection points between the trajectory of a track with each of the five[14] radial silicon layers of SVXII

Silicon clusters information is then transmitted to the *Associative Memory Sequencer* (AMS), which, at the same time, is fed with the XTRP output. In the AMS, a first, tentative association

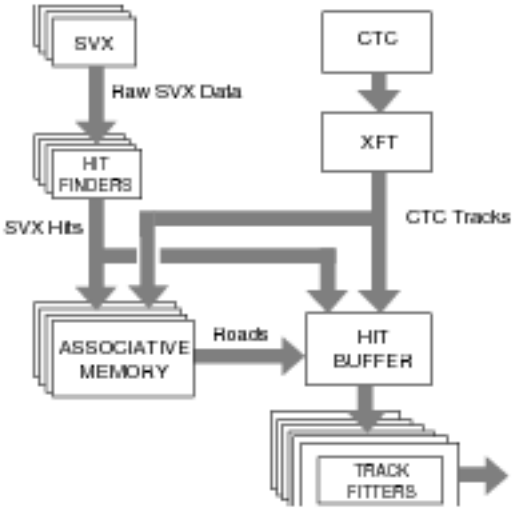

Figure 3.5: *The* SVT *data flow.*

[14] Only four are used by SVT.

between clusters and XFT tracks takes place: this is done by lining up the clusters of a given ϕ sector with outer XFT tracks. Due to the large number of possible combinations arising from this procedure, each cluster is substituted by a *superstrip*, whose dimension (250 μm) represents the best compromise between fake tracks rejection and cost. Then, the association between stacks of *superstrips* and XFT tracks is performed: each admissible combination, evaluated on the basis of lookup tables, defines a *road*, which represents a broad track.
Roads, each corresponding to a set of four SVXII clusters and an outer XFT track, are then sent to the *Hit Buffers*, which retrieve the full detector information (*i.e.* the single hits coordinates for each SVXII cluster and the two XFT track parameters[15]) to be used to fit the track to an arc of circumference trajectory and obtain the three parameters P_T, ϕ and d (impact parameter).

Simulations of the SVT trigger show that the resolutions $\sigma_d \simeq 35\,\mu$m (for $P_T > 2\ GeV/c$), $\sigma_\phi \simeq 1$ mrad and $\sigma_{P_T} \simeq 0.3\% \cdot P_T^2$ (with $[P_T] =$ GeV) are at reach. As an example of the rejecting power of the algorithm, one can consider the case of the B-decay $B^0 \to \pi^+\pi^-$, where the requirement of two XFT tracks ($P_T(1) > 2\ GeV/c$ and $P_T(2) > 3\ GeV/c$) well separated ($35° < \delta\phi < 135°$) fulfilling an additional request on the impact parameter ($|d| > 100\,\mu$m) at Level 2 reduces the rate by a factor 10^3, whilst maintaining an efficiency of $\sim$50% on the signal.

Two potential problems need to be controlled in order for the SVT trigger to meet design specifications. The first concerns mechanical alignment of the SVXII detector, which has to be collinearly aligned with the beam axis within 100 mrad in order to keep into account the fact that SVT does not have z information. The second problem, related to the occupancy of SVXII, is directly connected to the event multiplicity. It may happen, in fact, that high luminosity scenarios, where too many tracks are fed into SVT, could cause timing problems in the SVT trigger. The control of this kind of problem needs tuning of the SVT machinery on real data.

Muons

A minor difference distinguishes Level 2 from Level 1 muon primitives. This difference is essentially related to the precision of the ϕ-matching between XFT tracks and stubs. At Level 2, in fact, full detector resolution is exploited and the matching is performed within 1.25° for CMU and CMX, while for CMP the track segment to be matched to the XFT track has to be reconstructed within one-tube stack, which corresponds to an azimuthal coverage of 1.25° at the closest radial distance from the beam axis, reducing to 0.6° towards the edges of the chamber.

Electrons

At Level 2, central and plug shower maximum (XCES and XPES) primitives are available for triggering on electrons and photons. The shower maximum detectors rely on the strip/wire chambers (CES) contained in the central electromagnetic calorimeter towers and on two-layers of scintillator strips (PES) located within the electromagnetic plug calorimeters.

[15]Namely, the signed curvature and the ϕ seed (*i.e.* the azimuthal coordinate of the track at axial superlayer 3 of the COT – see page 50).

Both detectors provide a measurement of the charge deposition as well as a determination of the position of the intersection point of the track trajectory at the detector surface. This is achieved by merging the information collected by strip pads and wires in the central region or by U and V plug scintillators strips.

The purpose of these detectors is two-fold: first, providing a rate-rejection handle against non-electromagnetic matter and, second, enabling a separation between electrons and photons.

3.2 Physics Objects

As shown in the previous sections, physics objects are of fundamental importance for selecting a signal from the bulk of background events produced in hadronic collisions. However, it was pointed out that at trigger level, especially at Level 1 and 2, the full detector resolutions are seldom exploited completely due to time constraints. The third level of the trigger supplies a further step towards refining selection tools, which has the two-fold implication of augmenting the selection purity and of lowering the event rate to a level compatible with storing procedures.

3.2.1 Level 3

At Level 3, a more sophisticated event reconstruction is performed. This implies the definition of a new class of physics objects, including three-dimensional tracks, jets and identified leptons, which will be discussed in the following.

Some variables, as well as quantities that need a long processing (like, for instance, global kinematical event observables, or track isolation properties), cannot be calculated within the allowed time slot at trigger level. Further offline processing is then performed on selected events.

3.2.2 Tracks

Tracks carrying an electric charge qe (where e is the positron charge) travelling with a velocity $\boldsymbol{v}$ in a homogeneous magnetic field $\boldsymbol{B}$ experience a Lorentz force:

$$\boldsymbol{F} = qe\boldsymbol{v} \wedge \boldsymbol{B}$$

that constrains the tracks to a helicoidal trajectory, whose radius ρ, measured in the plane transverse to $\boldsymbol{B}$, is directly related to the track transverse momentum P_T according to the relation:

$$\rho = \frac{P_T}{|q|eB} \ .$$

A track trajectory is completely defined by five parameters [3]:

- $\cot\theta$: cotangent of polar angle of the helix measured at minimum approach to beam axis;
- C: signed half curvature (same sign of q);
- z_0: z-coordinate of minimum approach to beam axis;
- d: impact parameter;
- φ_0: azimuthal angle of the helix at minimum approach to beam axis.

Reconstruction

Some problems affected the tracking efficiency during Run I. These can be briefly summarized as follows:

- the length of SVX ($\sim 50\,\text{cm}$) was covering only part of the $p\bar{p}$ interaction region[16]. Consequently, only $\sim 60\%$ of the events fell into the vertex detector acceptance;
- the four layers of silicon in SVX, with a $\sim 95\%$ hit efficiency, yielded a global tracking efficiency of $\sim 75\%$ in four-out-of-four hit assignment for tracks within detector acceptance. Furthermore, the short lever arm ($\sim 5\,\text{cm}$) induced a poor P_T resolution;
- the silicon layers in SVX were single-sided, thus providing $r-\phi$ information only;
- three-dimensional tracking efficiency was further degraded by limited stereo sampling in the CTC.

The track-finding procedure used during Run I was based on linking SVX hits to previously fitted tracks in the CTC. This method, although improving the resolution achievable on the track parameters, did not allow any recovery from outer tracking inefficiencies.

The tracking system for Run II has then been thought in order to fit a higher luminosity scenario and, at the same time, to correct the limitations observed during Run I. For this purpose, the CTC and the SVX have been substituted by the COT and a new silicon complex respectively.
The adoption of the COT, a tracking chamber which addresses the increased luminosity and reduced bunch spacing by adopting smaller drift cells, provides a faster response and double stereo sampling with respect to Run I configuration.
Inner tracking (*i.e.* for $r < 48\,\text{cm}$) is entrusted to a silicon multilayer complex, which includes LAYER00, SVXII and ISL. The combination of these devices results in up to eight points for each fiducial track and guarantees a coverage of almost all the $p\bar{p}$ interaction region. Position measurements[17], ranging from ~ 1.6 to $\sim 28\,\text{cm}$, supply a long lever arm providing a P_T measurement with a precision of $\delta P_T/P_T^2 \sim 0.4\%$ in the silicon system alone.

The potentialities of this architecture can be fully exploited by means of a tracking procedure, which integrates the information supplied by various detectors. Several options are being investigated: besides the stand-alone COT reconstruction and tracking in the silicon system seeded from COT tracks (inherited from Run I), stand-alone silicon reconstruction and outward extension of silicon tracks in the COT will be possible. The latter options allow tracking to be extended in the region $1 < |\eta| < 2$.

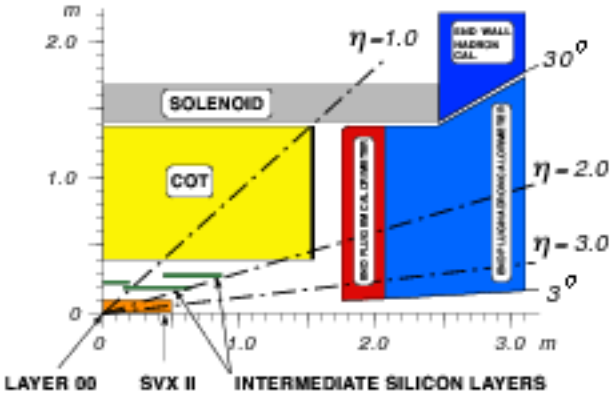

Figure 3.6: $r-z$ *view of* CDF.

[16] The z coordinate of $p\bar{p}$ interactions is approximately Gaussian-distributed with $\sigma \simeq 30\,\text{cm}$.
[17] All layers except the innermost provide both $r-\phi$ and $r-z$ information

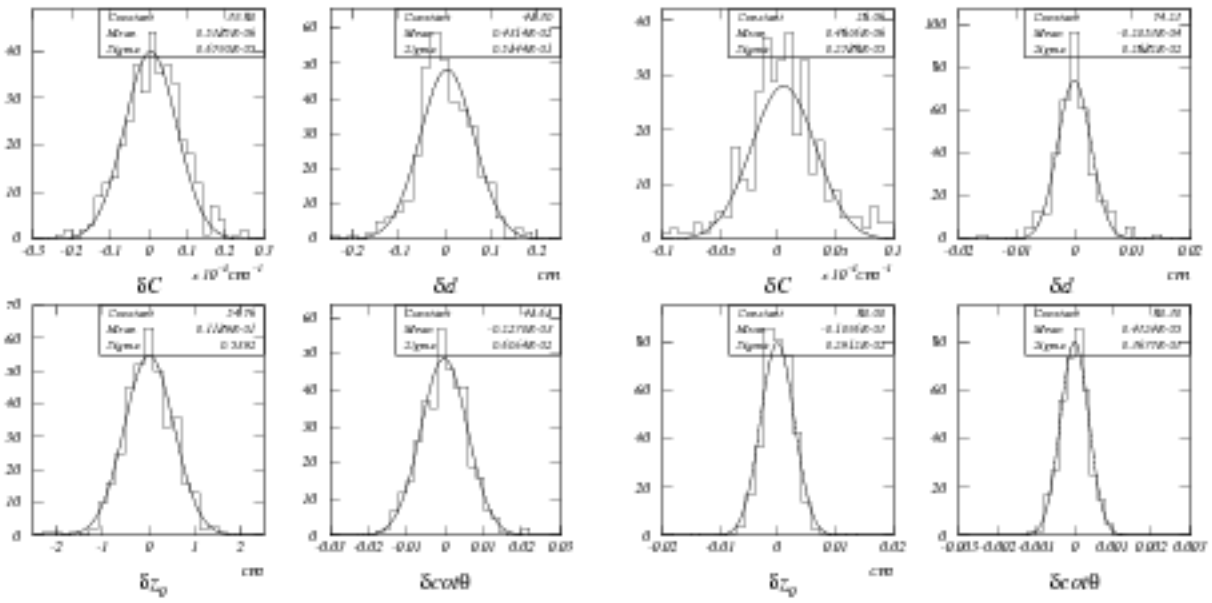

Figure 3.7: *A comparison between expected resolutions on tracking parameters achievable in stand-alone* COT *(left) and integrated tracking (right) environments [4].*

Resolutions

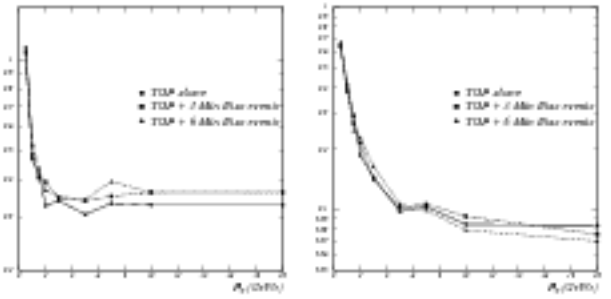

Figure 3.8: *A comparison between expected P_T resolutions for stand-alone* COT *(left) and integrated tracking (right) [4].*

To study the performances of the CDF II tracking system, the dense environment of b-jets in $t\bar{t}$ events have been used. As previously mentioned, if on one hand the design of the new tracking detectors has been developed aiming to achieve optimal performances even in a higher luminosity scenario, on the other, this led to the introduction of more material around the interaction point (more silicon layers and COT stereo superlayers). Simulations have then been focussed on estimating the effects that luminosity changes and multiple scattering phenomena induce on the resolution of the tracking parameters. The effect of multiple interactions (whose average number per beam crossing depends on both the instantaneous luminosity and number of colliding bunches) is kept into account by mixing one $t\bar{t}$ event with a variable number of generated minimum bias events[18] (see fig. 3.7).

Resolution estimates have been obtained as the difference between the reconstructed track parameters and the corresponding generated quantities which have been supplied as input to the tracking simulator. Results are shown in figs. 3.7 and 3.8. Although fig. 3.8 refers to a low luminosity scenario, degradations due to multiple interactions (which have been treated as described above) show a weak dependence on $\mathcal{L}$, of the order of 10% for $\mathcal{L}$ spanning from $1(3)\times10^{32}\ cm^{-2}s^{-1}$ to $2(6)\times10^{32}\ cm^{-2}s^{-1}$ in correspondence of 36(108) Tevatron bunches.

[18] An auto-accepting trigger path is used for collecting of unbiased events for calibration purposes.

Both figs. 3.7 and 3.8 show a comparison of the tracking resolutions achievable by the COT running in a stand-alone mode and by the integration of all tracking devices. This allows to appreciate the contribution of the silicon vertex detector, whose effect – related to the increased number of layer and of their shorter distance from the beam axis – is crucial for pursuing high precision measurements in particular on d and z_0. The effect of augmenting the number of silicon layers and of their arm lever, on the other hand, implies an enhanced resolution on P_T as well. A summary of the resolutions achievable in Run II by CDF is reported in table 3.2.

Resolution		
	COT	COT+SVXII+ISL
$\delta P_T/P_T^2\,[(\mathrm{GeV}/c)^{-1}]$	3×10^{-3}	1×10^{-3}
$\delta d\,[\mu\mathrm{m}]$	600	30
$\delta z_0\,[\mu\mathrm{m}]$	5×10^{3}	30
$\delta\cot\theta$	6×10^{-3}	4×10^{-4}

Table 3.2: *Summary of expected resolutions on various track parameters in Run II.*

In Run I, with an instantaneous luminosity $\sim10^{31}\ cm^{-2}s^{-1}$, the CTC could provide a momentum resolution $\delta P_T/P_T^2\simeq0.2\%(GeV/c\ )^{-1}$ as a stand-alone tracker and $\delta P_T/P_T^2\simeq0.1\%(\ GeV/c\ )^{-1}$ in combination with SVX or by using beam-constrained tracks. The use of SVX, on the other hand, implied a consistent increase in impact parameter resolution, passing from $\sim340\,\mu$m (stand-alone CTC) to $\sim15\,\mu$m.

The determination of the absolute momentum scale can be obtained by means of a comparison between a clean and known signal to some reference. In the case of CDF the decay $J/\psi\to\mu^+\mu^-$ is studied.

3.2.3 Primary vertex reconstruction

Reconstructed tracks enable the computation of the primary vertex in each event: its z position is then used in defining the actual pseudorapidity of each physics object reconstructed in the event, while its transverse position is important since it provides the benchmark for secondary vertex-finding procedures. The $p\bar{p}$ luminous region has a Gaussian spread of about $35\,\mu$m in the transverse plane. Its location is known with good precision, but a more precise determination can be obtained with the track parameters. Instead of relying on the beam spot location, an algorithm can be run on all reconstructed tracks according to an iterative scheme used during Run I (VXPRIM [5]): a P_T-weighted fit is performed with the tracks in the xy plane. Tracks with large impact parameter with respect to the fit vertex are discarded, and the fit is repeated until stability is reached. The resulting resolution in the x and y coordinates of the primary vertex ranges from 6 to 26 μm, depending on the topology of the event and on the number of tracks used in the fit. This determination of the primary vertex represents a significant improvement over the beam spot information alone, and is more reliable on an event-by-event basis.

3.2.4 Jets

Isolated partons emerging from the initial $p\bar{p}$ collision, due to their nature of strongly interacting matter, undergo a process called fragmentation. During fragmentation, a parton shower is developed from the original parton as an effect of the increasing strong coupling constant as lower P_T regimes are reached. Fragmentation terminates with hadronization, a process where all partons recombine in colour singlet states, corresponding to on shell hadrons. By momentum conservation, the more energetic the initial parton is, the closer the resulting hadrons are confined in phase-space. These clusters of particles are called jets and their importance is related to the fact that they represent the only physically-measurable quantity carrying a reminescence of the initial parton.

Jet Clustering

The information provided by the cluster finder algorithm at trigger level can be considered as a first-order jet reconstruction. At Level 3, looser time constraints enables to exploit the full detector segmentation for a better jet energy and direction determination.

At CDF a cone algorithm is used for jet reconstruction. The opening angle of the cone is usually defined in terms of a radius in the $\eta-\phi$ plane. Due to the relativistic properties of pseudorapidity, in fact, this definition allows to conveniently identify jets by circular disks on the $\eta-\phi$ calorimetry map. The magnitude of the radius (R) has to be chosen accordingly with the characteristics of the physical process under study: hence, lower radii (typically 0.4) will be preferred in high multiplicity events, where a higher jet resolution is required.

The first step for jet clustering consists in assigning to each calorimeter tower ($\Delta\eta\simeq 0.1$, $\Delta\phi\simeq 15^{\circ}$) a $r\eta\phi$ vector, with r representing the transverse energy deposition and η, ϕ addressing the corresponding energy barycenter[19].

Preclustering. Vectors with $E_T > 1$ GeV are ranked according to a decreasing magnitude order; the vector list is then scanned downwards in the following way:

1. a circle of radius R is drawn around the first element of the list;
2. all vectors falling inside the circle are summed to it and removed from the list;
3. a new circle is drawn around the next vector in the list;
4. steps 2 and 3 are repeated recursively until the end of the list is reached.

Clustering. A second iterative procedure involving all vectors with $E_T > 0.1$ GeV is started:

5. the E_T associated to each circle is recomputed by merging all the enclosed vectors;
6. new circles are drawn around the so obtained resultants;
7. steps 5 and 6 are reiterated until a stable configuration[20] is reached.

[19] The barycenter of the energy is defined assuming that all electromagnetic and hadronic energies have been released at a depth of 6 radiation lengths (X_0) and 10 interaction lengths (λ) respectively.

[20] A stable configuration is achieved when circles are reconstructed in the same position for two consecutive iterations; usually this happens after three iterations.

It may happen that two circles overlap. In this case, if the total contribution of all vectors belonging to the intersection region does not exceed the 75% of the magnitude of the smaller of the two resultants, each vector is assigned to the closest resultant. Otherwise, the two circles are replaced by a single one, centered around the sum of their resultants.

The circles that remain at the end of the procedure are identified with jets if their energy is large enough (typically 10 or 15 GeV) to guarantee their unambiguous interpretation in terms of partons.

3.2.5 Leptons

Lepton detection and tagging is a crucial feature at hadron colliders, where their presence provide a powerful handle to access electroweak processes. According to their production mode, leptons can be broadly divided into two classes: prompt high-P_T leptons, mainly coming from vector boson decay ($Z^0 \to \ell^+\ell^-$ and $W^\pm \to \ell^\pm\nu_\ell$), and non-isolated leptons. The latter, referring to leptons embedded within a jet, are usually characterized by a softer P_T-spectrum and – in case a correct identification is provided – can be safely related to the semileptonic decay of charmed or bottom hadrons. In fact, decaying bottom or charmed hadrons are expected to emit an electron or a muon[21] in approximately 20% of the cases. Furthermore, bottom hadrons decay in charmed hadrons[22], whose downstream decays can yield leptons.

Electrons

Electron tagging at CDF essentially relies on energy depositions in the electromagnetic towers of the calorimeter. Identification procedures, however, depend on both the transverse energy and the rapidity of the candidate. For electrons produced in the semileptonic decay of bottom and charmed hadrons, being characterized by a softer P_T spectrum with respect to prompt electrons, a reconstructed track extrapolating to an electromagnetic deposit and consistent with E/P electron hypothesis is needed to reduce the background from photons. Therefore, electron identification is limited within the acceptance of the tracking system. During Run I, soft electron tagging was then performed within $|\eta| < 1$. In Run II one hopes to fully exploit the new tracking capabilities as well as the performances of the new plug calorimeter.

The possibility of a non-electron track faking an E/P requirement because of the contribution of surrounding soft particles releasing energy in the same calorimeter towers is still high. A further contribution may also comes from isolated hadrons performing early showering (*i.e.*, before reaching the hadronic section of the calorimeter). Two sets of requirements help in keeping these effects under control. The first one relies on two purely calorimetric variables:

- $\diamond$ E_{had}/E_{em}: an upper bound on this variable can essentially result in an upper bound on the hadronic energy deposition detected within a jet cone. According to the process that led to the electron, the ratio E_{had}/E_{em} can be computed on cluster topologies other than jets, such as single towers or 3×3-tower squares.

[21] Taus, although produced with almost equal frequency than electrons and muons, due to their problematic detection, do not give a significant contribution to B physics at CDF.

[22] Since $|V_{cb}|^2 \sim 200\text{-}|V_{ub}|^2$.

- L_{shr}, the lateral shower shape χ^2, is a χ-squared comparison of the observed calorimeter lateral shower profile to test-beam electrons.

The second set, on the other hand, exploits the information provided by the CES detector. The latter proves to be of crucial importance for tagging non isolated electrons, due to its finer granularity with respect to the calorimeter towers. A predetermined number (typically 3, 5, 7, 9 or 11) of contiguous strips (or wires) is clustered around a seed, whose rôle can be played by a strip/wire either detecting an energy larger than 0.5 GeV or intercepted by the trajectory of a reconstructed track. Three kinds of information are accessible after clustering:

pulse-height: the energy content of a cluster reconstructed either in the strip or in the wire plane (E_s, E_w);

position: the centroids of the clusters reconstructed in the strip and wire planes provide a $x-z$ reading in the local wedge-coordinate system (see fig. 2.9). This information is useful for providing a high quality track-cluster matching;

shape: two χ-squared comparisons (χ^2_{strip}, χ^2_{wire}) of CES cluster profile fits (in strip and wire planes respectively) to test beam electrons.

Cluster-based procedures for electron tagging, like the standard electron selection described in table 3.3, however, contain several implicit isolation requirements that makes them rather inefficient in case the soft electron is embedded in a jet, which is the most likely situation expected in b and c quark decays. Clustering procedures, in fact, tend to average energy contributions coming from adjacent towers, making a few-GeV signal very difficult to distinguish from the large backgrounds provided by photons and low-energy hadrons releasing most of their energy in the electromagnetic calorimeter.
For this reason, during Run I a track-based soft electron tagging procedure[23] has been studied [6] and applied in offline analyses involving b-jet identification, for instance in top searches [7]. Instead of beginning from an electromagnetic deposition in the calorimeter, the algorithm starts by extrapolating all tracks passing a standard set of loose quality criteria to the central electromagnetic calorimeter (CEM) and to the muon chambers. Then, if the track extrapolates to a fiducial region of the detector, it is flagged as a 'candidate' track. In the following, candidate tracks undergo a selection criteria – whose main requirements are reported in table 3.3 – optimized for tagging electrons coming from b quark decay.
The soft electron tagger is characterized by a fake rate of $\lesssim 0.4\%$ per track, at the same time retaining an average efficiency of $\sim 70\%$ on single electron tracks [8].

[23] The soft electron track-based procedure is a part of a more general algorithm, dedicated to soft lepton tagging (often indicated as SLT).

[24] The standard electron tagging procedure is cluster-based: all calorimetric quantities refer to reconstructed jets unless explicitly remarked.

[25] The soft electron tagger relies on a track-based procedure: single tower quantity are used when calorimetric variables are computed. The tower is determined by extrapolating the candidate electron track to the electromagnetic calorimeter.

[26] In a 3×3-tower square centered in the electron jet seed.

[27] E_{s_5}, E_{w_5} are five-strip/wire cluster energies.

[28] Δx and Δz describing the spatial mismatch between track extrapolation at CES and cluster centroid.

Variable	Std. electron cuts[24]	Soft electron cuts[25]
$(E_T)_{em}$	>7.5 GeV	–
P_T	>6 GeV/c	$\geqslant 2$ GeV/c
E_{em}/P	–	$\geqslant 0.7, \leqslant 1.5$
E_{had}/E_{em}	<0.04 [26]	<0.1
L_{shr}	<0.2	–
E_{s_Σ}/P, E_{w_Σ}/P [27]	–	$\geqslant \min\{0.6, 0.24+0.03P\}$ GeV
$\lvert\Delta x\rvert$ [28]	<1.5 cm	$\leqslant \max\{0.7, 1.82-0.1867P\}$ cm
$\lvert\Delta z\rvert$ [28]	<3 cm	$\leqslant 2$ cm
$\chi^2_{strip}/6$	<10	$\leqslant 16$
$\chi^2_{wire}/6$	<10	$\leqslant 16$
Q_{CPR}	–	$\geqslant 4744-11592(P/P_T)+7923(P/P_T)^2$
Q_{CTC}	–	$\geqslant 29.15+e^{1.671-0.08P}$, $P\leqslant 15$ GeV/c

Table 3.3: *Standard electron selection compared to soft electron requirements (P, P_T expressed in GeV/c) for Run I. Further explanation is provided in the text.*

In order to achieve these goals, the soft electron algorithm exploits two more track-dependent pieces of information supplied by the detector: the energy deposition in the central preradiator (CPR) and the specific energy loss ($\mathrm{d}E/\mathrm{d}x$) experienced by the candidate track in traversing the central tracking chamber.
The CPR energy (Q_{CPR}) is computed in a similar way to CES: a three-wire sum is performed around the point the track extrapolates to. Since larger track η values correspond to thicker layers of material travelled by the particle, larger charge depositions in the CPR are expected for increasing η. Exploiting this fact, a rough z matching can be obtained between the CPR deposition and the track by introducing a $P/P_T = 1/\sin\theta$ dependence in the CPR pulse-height requirement.
Within the range of interest, $\mathrm{d}E/\mathrm{d}x$ is essentially independent from momentum if electrons are considered. Conversely, a strong momentum dependence is exhibited by other particles, like muons and light charged hadrons, which can contaminate the electron sample. The specific energy loss (Q_{ctc}) is required to match the expected electron behaviour for $P\leqslant 15$ GeV/c.

A serious source of background for either cluster-based or track-based procedure is due to photons arising from the decay of neutral pions, copiously produced within jets, which tend to convert into electron-positron pairs in detector material. The P_T spectrum of these electrons is not very different from that of electrons produced in b and c quark decays. This can be achieved by means of an algorithm that, after reconstructing all possible conversion pairs within an event, discards any electron candidate that can be associated to one leg of a conversion pair. In order to tag conversion pairs, the algorithm performs a first selection on the basis of geometrical considerations: two variables, $\Delta\cot\theta$ and $\Delta S = D-\rho_1-\rho_2$, where D is the distance between the center of the two circular trajectories – of radii ρ_1 and ρ_2 – describing the tracks in the $r-\phi$ plane, are used to select tracks compatible with coming from a common vertex[29], constrained to lay within 50 cm from the beamline (where the highest concentration of material in the tracking volume is found). Then, the two tracks fulfilling this requirement must converge to an invariant

[29] Actual requirements on these variables are $|\Delta\cot\theta|<0.06$ and $\Delta S<0.3$ cm.

Variable	Soft muon cuts			
	CMUP[31]	CMU	CMP	CMX
P_T	$\geqslant 3$ GeV/c	$\geqslant 2$ GeV/c	$\geqslant 3$ GeV/c	$\geqslant 2$ GeV/c
$\lvert\Delta z\rvert$	$< \max\{3\sigma, 8\,\text{cm}\}$	$< \max\{3\sigma, 8\,\text{cm}\}$	–	–
$\lvert\Delta x\rvert$	$< \max\{3\sigma, 2\,\text{cm}\}$	$< \max\{3\sigma, 2\,\text{cm}\}$	$< \max\{3\sigma, 5\,\text{cm}\}$	–
$\lvert\Delta\phi\rvert$	–	–	< 0.1 rad	< 0.1 rad
$\chi^2_{\Delta\phi\Delta x}$	–	< 10 [32]	< 10 [33]	< 9 [34]
$\chi^2_{\Delta x}$	–	–	–	< 9
$\chi^2_{\Delta z}$	–	–	–	< 9
$E_{had} - \Sigma_p^{0.2}$ [35]	< 6 GeV	< 6 GeV	< 6 GeV	–

Table 3.4: *Soft muon requirements for Run I; further explanation is provided in the text.*

mass lower than 0.5 GeV/c^2 to be tagged as a conversion pair.

Muons

Tagging in the case of muons is much less problematic than for electrons, since the natural tendency of muons to penetrate thick layers of materials can be exploited in order to separate them from surrounding electromagnetic and hadronic matter. For this purpose, the shielding offered by the calorimeters is used, while detection of charged particles beyond them is achieved by means of the muon system. The usual method for tagging muons consists in extrapolating a track to the muon system and matching it to a stub reconstructed therein.

The soft muon algorithm differs from a standard selection essentially because a lower P_T threshold implies taking into account the effect of multiple scattering, which becomes more relevant the lower P_T the particle has. After extrapolation, the distances from the edges of each detector as well as the average multiple scattering distance (σ_{MS}) are computed for each track. These parameters are used to assign tracks to four different fiducial regions of the muon system[30]: CMUP for tracks traversing both CMU and CMP volumes, CMU/CMP for tracks passing through the CMU/CMP volume only, while escaping the coverage of CMP/CMU, and CMX for tracks falling in the CMX fiducial volume. Each track falling in one of these classes is then matched to a muon stub; matching requirements depend on the class the track belongs to, as described in table 3.4. From the expected mismatch, χ^2 variables are built for each matching quantity: Δx refers to the distance between the extrapolated track and the stub in the transverse plane computed at the inner radius of the muon detector, while Δz refers to the mismatch in the z direction. In particular, the variable $\chi^2_{\Delta\phi\Delta x}$ takes into account the correlation between Δx and $\Delta\phi$, the latter describing the mismatch between the track extrapolated direction and the stub slope.

The major source of contamination in the case of muons arises from calorimeter *punchthroughs* (secondary charged pions leakages through the outermost layer of the hadron calorimeter) and from muons produced in the decays in flight of kaons or pions, which are responsible of 'fake' stubs. The former is strongly limited by the coincidence of CMU and CMP in the CMUP category. Furthermore, since punchthroughs are characterized by

[30] The value of $\sigma = \sqrt{\sigma^2_{SM} + \sigma^2_{res}}$, with σ_{res} describing the resolution of the detector, will be used as an estimate of the Gaussian fluctuation affecting the extrapolated position of the track in the muon system.

a higher activity in the muon chambers (especially in the CMU), an upper limit on the number of tubes involved in the stub definition (typically 5) is applied.

[31] Matching requirements for CMUP tracks refer to stubs in CMU only; the presence of a stub in CMP is enough to reduce background from punch-throughs.

[32] The $\chi^2_{\Delta\phi\Delta x}$ (CMU) replaces the straight Δx requirement for $P_T < 20$ GeV/c.

[33] The $\chi^2_{\Delta\phi\Delta x}$ (CMP) replaces the Δx, $\Delta\phi$ requirements for $P_T < 10$ GeV/c.

[34] The $\chi^2_{\Delta\phi\Delta x}$ (CMX) replaces the $\Delta\phi$ requirement for $P_T \leqslant 5$ GeV/c.

[35] The variable $\Sigma_p^{0.2}$ is defined as the sum of the momenta of all tracks reconstructed within a cone of $R = 0.2$ around the candidate muon. This cut, applied to tracks with $P_T > 6$ GeV/c only, is aimed at increasing muon purity; above this value, muons – which are minimum ionizing particles – deposit smaller energies in the calorimeters than hadrons.

Bibliography

[1] M. Albrow *et al.*, (The CDF Trigger and Datasets Working Group), *"Run II Trigger Table and Datasets Plan"*, CDF internal note 4718, Sep 2000.

[2] S. Belforte *et al.*, *"SVT – Silicon Vertex Tracker – Technical Design Report"*, CDF internal note 3108, Oct 1996.

[3] H. Wenzel, *"Tracking in the SVX"*, CDF internal note 1790, May 1998.

[4] F. Abe *et al.* (The CDF II Collaboration), *"The CDF II Detector Technical Design Report"*, FERMILAB-PUB-96-390-E, Oct 1996.

[5] S. Dell'Agnello *et al.*, *"A Primary Vertex Finding Package"*, CDF internal note 1789, 1992.

[6] C. Campagnari, D. Kestenbaum, *"Review of the SLT Algorithm for Run Ib"*, CDF internal note 3682, May 1996.

[7] F. Abe *et al.* (The CDF Collaboration), *Phys. Rev.* **D 50**, 2966 (1994).

[8] C. Campagnari, D. Kestenbaum, *"The SLT tags and backgrounds for 110 pb^{-1}"*, CDF internal note 3582, May 1996.

Chapter 4

Run II Event samples

With this study we begin to prepare the ground for the Run II analysis of the top-pair production and the subsequent all-hadronic decay.
The search for top in the all-hadronic state has been accomplished successfully in Run I[1][2] and lead to the measurement of the top mass $m_{top} = 186.0 \pm 10.0(stat) \pm 5.7(syst)$ GeV/c^2. In Run II we expect to improve that measurement by reducing the statistical uncertainty by about a factor of 5 due, al least, to a 20x increase in integrated luminosity and a $\approx 30\%$ increase in cross section. We also expect to improve the b-tag efficiency due to both a larger geometrical acceptance and a better performance of the SVXII detector.

4.1 Jets at CDF

Jets are among the most interesting "objects" produced by a high energy collider, as they characterize the experimental signature of many know physical events as well as of new physics. Since they cannot be isolated, quarks and gluons can be studied only indirectly. In particular, the study of a jet gives informations about the initiating parton as it consists of a group of energetic particles which are emitted spatially collimated along the original parton direction.
In $p\bar{p}$ collisions, jet production can be understood as a point-like collision of a quark or gluon from the proton and an (anti)quark or gluon from the antiproton. After colliding, because of fragmentation, these scattered partons manifest themselves as "sprays" of particles called "jets".
In general, any *inelastic* scattering between a proton and an antiproton can be described as an *elastic* collision between a single proton and antiproton constituent. The non-colliding constituents of the incoming proton and antiproton are called "beam fragments" or "spectators" and contribute to the underlying event.

4.1.1 A brief Jet History

Jets were first observed at e^+e^- colliders in 1975 when the center of mass energy reached 6-8 GeV at SPEAR[3]. When PEP and PETRA reached energies of 30-40 GeV, jets were found to be the dominant feature of hadron production.
Jets in hadron collisions were observed for the first time in early 80's at the CERN. The first collaboration to produce results was the UA1 experiment at the S$p\bar{p}$S ($\sqrt{s} = 630$

GeV), which sought direct evidence of the top quark production in the decays of the recently discovered W bosons, $p\bar{p} \rightarrow WX \rightarrow t\bar{b}X$ [4].

4.1.2 Jet Reconstruction

In a collider experiment a jet appears typically as an energy deposit shared among several calorimeter towers. A reconstruct algorithm is then needed to recognize and reconstruct a jet starting from the energy information of each calorimeter tower.
Fig. 4.1 gives us an idea of the jet "development" in the CDF detector. It is the event display of a typical di-jet event where two jets are produced.

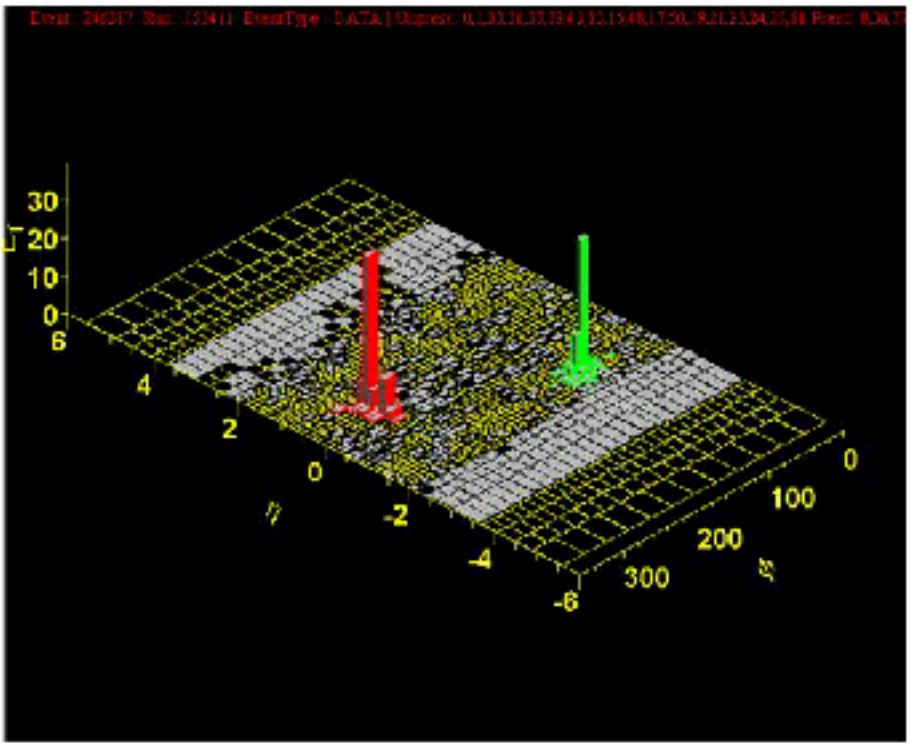

Figure 4.1: *CDF display of a typical di-jet event*

The CDF jet reconstruction process can be divided into two parts: first, a list of towers is assigned to each jet by a clustering algorithm, then the energetic and geometrical information of each tower is combined to reconstruct the jet energy and direction.
The clustering algorithm uses a cone of a fixed radius to define a jet, the calorimeter towers being its basic units. Energetic towers are assigned to jet clusters by an off-line routine (JetClu) implementing the jet-finding algoritm in two steps (see Chapter 3):

- **preclustering**;
- **clustering**.

From the list of towers associated with the cluster, JetClu calculates the jet four-momentum components according to the following definitions:

$$E^J = \sum_{i=1}^{N} E_i \tag{4.1}$$

$$P_x^J = \sum_{i=1}^{N} E_i \sin\theta_i \cos\phi_i \tag{4.2}$$

$$P_y^J = \sum_{i=1}^{N} E_i \sin\theta_i \sin\phi_i \tag{4.3}$$

$$P_z^J = \sum_{i=1}^{N} E_i \cos\theta_i \tag{4.4}$$

$$P_T^J = \sqrt{(P_x^J)^2 + (P_z^J)^2} \tag{4.5}$$

$$E_T^J = E^J \times \frac{P_T^J}{\sqrt{(P_x^J)^2 + (P_z^J)^2}} \tag{4.6}$$

where i is the tower index and N the number of towers in the cluster. The azimuthal angles ϕ_i are evaluated according to the CDF coordinate system while the polar angles θ_i are calculated respect to the event vertex along the beam axis.

Jet corrections

According to CDF definition, jets emerge from a vector sum of the momenta associated to calorimeter towers enclosed in a certain region (cone), under the assumption that all tower contributions come from massless particles originated in the primary vertex[1] and detected in the energy barycenter of each tower. Unambiguous results can be obtained only if adequate corrections, aimed at reducing systematic effects degrading the energy determination, are applied to the raw energies detected by the calorimeters.

Detector. During Run I, central and plug calorimeter relied on different detection techniques (scintillators and gas proportional chambers respectively). This introduced a non-homogeneity in energy response that had to be accounted for. This effect should be substantially reduced in Run II, thanks to the calorimeter plug upgrade, which will rely on scintillators as active medium.

Imperfect calorimeter coverage as well as limited response for low-P_T hadrons, contributes in degrading energy measurements, since little or no energy deposition is detected for particles escaping through detector cracks – in particular at boundaries between the central and plug regions – or for soft hadrons reaching the hadron calorimeter.

Clustering procedure. The clustering procedure described above has a finite resolution essentially imposed by R, the jet $\eta - \phi$ radius. Particles which, during hadronization or subsequent hadron decay, are emitted at large angles, fail to contribute to the jet they would naturally belong to. In the same way, *out-of-cone* losses can be caused by low-P_T particles being trapped in the magnetic field.

Underlying event and multiple interactions. These two phenomena produce observable effects in the jet clustering procedure. In the first case, strong interactions involving

[1] The definition of primary vertex is different for Level 3 and offline jet clustering; in the first case, in fact, the collision is assumed to take place in the detector origin, while in the latter the primary interaction point is reconstructed by means of a beam-constrained fit of all tracks.

beam remnants can introduce a flux of hadrons that can interfere with particles produced in the hard scattering process. This "extra production" of hadrons can have a relapse on the jet definition, since some particles generated in the underlying event can be included in the clustering procedure. The same can happen when multiple interactions occur, *i.e.*, when two (or more) collisions occur during the same beam cross. In this case, therefore, more events are overlapped.

All these effects have been accounted for in the definition of jet corrections, whose aim is to suitably rescale the transverse energy of each jet to a value which represents *the most likely E_T that would have been measured if all the degrading effects were not present*. The most general form for the corrections to be applied to the E_T of a jet (cone $R=\sqrt{\Delta\eta^2+\Delta\phi^2}$) is the following [5]:

$$P_T(R) = (P_T^{raw}(R) \times f_{rel} - UEM(R)) \times f_{abs}(R) - UE(R) + OC(R) \ ,$$

where:

f_{rel}:	relative energy scale factor, correcting for non-uniformities in the detector response;
$UEM(R)$:	correction for multiple interactions;
$f_{abs}(R)$:	absolute energy scale factor, rescaling the raw jet energy into the average true jet energy;
$UE(R)$:	correction for underlying event;
$OC(R)$:	*out-of-cone* losses correction.

The absolute calorimetric energy scale can be estimated by means of a two-step procedure. First, the electromagnetic energy scale can be determined using a sample of $J/\psi \to e^+e^-$ or $Z^0 \to e^+e^-$ events. This can be done exactly as for setting the momentum scale of the tracking system by renormalizing the observed $J/\psi(1S)$ and Z^0 peaks to the corresponding world average values. Hence, this information can be used for calibrating the response of the hadronic calorimeter: once the process $Z^0 \to e^+e^- + 1$ *jet* is considered, the hadronic energy scale can be determined by renormalizing the energy of the single jet to the energy measured for the recoiling leptons.

4.1.3 Monte Carlo Simulations

The main Monte Carlo sample we have used consists of 150000 inclusive $t\bar{t}$ events generated with:

- Herwig, version 6.4;
- $E_{cm} = 1.96$ TeV;
- $M_{top} = 175$ Gev/c^2;

and reconstructed through a realistic simulation of the detector. These events are then processed ("production") in the same way as the data.
Additional samples at different top masses (170, 180 Gev/c^2) or with different generators (PYTHIA) or in different conditions are produced in order to evaluate systematics on the efficiency.

4.2 The Multijet dataset

The dataset most suitable for the $t\bar{t}$ all-hadronic analysis is the multijet one because it replicates better than any other dataset the final state topology, without loosing too much in efficiency.

This dataset is based on the *multijet trigger* which, essentially, requires at least 4 clusters of calorimetric towers with a minimum amount of total energy. In particular, the most recent *multijet* trigger requires:

- at **Level 1**: at least 1 Tower with $E_T \geq 10$ GeV
- at **Level 2** : at least 4 clusters with $E_T^{cluster} \geq 15$ GeV and total energy $\sum E_T \geq 125$ GeV
- at **Level 3**: $N_{jet} \geq 4$, (JetClu) with $R_{cone} = 0.4$ and $E_T^{jet} \geq 10$ GeV

Such trigger has a cross section of about 10 nb and is fully efficient on $t\bar{t}$ all-hadronic events.
The sample we currently have amounts to an integrated luminosity of $100 \pm 6\ pb^{-1}$.

4.3 Multijet dataset Run II vs Run I

Validation of this dataset can be insured by comparing some characteristic distributions to those obtained on the Run I multijet dataset. The most relevant quantities in this dataset are calorimetric and, apart from minor differences due to different calibration of the calorimeters, these quantities should behave in a similar fashion. We compare the distributions for the following calorimetric variables (for $JetClu$ jets, cone size 0.4):

- number of jets with $E_T \geq 15$ GeV and $|\eta| \leq 2.0$;
- E_T of these jets;
- η of these jets;
- total transverse energy, $\sum E_T$, of these jets.

This comparison is limited to events with ≥ 5 jets and $\sum E_T \geq 150$ GeV because this is the Run I dataset we have currently available. Unfortunately the calorimeter response in Run II is about 4% less than in Run I; for this reason we have corrected the jet transverse energy by a factor 1.04.
The figures 4.2, 4.3, 4.4 and 4.5 show indeed that these distributions, for Run I and Run II multijet events, are in close agreement. This gives us confidence on the validity of the approach used in Run I, that is a refinement of the sample through a kinematical selection. This will be the subject of next section.

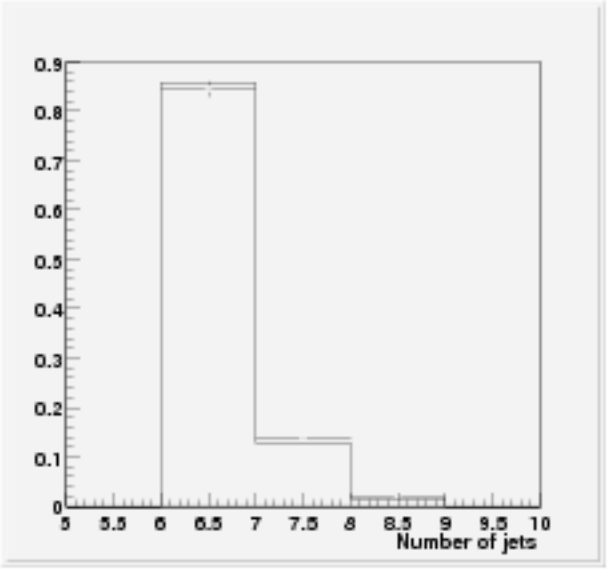

Figure 4.2: *The number of jets (JetClu, cone 0.4, $E_T \geq 15$ GeV, $|\eta| \leq 2.0$). The histogram is for Run I events the points are for Run II events. Distributions normalized to equal area.*

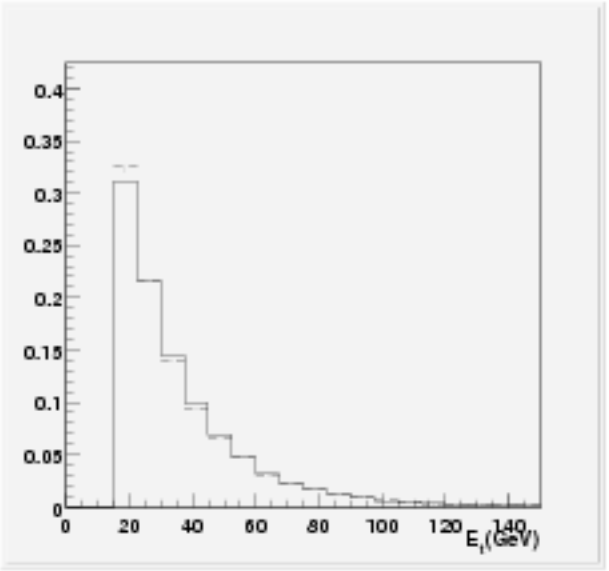

Figure 4.3: *Jet E_T (JetClu, cone 0.4, $E_T \geq 15$ GeV, $|\eta| \leq 2.0$). The histogram is for Run I events, the points are for Run II events. Distributions normalized to equal area.*

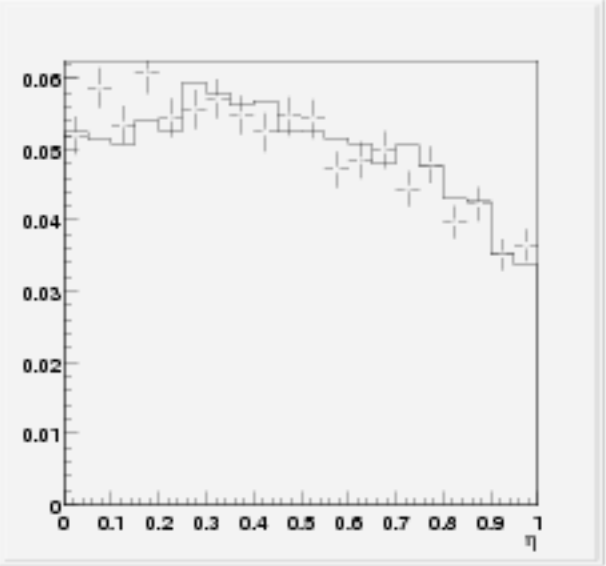

Figure 4.4: *Jet η (JetClu, cone 0.4, $E_T \geq 15$ GeV, $|\eta| \leq 2.0$). The histogram is for Run I events, the points are for Run II events. Distributions normalized to equal area.*

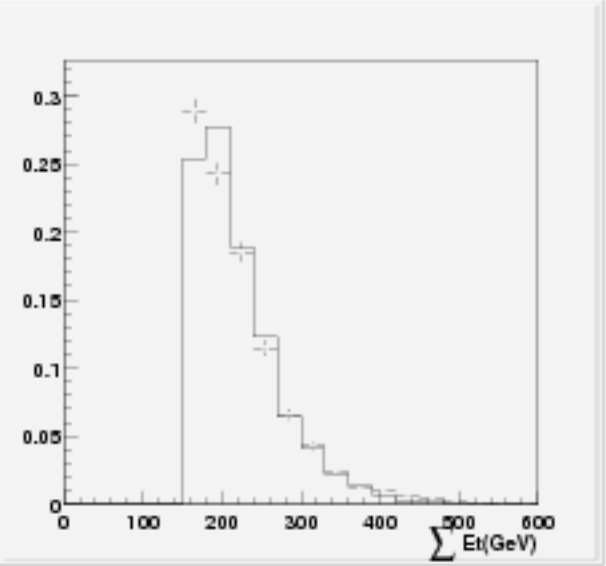

Figure 4.5: *$\sum E_T$ of all jets (JetClu, cone 0.4, $E_T \geq 15$ GeV, $|\eta| \leq 2.0$). The histogram is for Run I events, the points are for Run II events. Distributions normalized to equal area.*

Bibliography

[1] CDF Collaboration, F. Abe *et al.*, *Phys. Rev. Lett.* **79**, 1992(1997).

[2] CDF Collaboration, T. Affolder *et al.*, *Phys. Rev.* **D 63**, 032003 (2001).

[3] V. Barger, R. Phillips, *Collider Physics*, Addison-Wesley (1987).

[4] P. Bagnaia *et al.*, *Z Phys.* **C20**, 117(1983).

[5] T. Affolder *et al.* (The CDF Collaboration), *"Measurement of the Top Quark Mass with the Collider Detector at Fermilab"*, hep-ex0006028, Jun 2000.

Chapter 5

Kinematical Selection

The effective cross section of the multijet dataset (about 10 nb) is much larger than the $t\bar{t}$ one (about 3 pb - level 3 requirements only) corresponding to $S/B \approx 1/3000$: we need a very discriminating selection. We know by Run I experience that a simple first step is to apply a kinematical selection based on calorimetric quantities in order to achieve a *reasonably good* S/B ratio.
As a guideline we will optimize the selection with respect to all-hadronic $t\bar{t}$ events i.e. where both W's decay into jet. In the end, however, we will consider the inclusive efficiency where all possibile W decays are considered.
All jet energies are raw quantities, i.e. those measured in the detector.

5.1 Preliminary Requests

Simple requests are applied for a minimal clean-up of the sample:

- $|Z_{vert}| \leq 60$ cm based on the 28 cm RMS beam spread in z
- $\sum E_T \leq 2000$ GeV, $\not\!\!E_T / \sqrt{\sum E_T} \leq 6$ GeV$^{\frac{1}{2}}$ to reject a few patological events.

5.2 Lepton removal

In order to obtain a sample orthogonal to the ones used for other $t\bar{t}$ searches, we reject events which contain at least one good high energy electron ($E_T \geq 20$ GeV) or one good high-p_T muon ($p_T \geq 20$ GeV/c).

5.3 The topology

The first real step requires a topology consistent with the basic process: $t\bar{t} \rightarrow bq\bar{q}\bar{b}q\bar{q}$. The number of jets is not always six because jets can blend or can get lost along the beam line. Besides, the radiation can produce other additional jets in the final state. For these reasons (fig. 5.1), the selection requires a number of jets (*JetClu*, cone 0.4, $E_T \geq 15$ GeV, $|\eta| \leq 2.0$):

$$5 \leq N_{jet} \leq 8$$

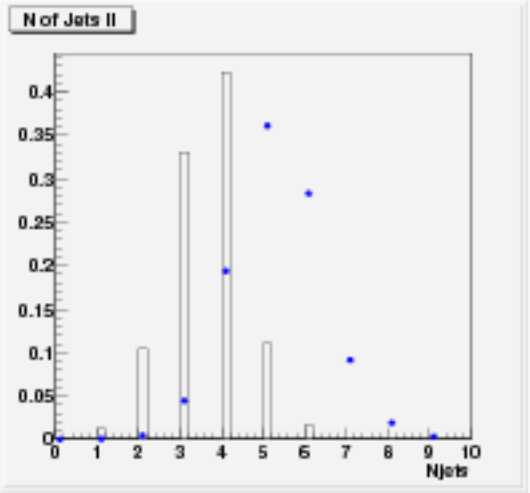

Figure 5.1: *Number of jets (JetClu, cone 0.4, $E_T \geq 15$ GeV, $|\eta| \leq 2.0$). The histogram is for multijet events, the points are for $t\bar{t}$ all-hadronic events. Distributions normalized to equal area.*

The efficiency of this selection is about 76% on all-hadronic $t\bar{t}$ events, while 12% of the multijet events survive the cut.

5.4 Additional kinematical variables

We start using variables considered in the Run I kinematical selection:

1. $\sum E_T = \sum_{i=1}^{N_{jet}} E_T^i$, the total transverse energy of considered jets;
2. $\sum E_T/\sqrt{\hat{s}}$, the *centrality*, i.e., the fraction of the hard scatter energy which goes in the transverse plane;
3. $\mathrm{A} = \frac{3}{2} Q_1$, the *aplanarity* calculated in the center-of-mass of N jets.;
4. $\sum_3 E_T$, the non leading total energy obtained removing the two more energetic jets.

5.4.1 $\sum E_T$

Fig. 5.2 shows the spectrum in $\sum E_T$ for all-hadronic $t\bar{t}$ events and for the multijet events normalized at the same area. It is evident that this variable is very discriminant.

The cut on $\sum E_T$ is chosen at the value which maximizes the statistic significance of the signal, i.e., the ratio $\mathbf{signal}/\sqrt{\mathbf{background}}$ (see fig. 5.3), where the background is represented by the multijet events themselves.

This value corresponds to:

$$\sum E_T \geq 250 \text{ GeV}$$

Only 8% of the surviving multijet events pass this cut, while the relative efficiency is about 61% on all-hadronic $t\bar{t}$ events.

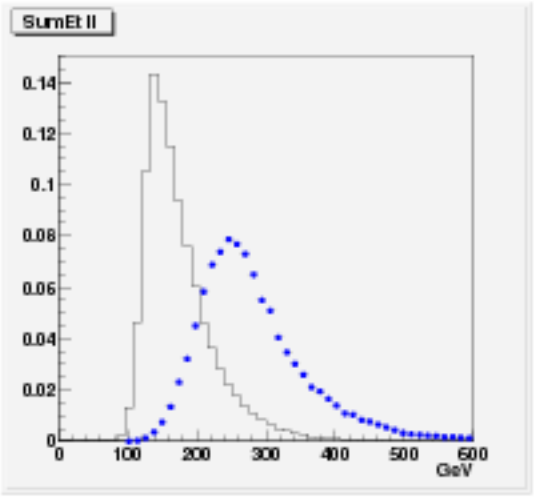

Figure 5.2: $\sum E_T$ *(JetClu, cone 0.4,* $E_T \geq 15$ *GeV,* $|\eta| \leq 2.0$*) for events with* $5 \leq N_{jet} \leq 8$*. The histogram is for multijet events, the points are for* $t\bar{t}$ *all-hadronic events. Distributions normalized to equal area.*

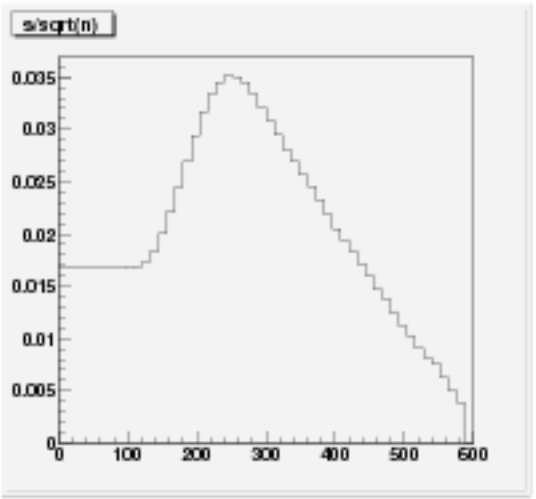

Figure 5.3: *Signal significance as a function of the* $\sum E_T$ *cut*

5.4.2 Centrality

Another characteristic of the all-hadronic $t\bar{t}$ events is the "centrality" of the energy: the jets coming from the $t\bar{t}$ decay are emitted quite perpendicularly respect the beam direction. For this reason, we expect a centrality distribution close to 1 for all-hadronic $t\bar{t}$ events while for background events we have $\sum E_T/\sqrt{\hat{s}}$ smaller than 1.
The distributions, after cutting on $\sum E_T$, are showed in fig. 5.4.

Since the maximum value of $S/\sqrt{B}$ as a function of $\sum E_T/\sqrt{\hat{s}}$ is reached around 0.75 (fig. 5.5) we require:

$$\sum E_T/\sqrt{\hat{s}} \geq 0.75$$

54% of the surviving multijet events remains after this cut and the relative efficiency on the $t\bar{t}$ all-hadronic events is about 83%.

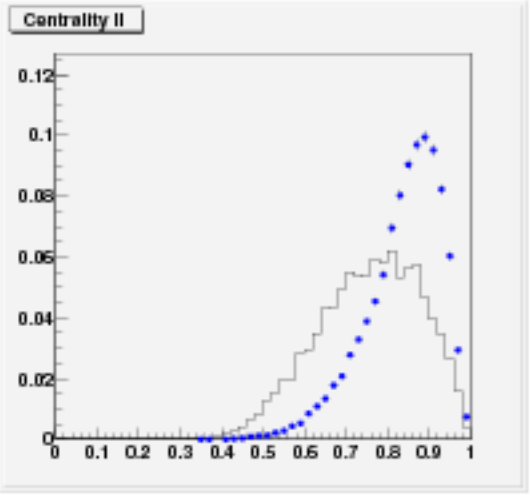

Figure 5.4: *Centrality (JetClu, cone 0.4, $E_T \geq 15$ GeV, $|\eta| \leq 2.0$) for events with $5 \leq N_{jet} \leq 8$ and $\sum E_T \geq 250$ GeV. The histogram is for multijet events, the points are for $t\bar{t}$ all-hadronic events. Distributions normalized to equal area.*

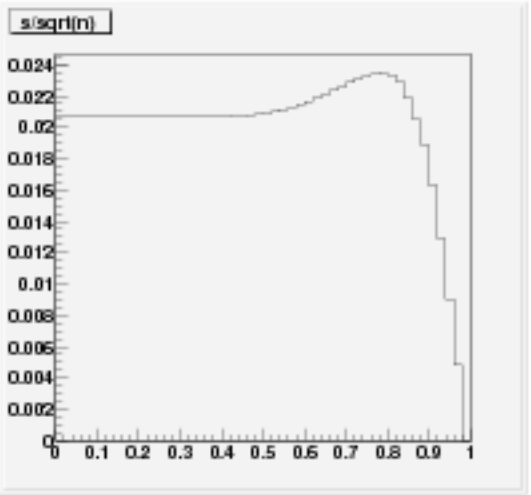

Figure 5.5: *Signal significance as a function of the $\sum E_T/\sqrt{\hat{s}}$ cut.*

5.4.3 Aplanarity and non-leading energy

At this point the distribution in space of jets is very important, and in particular we consider the variable *Aplanarity* [1]. The QCD processes are described as scattering processes $2 \to 2$, where the final partons emit gluon radiation which produces other independent jets. For this reason, the event aplanarity is not equal to zero but still quite small.
Instead, in the all-hadronic $t\bar{t}$ events the aplanarity has a larger value, in particular for the "heavy" top quark mass.
Using the same considerations, there is another variable which can permit to separate the signal from the background. It is the total transverse energy of the jets without the two jets with the highest E_T, $\sum_3 E_T$. Fig. 5.6 shows the distributions of aplanarity versus

[1] Aplanarity is defined as $A = \frac{3}{2}Q_1$, where Q_1 is the smallest of the three normalized eigenvalues of the sphericity tensor $M_{ab} = \sum_j P_a^j P_b^j$, P^J being the jet four-momentum. Aplanarity values range between 0 (in the case of two opposite jets) and 0.5 (for more evenly distributed jets).

$\sum_3 E_T$ for the $t\bar{t}$ events and for the multijet events and it is clear that QCD events have low values for both variables while $t\bar{t}$ events are distributed at higher values.

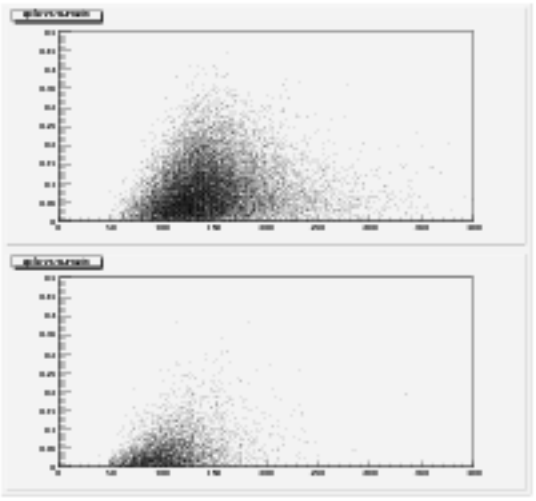

Figure 5.6: *Aplanarity versus $\sum_3 E_T$ for $t\bar{t}$ all-hadronic events (first plot) and for multijet events (second plot) for events with $5 \leq N_{jet} \leq 8$, $\sum E_T \geq 250$ GeV and $\sum E_T/\sqrt{\hat{s}} \geq 0.75$.*

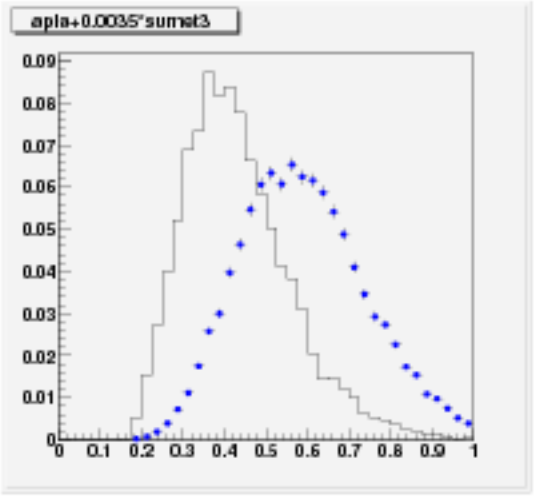

Figure 5.7: *Aplanarity + 0.0035$\times \sum_3 E_T$ for events with $5 \leq N_{jet} \leq 8$, $\sum E_T \geq 250$ GeV and $\sum E_T/\sqrt{\hat{s}} \geq 0.75$. The histogram is for multijet events, the points are for $t\bar{t}$ all-hadronic events. Distributions normalized to equal area.*

As made in Run I, we decide to cut the bottom-left corner of the scatter plot by requiring:

$$\mathrm{A} \geq (-\ 0.0035 \times \sum_3 E_T + 0.55)$$

The first coefficient has been chosen after several trials while the second one (see fig.5.7) has been optimized for the maximum significance (see fig.5.8).

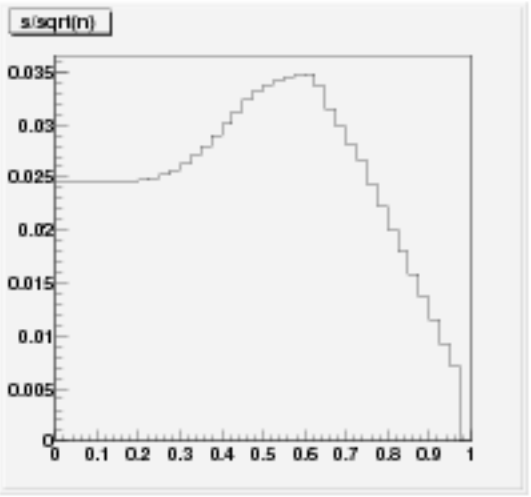

Figure 5.8: *Signal significance as a function of the A + 0.0035× $\sum_3 E_T$ cut.*

This final cut has a relative efficiency of 58% on all-hadronic $t\bar{t}$ events, while accepting 17% of the surviving multijet events.

5.5 Final kinematical selection

In summary, the uncertainty on the kinematical selection requires:

1. $|Z_{vert}| \leq 60$ cm
2. $\sum E_T \leq 2000$ GeV, $\not\!\!E_T / \sqrt{\sum E_T} \leq 6$ (GeV$^{\frac{1}{2}}$)
3. no high-p_T leptons (e or μ)
4. $5 \leq N(jet) \leq 8$ ($E_T \geq 15$ GeV, $|\eta| \leq 2.0$)
5. $\sum E_T \geq 250$ GeV
6. $\sum E_T / \sqrt{\hat{s}} \geq 0.75$
7. A + 0.0035× $\sum_3 E_T \geq 0.55$

and its performance is described in Table 5.1 [2].

[2] In a first period of data taking the trigger had no Level 2 requirements; these difference disappear once the kinematical cuts are applied.

Table 5.1: *Kinematical selection summary.ϵ-Cum represents the cumulative efficiency of the cuts applied in cascade, while ϵ-Rel is the relative efficiency of each cut. ($\int \mathcal{L}dt = 100 \pm 6\ pb^{-1}$)*

Cut	MJ Events	ϵ-Cum	ϵ-Rel	S/B
Multijet Trigger	1086208	99%	99%	1/5000
Clean-up	1017054	96%	97%	1/3400
NO Tight Leptons	1009789	96%	99%	1/3400
$5 \leq N(jet) \leq 8$	130967	73%	76%	1/600
$\sum E_T \geq 250$ GeV	11025	45%	61%	1/80
$\sum E_T/\sqrt{\hat{s}} \geq 0.75$	5989	37%	83%	1/50
$A + 0.0035 \times \sum_3 E_T \geq 0.55$	1023	22%	58%	1/15

In conclusion, these cuts select 1023 events (on 100 pb^{-1}) with an "exclusive" efficiency (on all-hadronic $t\bar{t}$ events) $\epsilon = 22\%$, corresponding to $S/B \approx 1/15$ (assuming $\sigma_{t\bar{t}} \approx 7$ pb and BR($t\bar{t} \rightarrow$ all-hadronic) $= 44\%$. Instead if we consider all possible W decays we have an "inclusive" efficiency $\epsilon = (10.4 \pm 0.1)\%$ and a slighty better ratio $S/B \approx 1/14$.
Unfortunately, this ratio is not good enough: we need to recur to the *b-tag*.

5.6 Systematic uncertainty on the kinematical efficiency

In order to evaluate the systematic uncertainty on the eveluation of the kinematical efficiency we have generated samples with different generators and different top masses (170 and 180 GeV/c^2):

- HERWIG (default)
- HERWIG with all jet E_T's increased by 4%
- HERWIG with all jet E_T's decreased by 4%
- PYTHIA (default)
- PYTHIA with initial state radiation turned off
- PYTHIA with final state radiation turned off

For the dependence on the energy scale uncertainty we have compared the efficiencies obtained when the jet energies are increased/decreased by a conservative 4% [3].
For the gluon radiation modeling we have compared PYTHIA (default) efficiency with the ones obtained when turning off initial/final state radiation.
In addition, since the top mass is know with an uncertainty of ≈ 5 GeV/c^2, we compare the efficiencies obtained for a top mass of 170 and 180 GeV/c^2.
We summarize all these relative uncertainties in table 6.2.

[3]This is a preliminary rough evaluation. Once a full set of studies of the jet energies are completed, we will expect a smaller uncertainty on the scale.

In all cases we have taken the semi-difference between the two compared situations. The total systematical uncertainty is taken as the quadrature sum af all sources: 29%.

Table 5.2: *Summary of systematic uncertainties.*

Source	Relative uncertainty
Energy Scale	14%
Fragmentation	11%
Mass	10%
Radiation (ISR)	14%
Radiation (FSR)	16%
Total	29%

In conclusion the efficiency of the kinematical selection is $(10.4 \pm 2.9)\%$.

Chapter 6

Search for Top events using Secondary Vertex B-Tagging

Our method for isolating a top signal within the multijet sample is the selection of events with at least one jet arising from b quark production. Given the relatively long b quark lifetime ($\tau_b = 1.46 \pm 0.06$ ps) we can *tag* long-lived hadrons within jets. The decay of a long-lived hadron produces a signature of several charged particle trajectories emanating from a point, or secondary vertex, separated from the $p\bar{p}$ interaction, or primary vertex. We describe below this secondary vertex b-tagging technique and verify that it selects b jets in control samples. We then calculate the number of tagged events expected in the multijet sample from background sources.
From this point on the role of the silicon detector is essential. For this reason we limit ourselves to the runs in which the silicon detectors (SVX and ISL) were indeed powered-up and integrated in the data acquisition. This dataset amounts to (69 ± 4) pb^{-1}.

6.1 Secondary Vertex Algorithm

In order to identify b-hadron decays within a jet, we search for its decay products, particles which appear as charged tracks originating from a point separated from the $p\bar{p}$ interaction by a significant distance, as indicated schematically in figure 6.1.

The $p\bar{p}$ interaction point is called the *primary vertex* and the b-hadron decay point is called *the secondary vertex*. Most particles in an event, even in presence of real displaced secondary vertex, will emanate from the primary vertex. In order to distinguish a secondary vertex from the primary vertex, we base ourselves on the following quantities:

- the quality used to reconstruct the track in SVX;
- the track p_T;
- the impact parameter d with respect to the primary vertex and its error σ_d .

The algorithm SecVtx uses the spatial resolution of the Silicon Vertex Detector to determine the presence of secondary vertices in the event.

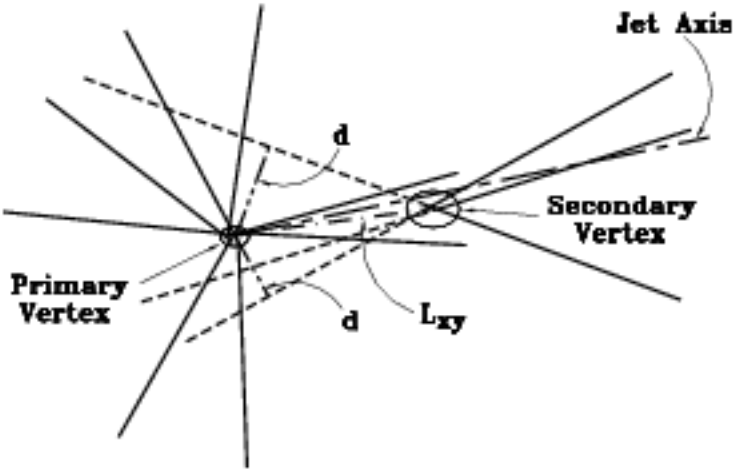

Figure 6.1: *Simplified 2d projection of an event containing a jet with a secondary vertex.*

6.1.1 Selection of the tracks sample

SecVtx takes the position of primary vertex from the average beamline which is filled for each run[1]. Such beamline is known with an uncertainty of about 30 μm. The algorithm counts the number of axial and stereo hits present in all layers of SVX and ISL to know the number of hits shared between one track and the other. After that, only the hits not shared between two or more tracks are counted and we call these hits as "fiducial". Using these information SecVtx selects a group of "fiducial" tracks as shows in table 6.1:

Table 6.1: *"Fiducial" tracks for SecVtx.*

Type of tracks	axial hits	axial and "fiducial" hits	stereo and "fiducial" hits
"fiducial" in the COT	≥ 3	≥ 1	≥ 0
reconstructed only in the Silicon	≥ 5	≥ 3	≥ 3

The algorithm considers as "fiducial" in the COT only the tracks which have at least 4 hits in 2 axial superlayers and 2 stereo superlayers. From this group of "fiducial" tracks, SecVtx chooses two subsamples called respectively "pass 1" and "pass 2"; our selection changes if SecVtx works with *2d* modality or with *3d* modality.
In fact, in *2d* modality these characteristics are required for the tracks:

- Pass 1:
  1. $|S(d_0)| \geq 2.5$
  2. $p_T \geq 0.5$ GeV/c
- Pass 2:
  1. $|S(d_0)| \geq 3$

[1] In the near future we expect this to be replaced by an event-by-event vertex with a smaller uncertainty.

2. $p_T \geq 1$ GeV/c

while for *3d* modality:

- Pass 1:
  1. $\sqrt{S(d_0)^2 + S(z_0)^2} \geq 2.5$
  2. $p_T \geq 0.5$ GeV/c
- Pass 2:
  1. $\sqrt{S(d_0)^2 + S(z_0)^2} \geq 3$
  2. $p_T \geq 1$ GeV/c

The selections are determined by the requests on the significance of d_0 ($S(d_0) = d_0/\sigma_{d_0}$) and z_0 ($S(z_0) = (z_0 - z_{vert})/\sigma_{z_0}$).

6.1.2 Secondary Vertex finding

The algorithm finds the secondary vertex by forcing all available tracks (with hits in SVX) to originate from the same point. By an iterative procedure, the track with higher χ^2 is eliminated and this process continues until the secondary vertex has at least 2 tracks with a value of χ^2 under an opportune threshold. For this reason we call "taggable" jets with at least 2 pass 1 or pass 2 tracks.

6.1.3 Definition of the Tags

Having found the secondary vertex, SecVtx moves on to the effective procedure of the jet tagging. According to the used modality, the algorithm calculates the decay length of secondary vertices, L_{xy} (L_{3d} if used *3d* modality). L_{xy} is the projection of the 2d vector from the primary to the secondary vertex, $\vec{x}_{sec} - \vec{x}_{prim}$, on the transverse jet direction:

$$L_{xy} = (x_{sec} - x_{prim}) \cos\phi_{jet} + (y_{sec} - y_{prim}) \sin\phi_{jet} \tag{6.1}$$

L_{3d}, instead, is the same projection but in the tridimensional space:

$$L_{3d} = L_{xy} \sin\theta_{jet} + (z_{sec} - z_{prim}) \cos\theta_{jet} \tag{6.2}$$

SecVtx considers generated by heavy quarks (*positive tags*) the jets with L_{xy} significance ($L_{xy}/\sigma_{L_{xy}}$) greater then a fixed value while takes as *negative tags* the jets with a decay length less then a negative value. Usually the negative tags are due to errors of reconstruction and are called *mis-tags*.

6.2 b-tagging efficiency on $t\bar{t}$ events

To better define the b-tagging efficiency, we factorize it to account for different components. The total efficiency can be defined as:

$$\epsilon_b = \epsilon_{taggable} \times \epsilon_{tag}^{overall-event} \tag{6.3}$$

where:

- $\epsilon_{taggable}$ is the efficiency to find at least 1 taggable jet in the event
- $\epsilon_{tag}^{overall-event}$ is the efficiency to tag at least 1 taggable jet in the event

In particular, accounting for the possibility of tagging jets not from heavy flavors (non B-jet), as opposed to jets really coming from heavy flavors (B-jet):

$$\epsilon_{tag}^{overall-event} = \epsilon_{btag}^{event} + \epsilon_{mistag}^{event} - (\epsilon_{btag}^{event} \times \epsilon_{mistag}^{event}) \tag{6.4}$$

with :

- $\epsilon_{mistag}^{event}$ being the fraction of starting events with at least 1 tagged non B-jet
- ϵ_{btag}^{event} being the fraction of starting events with at least 1 tagged B-jet

This fraction is equal to:

$$\epsilon_{btag}^{event} = F_{2b} \times \epsilon_{btag} \times SF \times (2 - \epsilon_{btag} \times SF) + F_{1b} \times \epsilon_{btag} \times SF \tag{6.5}$$

where:

- F_{2b} = fraction of starting events that contain 2 taggable B-jets
- F_{1b} = fraction of starting events that contain 1 taggable B-jets
- SF = scale factor, that is a factor which relates the efficiency evaluated on Monte Carlo events to that evaluated on real heavy flavor data (more on this later)
- ϵ_{btag}=per jet b-tagging efficiency as measured in the $t\bar{t}$ Monte Carlo

All the number relevant for these calculation are summarized in table 6.2, and are obtained from the subset of the 150000 $t\bar{t}$ simulated events which passed the full kinematical selection.

Table 6.2: *Elements used in the b-tagging efficiency evaluations.*

Total number of events	15605
Total number of jets	334284
Jets matched to a b-quark	29934
Jets matched to a b-quark and Taggable	23841
Events with 1 jet matched to a b Taggable	4938
Events with 2 jets matched to a b Taggable	8735
Jets matched to b-quarks and Tagged positive	9772
Jets matched to b-quarks and Tagged negative	252
$\epsilon_{taggable}$	$(87.6 \pm 0.3)\%$
ϵ_{btag}	$(39.9 \pm 0.3)\%$
ϵ_{mistag}	$(2.0 \pm 0.3)\%$
F_{1b}	0.316 ± 0.004
F_{2b}	0.559 ± 0.004
ϵ_{btag}^{event}	$(48.4 \pm 0.7)\%$
$\epsilon_{btag}^{overall-event}$	$(45 \pm 1)\%$
ϵ_b	$(40 \pm 1)\%$

The scale factor (SF) has been calculated [2] by comparing the per-jet b-tagging efficiency (ϵ_{btag}) in QCD $b\bar{b}$ simulated events to the experimental efficiency evaluated in heavy flavor enriched events, that is events where one electron is embedded within a jet. Such factor amounts to 0.89 ± 0.09 (see figure 6.2).

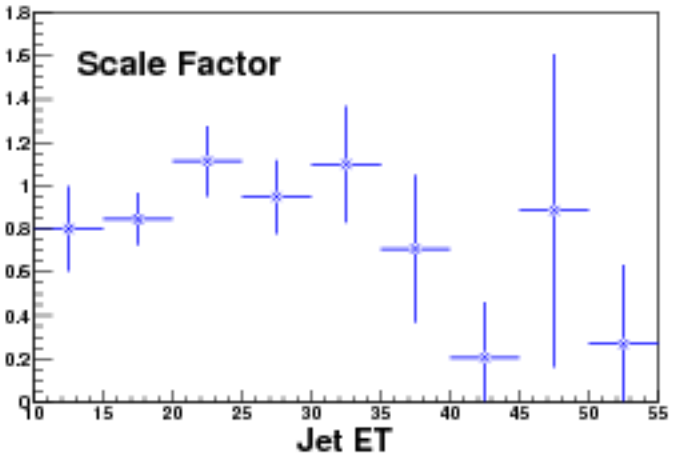

Figure 6.2: *Scale factor as a function of jet E_T.*

The b-tagging efficiency on $t\bar{t}$ events is $(40 \pm 1(\text{stat}) \pm 4(\text{syst}))\%$.

6.3 b-tagging on Multijet events

In the multijet sample we expect the presence of tags coming from processes different from $t\bar{t}$ production. These processes are:

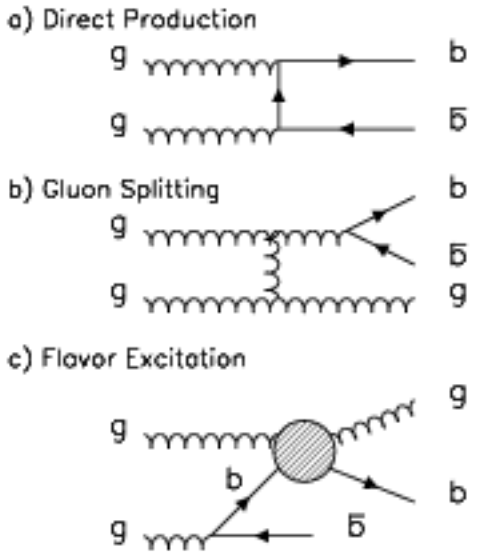

Figure 6.3: *Three sources of heavy flavour in inclusive jets: a) direct production; b) gluon splitting; c) flavour excitation.*

- QCD production of $b\bar{b}$ [1] by: direct production, gluon splitting or flavour excitation (fig.6.3);
- W and Z bosons production with radiation which produces $b\bar{b}$ by gluon splitting;
- W and Z bosons production with W/Z decaying into heavy flavors;
- mis-tag.

The most important background contribution is the first process.

6.3.1 QCD background

The method to estimate this source of background is based on the assumption that the contribution of the QCD processes, which give tags in the sample with $N_{jet} = 4$ remains the same as the jet multiplicity increases. With this ipothesis, when the probability for a taggable jet in the $N_{jet} = 4$ control sample to be tagged is determined then it can be used on the jets of other samples to estimate the number of expected tags. Such a probability (*tag rate*) is defined as:

$$\mathcal{P} = \frac{\#\ of\ tagged\ jets}{\#\ of\ taggable\ jets}$$

From now on we consider only positive tags because negative ones are used neither to isolate a signal nor for background evaluation.

6.3.2 Characteristics of Multijet sample

To determine which variables are more suitable for the parametrization of the tag probability, we have studied its dependence on:

- specific jet variables as E_T, η, ϕ and the number of taggable tracks (N_{trk}) into the jet cone (see figs.6.4, 6.5, 6.6, 6.7)

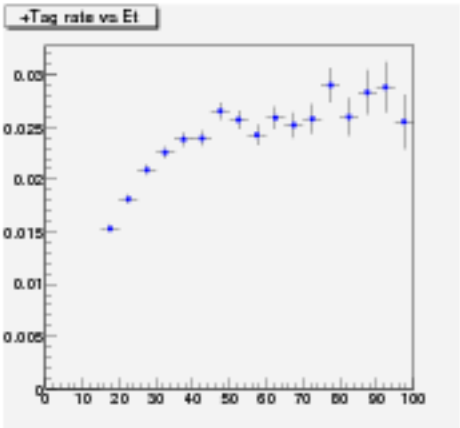

Figure 6.4: *Positive tag rate as a function of jet E_T.*

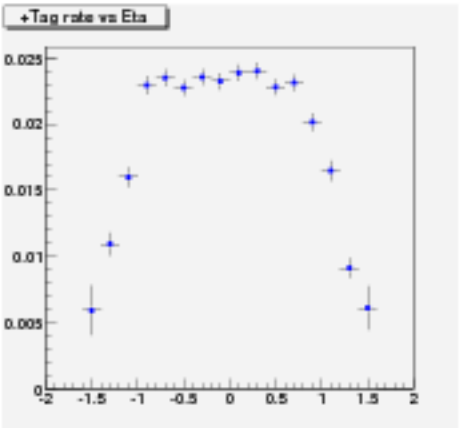

Figure 6.5: *Positive tag rate as a function of jet η.*

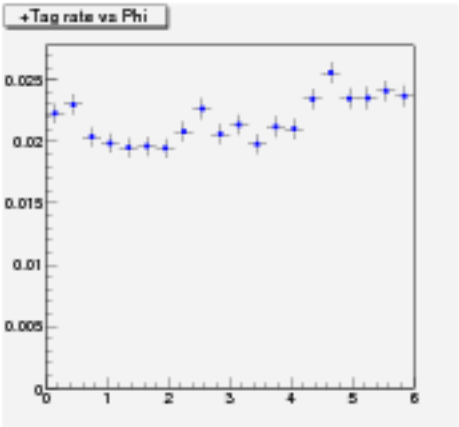

Figure 6.6: *Positive tag rate as a function of jet ϕ.*

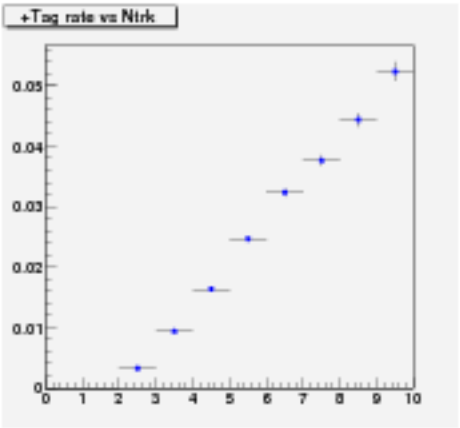

Figure 6.7: *Positive tag rate as a function of the number of SVX tracks inside the jet.*

- global variables as instantaneous luminosity and data taking period (Run number) (see figs. 6.8, 6.9).

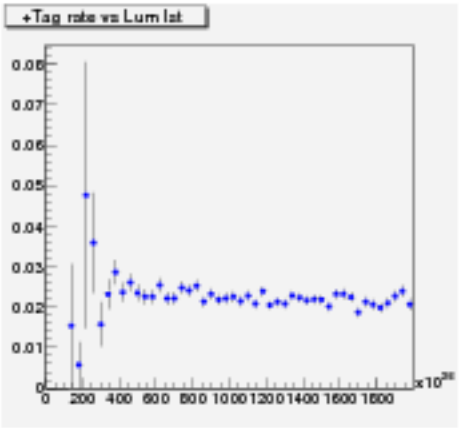

Figure 6.8: *Positive tag rate as a function of the instantaneous luminosity.*

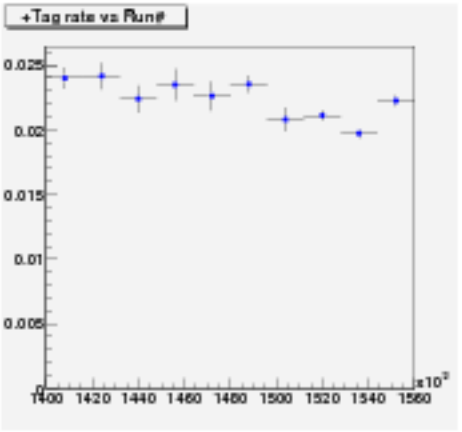

Figure 6.9: *Positive tag rate as a function of the run number.*

6.3.3 Tag rate parametrization

It is reasonable to parametrize the rate in terms of jet-E_T, jet-η and number of SVX tracks, N_{trk}. The tag rate is then:

$$\mathcal{P} = \mathcal{P}(E_T, \eta, N_{trk})$$

With this choice we evaluate a 3-dimensional matrix[2] of positive tag rates in the control sample of events with exactly 4 jets.
The contribution to the total number of expected tags from the i-th event with n taggable jets is calculated as:

$$N^i_{exp} = \sum_{j=1}^{n} \mathcal{P}(E^j_T, \eta^j, N^j_{trk})$$

while the expected background over all N events amounts simply to:

$$N_{exp} = \sum_{i=1}^{N} N^i_{exp}$$

At this point, we are interested in checking that the matrix so obtained predicts well the number of tags observed in our sample, and that all relevant kinematical distributions are well reproduced.
As first thing we compare the $\sum E_T$, $\sum E_T/\sqrt{\hat{s}}$ and $A + 0.0035 \times \sum_3 E_T$ distributions for the events with at least one *observed* tag to what *expected* from the application of the tag parametrization in the control sample. We see in fig.6.10 that these distributions are quite well reproduced, both in normalization and in shape.

[2] 6 bins in E_T, 3 bins in η, 11 bins in N_{trk}

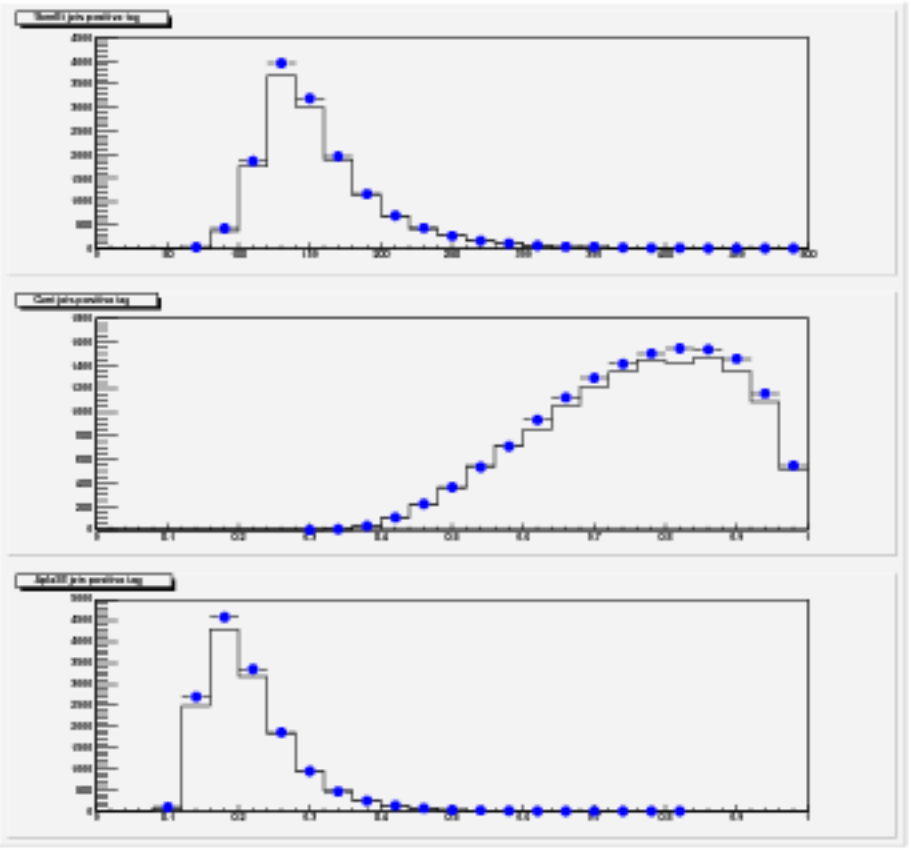

Figure 6.10: $\sum E_T$, $\sum E_T/\sqrt{\hat{s}}$ *and* $A + 0.0035 \times \sum_3 E_T$ *distributions for the* observed *(histogram) and* expected *(points) events with at least one tag, in the control sample with 4 jets.*

For instance, see table 6.3, the number of observed/expected tags with $\sum E_T \geq 250$ GeV agree within 10%. The agreement is within 4% for events with $\sum E_T/\sqrt{\hat{s}} \geq 0.75$. As for the events with large values of $A + 0.0035 \times \sum_3 E_T$ we see for instance an agreement within 3% for events with $A + 0.0035 \times \sum_3 E_T \geq 0.3$[3].

Table 6.3: Observed and Expected Tags for events with 4 jets, $\sum E_T \geq 250$ GeV, $\sum E_T/\sqrt{\hat{s}} \geq 0.75$ and $A + 0.0035 \times \sum_3 E_T \geq 0.3$.

Cut	$\sum E_T \geq 250$ GeV	$\sum E_T/\sqrt{\hat{s}} \geq 0.75$	$A + 0.0035 \times \sum_3 E_T \geq 0.3$
Obs Tags	190	2269	409
Exp Tags	173 ± 13	2332 ± 48	393 ± 20
$\frac{N_{obs}-N_{exp}}{N_{exp}}$ (%)	10 ± 8	-3 ± 2	4 ± 5

We then consider the numbers of *observed* and *expected* tags for events with respectively 4, 5, 6 and ≥ 7 jets:

[3]The actual cut at 0.55 depletes too much the distribution. Cutting at 0.3 on the control sample isolate about 15% of the upper end of the distribution. This is the same as what happens on the signal sample when we cut at 0.55

Table 6.4: Observed and Expected Tags in our sample. Errors are statistical only.

N(jet)	4	5	6	≥ 7
Events	283952	75569	11259	1479
Taggable jets	664735	222068	40067	6361
Obs Tags	14484	4704	761	137
Exp Tags	14484 $\pm$ 118	4712.6 $\pm$ 67.5	850.0 $\pm$ 28.5	133.6 $\pm$ 11.3
$\frac{N_{obs}-N_{exp}}{N_{exp}}$ (%)	-	0.2 $\pm$ 1.4	-10 $\pm$ 3	2 $\pm$ 9

We see that the 5 and 7 jet subsamples are well reproduced while there is a significant overestimate in the 6 jet subsample. If we consider the average observed tag rate we see that indeed it is smaller in the 6 jet subsample (1.9%) with respect to events with 4, 5 and 7 jets (2.2%, 2.1% and 2.2% respectively). This is an indication that the reason for the disagreement resides more in the observed rather than in the expected tags. To be conservative we consider a 10% systematic uncertainty on the background prediction based on this jet multiplicity dependence, to which we add in quadrature 10% from the dependence on the other kinematical cuts, for a total 14%.

Bibliography

[1] M.L. Mangano, *Nucl. Phys.*, B405 (1993) 536

[2] D. Amidei et al, *CDF Note*, 6329

Chapter 7

Measurement of the $t\bar{t}$ Cross Section

In this chapter we want to summarize the results from the analysis of the multijet sample after the application of the kinematical selection and the request of at least one b-tag in the event.
Unfortunately both the statistical and systematical uncertainties on the expected background are large, making it difficult to extract a signal and a cross section measurement. For this reason we will introduce an alternative way of estimating the background enabling us to make a preliminary measurement of $\sigma_{t\bar{t}}$.

7.1 Results on the signal sample

The kinematical selection and the b-tagging algorithm are described in chapter 5 and 6 respectively. We can summarize the analysis as:

- $5 \leq N(jet) \leq 8$ ($E_T \geq 15$ GeV, $|\eta| \leq 2.0$)
- $\sum E_T \geq 250$ GeV
- $\sum E_T/\sqrt{\hat{s}} \geq 0.75$
- A + 0.0035$\times \sum_3 E_T \geq 0.55$
- at least 1 secondary vertex (b-tag) in the event.

In table 7.1 the results of the analysis are shown: a small excess of observed tags is seen with respect to the expected ones. Such an excess can be abscribed to $t\bar{t}$ production but is quite smaller than what expected ($\sim$ 25 tags assuming $\sigma_{t\bar{t}} = 7$ pb).

Table 7.1: Observed and Expected Tags in the signal sample after kinematical selection. The first error is statistical and the second one is systematical. ($\int \mathcal{L}dt = 69 \pm 4\ pb^{-1}$)

N(jet)	5	6	≥ 7	total
Events	262	277	144	683
Obs Tags	27	34	15	76
Exp Tags	$26.0 \pm 5.0 \pm 3.6$	$31.2 \pm 5.5 \pm 4.4$	$17.5 \pm 4.1 \pm 2.5$	$74.7 \pm 8.5 \pm 10.5$

Unfortunately, due to the limited statistics (only 69 pb^{-1} with respect to the 110 pb^{-1} used in Run I) the uncertainties on the estimated background are similar in size to the expected signal. This makes it difficult to obtain a significant measurement, so we try to estimate the background in a different way.

7.2 Alternative background estimate

Since the distribution of the quantity A + 0.0035× $\sum_3 E_T$ expected from the application of the tag rate reproduce well in shape the observed distribution (see fig.6.10), we want to use both and perform a two-component fit in order to extract the amount of signal and background present in our sample. To do so we release the last cut of the kinematical selection and derive:

- the distribution of A + 0.0035× $\sum_3 E_T$ for the $t\bar{t}$ Monte Carlo events with at least 1 b-tag(the signal "template")
- the distribution of A + 0.0035× $\sum_3 E_T$ for the multijet events, weighed by the probability to be tagged (the background "template")

These distribution are then fitted (see fig.7.1) to a 7^{th} degree polynomial to extract an analytical probability density of being background or signal.

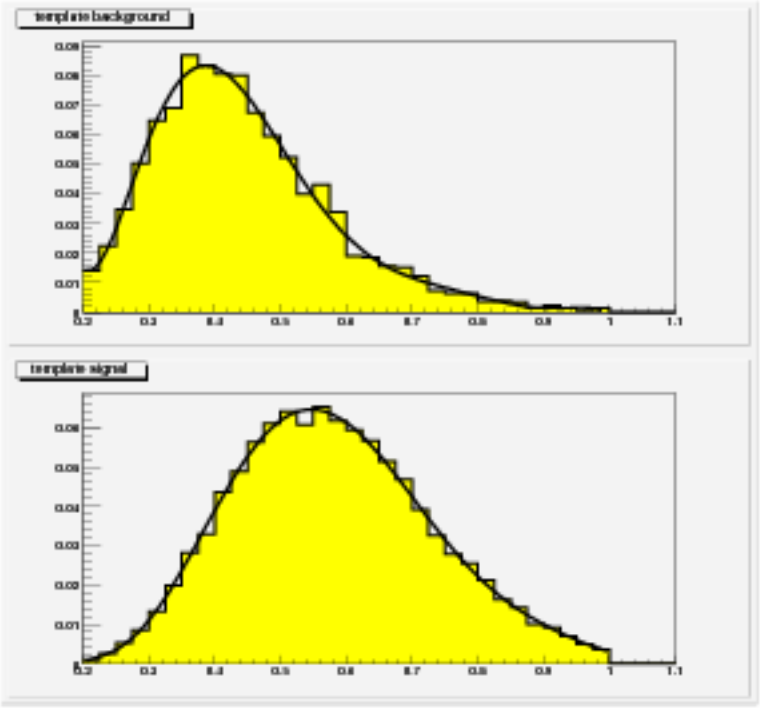

Figure 7.1: *A + 0.0035× $\sum_3 E_T$ distribution. Top: background "template"; bottom: signal "template". A fit to a 7^{th} degree polynomial is superimposed.*

We then request the presence of at least one b-tag in the event and define an unbinned likelihood as:

$$L = \prod_{i=1}^{N_{cand}} \frac{n_b f_b(i) + n_s f_s(i)}{n_b + n_s} \tag{7.1}$$

where:

- x_i represent the value of A + 0.0035$\times \sum_3 E_T$ for the i-th event
- n_b and n_s are respectively the number of background and signal events (in particular we consider n_s = (N_{cand} - n_b))
- f_b and f_s are the probability densities for background and signal respectively.
- N_{cand} = 347 is the number of candidate events passing the alternative kinematical selection and with at least 1 b-tag.

From the maximization of this likelihood (i.e. the minimization of -ln(L)) we obtain

$n_b = 336^{+11}_{-16}$ background events (see fig.7.2).

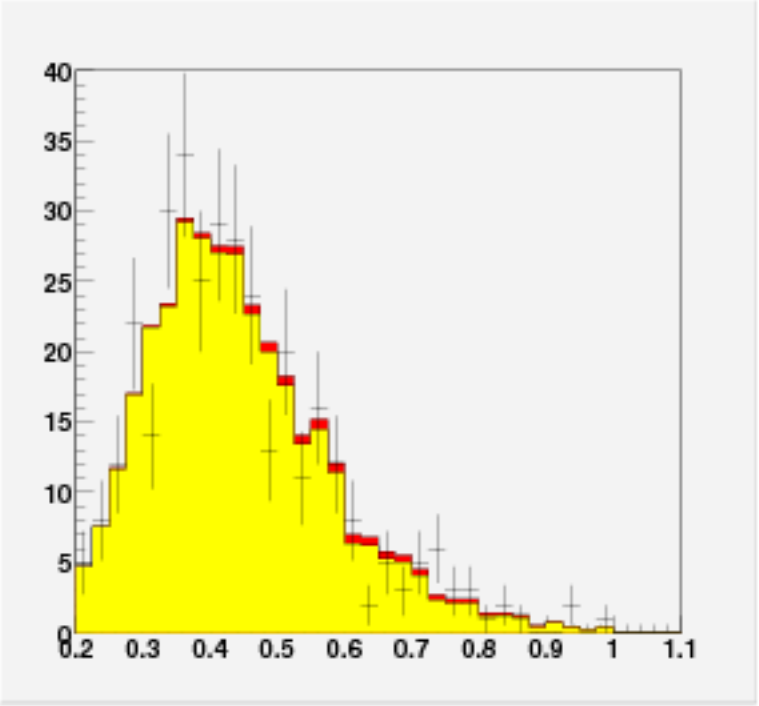

Figure 7.2: *A + 0.0035$\times \sum_3 E_T$ distribution. The yellow (red) histogram represents the background (signal) normalized to the outcome of the fit. The points represent the 347 candidates.*

7.3 Measurement of the $t\bar{t}$ production cross section

Having evaluated the amount of background, the value of $\sigma_{t\bar{t}}$ is:

$$\sigma_{t\bar{t}} = \frac{N_{cand} - n_b}{\epsilon_{kin} \cdot \epsilon_b \cdot \int \mathcal{L} dt} \tag{7.2}$$

where:

- $N_{cand} = 347$ events
- $n_b = 336^{+11}_{-16}$ events
- $\epsilon_{kin} = (16.4 \pm 3.2)$ %
- $\epsilon_b = (39.0 \pm 3.9)$ %

The kinematical and b-tagging efficiencies, included their uncertainty, have been reevaluated after the removal of the A + 0.0035$\times \sum_3 E_T$ cut.
The best value for $\sigma_{t\bar{t}}$ is the one which maximize the likelihood:

$$L = e^{-\frac{(\int \mathcal{L} dt - \overline{\int \mathcal{L} dt})^2}{2\sigma^2_{\mathcal{L}}}} \cdot e^{-\frac{(\epsilon_{kin} - \overline{\epsilon_{kin}})^2}{2\sigma^2_{\epsilon_{kin}}}} \cdot e^{-\frac{(\epsilon_b - \overline{\epsilon_b})^2}{2\sigma^2_{\epsilon_b}}} \cdot e^{-\frac{(n_b - \overline{n_b})^2}{2\sigma^2_{n_b}}} \times$$
$$\frac{(\epsilon_{kin} \cdot \epsilon_b \cdot \sigma_{t\bar{t}} \cdot \int \mathcal{L} dt + n_b)^{N_{cand}}}{N_{cand}} \cdot e^{-(\epsilon_{kin} \cdot \epsilon_b \cdot \sigma_{t\bar{t}} \cdot \int \mathcal{L} dt + n_b)}$$

that is:

$$\sigma_{t\bar{t}} = \mathbf{2.5^{+4.3}_{-2.5}(stat)^{+2.9}_{-2.5}(syst)\ pb}$$

.

This value is smaller but consistent with the theoretical calculations [1] $\sigma_{t\bar{t}} = 7$ pb.

Bibliography

[1] R. Bonciani *et al.*, *Nucl. Phys.*, B529, 424 (1998).

Conclusions

At the Fermilab Tevatron, top quarks are pair produced in $p\bar{p}$ collisions via $q\bar{q}$ annihilation and gg fusion, the former being the dominant process. In the framework of the Standard Model, each top quark decays almost exclusively into a W boson and a b quark. The Collider Detector at Fermilab (CDF) and D0 collaborations have reported the observation of the top quark in events collected during 1992-1995 data taking period (Run I).
In this analysis we search for events in which both W bosons decay into quark-antiquark pairs, leading to an all-hadronic final state.
The study of this channel, with a branching ratio of about $\frac{4}{9}$, complements the leptonic modes where one or both of the W bosons deday leptonically.
Since the expected decay signature involves only hadronic jets, a very large background from standard quantum chromodynamics (QCD) multijet production is present and dominates over $t\bar{t}$ production.
To reduce the background and increase the signal/background ratio to a good value ($\sim$ 1/15) we have performed a selection based on the kinematical characteristics of the events and we have required at least one b-jet.
Unfortunately both the statistical and systematical uncertainties on the expected background are large, making it difficult to extract a signal and a cross section measurement. For this reason we have introduced an alternative way of estimating the background leading to a preliminary measurement of $\sigma_{t\bar{t}}$:

$$\sigma_{t\bar{t}} = \mathbf{2.5^{+4.3}_{-2.5}(stat)^{+2.9}_{-2.5}(syst)\ pb}$$

Anyway, a group of people (P. Azzi, A. Castro, A. Gresele and T. Dorigo) is working very hard to improve this cross section value and, in particular, to implement the new jet corrections algorithms to obtain, for the next summer conferences, a top mass measurement.

Acknowledgements

The first person I would like to thank is Andrea Castro, for all the teaching he has given me during these years and for his patience...
I would also thank all members of the CDF Padova group and, in particular, Patrizia Azzi and Tommaso Dorigo, who helped me with important advice.
Special mention to Gabriele who has supported me with love: this thesis is dedicated to him.